STRONG INTERACTIONS BETWEEN TWO CO-ROTATING VORTICES IN ROTATING AND STRATIFIED FLOWS.

Ross R. Bambrey

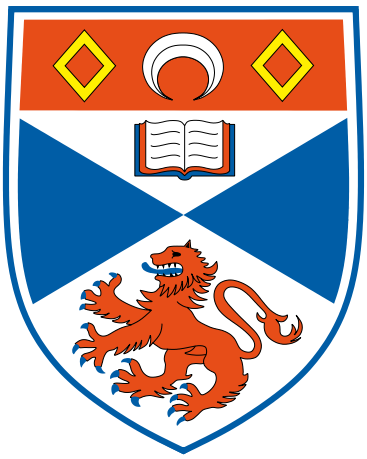

A thesis submitted for the degree of Doctor of Philosophy at the

University of St Andrews

23rd February 2007

Abstract

In this study we investigate the interactions between two co-rotating vortices. These vortices are subject to rapid rotation and stable stratification such as are found in planetary atmospheres and oceans. By conducting a large number of simulations of vortex interactions, we intend to provide an overview of the interactions that could occur in geophysical turbulence.

We consider a wide parameter space covering the vortices height-to-width aspect-ratios, their volume ratios and the vertical offset between them. The vortices are initially separated in the horizontal so that they reside at an estimated margin of stability. The vortices are then allowed to evolve for a period of approximately 20 vortex revolutions.

We find that the most commonly observed interaction under the quasi-geostrophic (QG) regime is partial-merger, where only part of the smaller vortex is incorporated into the larger, stronger vortex. On the other hand, a large number of filamentary and small scale structures are generated during the interaction. We find that, despite the proliferation of small-scale structures, the self-induced vortex energy exhibits a mean 'inverse-cascade' to larger scale structures. Interestingly we observe a range of intermediate-scale structures that are preferentially sheared out during the interactions, leaving two vortex populations, one of large-scale vortices and one of small-scale vortices.

We take a subset of the parameter space used for the QG study and perform

simulations using a non-hydrostatic model. This system, free of the layer-wise two-dimensional constraints and geostrophic balance of the QG model, allows for the generation of inertia-gravity waves and ageostrophic advection. The study of the interactions between two co-rotating, non-hydrostatic vortices is performed over four different Rossby numbers, two positive and two negative, allowing for the comparison of cyclonic and anti-cyclonic interactions. It is found that a greater amount of wave-like activity is generated during the interactions in anti-cyclonic situations. We also see distinct qualitative differences between the interactions for cyclonic and anti-cyclonic regimes.

Acknowledgements

I would like to thank my supervisor and friend Dr. Jean Reinaud for all his guidance and support throughout this project. Thanks are also due to Prof. David Dritschel and all other members of of the Vortex Dynamics group at the University of St Andrews School of Mathematics and Statistics.

Special thanks go to my wife Nina for her patience and understanding and to my parents Pauline and Richard Bambrey for their encouragement.

I am grateful to the UK Natural Environment Research Council (grant ref: NER/S/A/2003/11903) who funded this project.

Declaration

I, Ross Richard Bambrey, declare that this thesis has been composed by myself, that it is a record of my own work, and that it has not been accepted in any previous application for any degree.

Name: Ross R. Bambrey **Signature:**..... **Date:** .....

I was admitted as a research student in October 2003 and as a candidate for the degree of PhD in October 2003; the higher study for which this is a record was carried out in the University of St Andrews between 2003 and 2007.

Name: Ross R. Bambrey **Signature:**..... **Date:** .....

I hereby certify that the candidate has fulfilled the conditions of the Resolution and Regulations appropriate for the degree of PhD in the University of St Andrews and that the candidate is qualified to submit this thesis in application for that degree.

Name: Jean N. Reinaud **Signature:**..... **Date:** .....

In submitting this thesis to the University of St Andrews I understand that I am giving permission for it to be made available for use in accordance with the regulations of the University Library for the time being in force, subject to any copyright vested in the work not being affected thereby. I also understand that the title and abstract will be published, and that a copy of the work may be made and supplied to any bona fide library or research worker.

Name: Ross R. Bambrey **Signature:**..... **Date:** .....

Contents

List of Figures

List of Tables

Symbols and abbreviations

Abbreviations

CASL	Contour-Advective Semi-Lagrangian
ELM	Ellipsoidal model
PV	Potential vorticity
QG	Quasi-geostrophic
NH	Non-hydrostatic
2D	Two-dimensional
3D	Three-dimensional
IGW	Inertia-gravity wave
EI	Elastic interaction
PSO	Partial straining-out
CSO	Complete straining-out
PM	Partial merger
CM	Complete merger
NQG	Nonlinear quasi-geostrophic
OPV	Optimal potential vorticity

Commonly used symbols

a_{imb}	Imbalanced part of scalar a
$\mathbf{A}_h$	Horizontal part of vector $\mathbf{A}$
b	Buoyancy acceleration
$\mathcal{B}$	Ellipsoid shape matrix
$\mathcal{D}$	Isopycnal displacement
E_s	Vortex self-energy
f	Coriolis parameter
Fr	Froude number
g	Gravity
h	Vertical half-height
H	Characteristic vertical length scale
J	Angular impulse
$\mathbf{k}$	Vertical unit vector
L	Characteristic horizontal length scale
N	Buoyancy frequency
q	Potential vorticity anomaly
r	Horizontal mean radius
Ro	Rossby number
$\mathcal{S}$	Flow matrix
t	Time
$\mathbf{u} \equiv (u, v, w)$	3D velocity vector
U	Characteristic horizontal velocity scale
V	Volume
$\mathbf{X}$	Centroid position vector

δ	Horizontal gap between innermost edge of two ellipsoids
δz	Vertical offset as fraction of sum of half-heights
Δz	Vertical distance between two centroids
Γ	Circulation
κ	Strength
ρ	Density
ρ_V	Volume ratio
ψ	Scalar streamfunction in QG
$\boldsymbol{\varphi} = (\varphi, \psi, \phi)$	Vector streamfunction in NH
Π	Rossby-Ertel potential vorticity
$\boldsymbol{\omega} \equiv (\xi, \eta, \zeta)$	Vorticity vector
$\boldsymbol{\nabla}$	3D gradient operator
$\boldsymbol{\nabla}^2$	3D Laplacian operator
R_F	Elliptic integral of the first kind

Chapter 1

Introduction

1.1 Background

The fluid motions of planetary atmospheres and oceans are highly complex turbulent systems. This turbulence is partly a consequence of the interactions between coherently defined swirling masses of fluid, commonly termed as 'vortices'. Vortices are ubiquitous features of geophysical flows, see e.g. *Holton et al* (1995)[23], *Garret* (2000)[20] and *Marcus* (1988)[27]. In the oceans for example, *Ebbesmeyer et al* (1986)[18] estimated from observations that between 10^3 and 10^4 vortices populate the surface layers of the North Atlantic alone.

Very early attempts to explain vortices can be found in Aristotle's '*Meteorology*' (*circa* 350 B.C.E.)[2]. It is interesting to note that whilst he had already deduced, rather eccentrically by modern standards, the existence of buoyancy, the insistence on a fixed, non-rotating earth left him to reason that all winds travel in straight lines wherever possible and that eddy motions were caused by the inevitable meeting of a wind with another wind or a rigid boundary and being forced to take the path of least resistance and curving away.

Thanks to the observations of first Copernicus and later Kepler and Galileo,

we now know the Earth to be rotating. This rotation, along with the stable density stratification, greatly affects geophysical turbulence in that it reduces vortex stretching and renders the flow quasi-two-dimensional. Under rotation and stratification it becomes useful to regard vortices as coherent masses of potential vorticity, a conserved material tracer in the absence of diabatic and viscous effects which are often weak on the characteristic time and space scales of geophysical flows.

Vortex interactions, such as the merging storms in Jupiter's atmosphere shown in figure 1.1 are highly nonlinear and thus challenging to understand. Numerical and analytical studies of vortex interactions have as a result been primarily conducted in two-dimensional flows. Such flows are relevant to motions having characteristic horizontal scales L in excess of the bulk Rossby deformation length $L_D = NH/f$, where N is the buoyancy (or Brunt-Väisälä) frequency, H is the characteristic fluid depth and f is the Coriolis frequency, see *Dritschel et al.* (1999)[15]. Much of this research has sought to explain physically the average inverse-cascade of energy seen spectrally in two-dimensional turbulence as the growth of vortices through merger.

Initially, interactions between two identical vortices were considered. From this, *Waugh* (1992)[47] identified three different types of interaction which he classified: merger, pulsation with exchange and pulsation, adopting the terminology used by *Melander et al.* (1988)[28]. These interaction regimes are comparable with the regimes defined by *Reinaud & Dritschel* (2002)[36] for vortex interactions in the three-dimensional context. Here one can see that merger corresponds with complete-merger, pulsation with exchange to either partial-merger or weak-exchange depending on the volume of potential vorticity exchanged, and pulsation with elastic-interaction. Waugh also found that the generation of thin 'filaments' of vorticity was a common occurrence in vortex interactions.

Dritschel & Waugh (1992)[17] generalised the work of *Waugh* (1992)[47] by

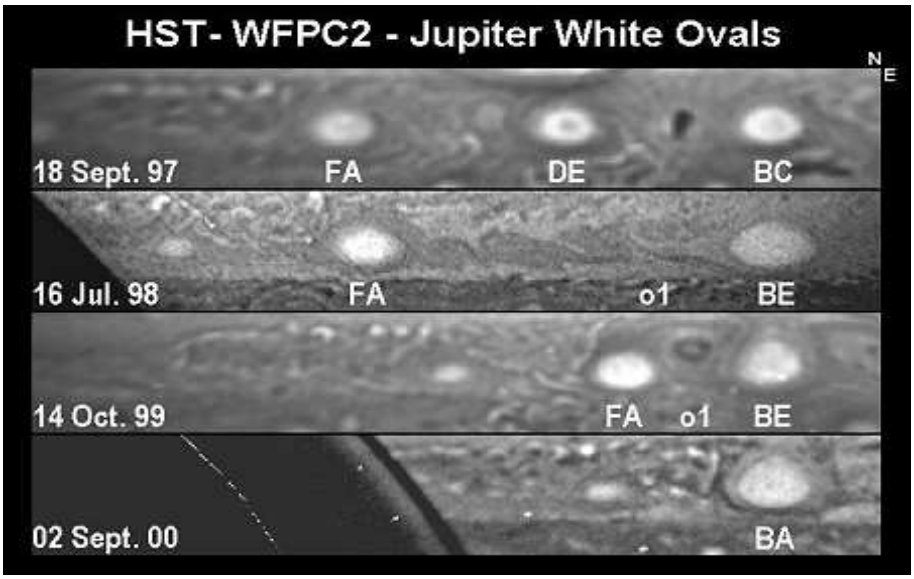

Figure 1.1: The merger of three vortical storms (FA, DE & BC) into one (BA) between September 1997 and September 2000. Images taken by Hubble telescope. Image credit NASA/JPL/WFPC2.

considering the interactions between vortices of different sizes. They found, in this case, four different types of interaction and most importantly that the classic picture of vortex merger, i.e. complete-merger, was a relatively uncommon occurrence. Furthermore, such interactions were often found to produce a number of *smaller* vortices making association with spectral cascade theories questionable. *Dritschel* (1995)[6] investigated the interactions of steadily co-rotating vortices. He demonstrated that strong interactions arise from a linear instability of the basic vortex configuration. Once again, complete-merger was found to be a rare phenomenon and smaller vortices were often produced.

In a more realistic three-dimensional approach, the simplest method of simulating vortex interactions whilst still maintaining the necessary geophysical conditions of stable stratification and rapid rotation is through the use of the quasi-geostrophic model. This model conveniently reduces the full equations of motion to a single dynamical equation for the conservation of the potential-vorticity

anomaly and a simple linear inversion relation for the recovery of the velocity field. It should be noted here that the potential-vorticity anomaly (hereinafter referred to as PV) in the quasi-geostrophic (QG) model represents the departure of the full PV field from the background potential-vorticity associated with the planetary rotation in the stratified fluid, see *Hoskins et al.* (1985)[24]. The QG model is based on the hydrostatic and geostrophic approximations which neglect acceleration in the momentum equations in the rotating frame of reference. These approximations are valid providing that the background rotation and stratification are suitably strong, i.e. the Rossby and Froude numbers are sufficiently small, see *Gill* (1982)[21] or *Vallis* (2006)[44]. The fluid motion in QG flows is constrained to move parallel to isopycnals. In this way it is layer-wise two-dimensional although the PV distribution is fully three-dimensional.

The inverse energy cascade also occurs in QG turbulence making it closely analogous to two-dimensional turbulence, and it also appears to have the same spectral form. *Charney* (1971)[5] predicted an inverse energy cascade for QG turbulence, this was shown by *Hua & Haidvogel* (1986)[26] who demonstrated that PV forms isolated structures in both forced and freely evolving QG turbulence. QG turbulence is also seen to follow the same mathematical regularity as two-dimensional turbulence, see *Tran & Dritschel* (2006)[43].

Recent studies of QG vortex interactions include works by *von Hardenberg et al.* (2000)[22], *Dritschel* (2002)[7], *Reinaud & Dritschel* (2002)[36], *Reinaud et al.* (2003)[39] and *Reinaud & Dritschel* (2005)[37]. The research of *von Hardenberg et al.* (2000)[22] and *Dritschel*[7] (2002) focused on the effects of the vortex shape, that is the height-to-width aspect ratio, on the critical merger distance between horizontally-aligned, equal-volume, equal-PV vortices. It was found by *Dritschel* (2002)[7] that the merger of tall vortices does not tend to two-dimensional merger. Instead, the vortices break up into three-dimensional structures due to a basic instability affecting tall vortices (after scaling the vertical co-ordinate by the

conventional f/N), see *Dritschel & de la Torre Juárez* (1996)[14], *Dritschel et al.* (1999)[15] and *Billant et al.* (2006)[3].

Reinaud & Dritschel (2002)[36] investigated the effect of a vertical offset on the merger distance between two equal-PV, equal-volume and unit height-to-width aspect-ratio (again after f/N vertical scaling) vortices. They discovered that vertically offset vortices can merge from greater horizontal separations due to the effects of vertical shear. On the other hand the simulations of freely decaying QG turbulence analysed in *Reinaud et al.* (2003)[39] show that the most robust, long-lived vortices have a mean height-to-width aspect-ratio of 0.8, vertical shear being the reason for the oblate shape of the vortex.

A linear stability analysis was performed by *Reinaud & Dritschel* (2005)[37] to determine the critical merger distance between two equal-PV ellipsoidal vortices, as a function of the volume ratio of the ellipsoids, their vertical offset and their height-to-width aspect ratios. To allow them to cover such a vast parameter space the authors used a reduced model, the 'ellipsoidal model' (ELM), as described in full in *Dritschel et al.* (2004)[13]. This model represents vortices as ellipsoids of uniform PV and filters out any non-ellipsoidal deformations. The ELM however, accurately approximates the critical merger distance, based on comparisons with the QG model, see *Reinaud & Dritschel* (2005)[37] for details.

The extensive use of the QG model in previous studies is attributable to its accuracy in simulating the large scale 'balanced' motions, i.e. vortices, seen in the atmosphere and oceans. The atmosphere and oceans however are more frequently observed to be more in a state of 'near-balance' meaning that oscillations of the density stratification surfaces exist but have very little impact on the large scale vortical motions, see for example *Mohebalhojeh & Dritschel* (2000)[32] and *Dritschel & Viúdez* (2007)[12].

These density surface oscillations are generally termed inertia-gravity waves

(IGW) and for distinction from the part of the flow associated with vortical motions, are often referred to as the '*imbalanced*' part of the flow. An example of an IGW in the atmosphere is shown in figure 1.2 where cloud rolls indicate the crests in the IGW.

Dritschel & Viúdez (2003)[16] developed a method to model three-dimensional, rotating, stratified flows at finite Rossby numbers. The authors used the ageostrophic horizontal vorticity components, representing the departure from hydrostatic and geostrophic balance, along with PV as new variables for the flow.

Several methods exist for decomposing the full flow into its balanced and imbalanced components. Optimal potential vorticity balance (OPV), *Viúdez & Dritschel* (2004)[45], uses backwards and forwards time-integrations to remove most of the IGW's. Another example is the nonlinear-QG (NQG) method developed in *McKiver & Dritschel* (2006)[31] which uses QG scaling of the non-hydrostatic equations from *Dritschel & Viúdez* (2003)[16]. Computationally the NQG method is less expensive than OPV but is seen to be less accurate in that it attributes more of the flow to imbalance than OPV does.

The non-hydrostatic model also allows for the consideration of cyclonic and anti-cyclonic regimes by considering positive and negative Rossby numbers respectively. *Arai & Yamagata* (1994)[1] find a distinct asymmetry between the evolution of cyclonic and anti-cyclonic vortices in shallow-water. In their studies the cyclonic vortices were seen to split in two when the surface displacement exceeded a critical value. *Polvani et al.* (1994)[35] witness a predominance of anti-cyclonic vortices over cyclonic vortices emerging from decaying shallow-water turbulence. It should be noted however that the shallow water cases are significantly different to the three-dimensional cases, see *Stegner & Dritschel* (2000)[41]. Interestingly *Theiss* (2004)[42] finds a predominance of cyclonic vortices in geostrophic turbulence using the QG shallow-water equations on a β-plane. This, the author states, is concurrent with observations of the predominance of cyclonic

Figure 1.2: Altocumulus Undulatus. Cloud rolls indicating the crests of a gravity wave on the cloud deck. Image ©Harald Edens, reproduced with permission[25].

vortices in the oceans, citing *Munk et al.* (2000)[33] and *Rudnick* (2001)[40].

1.2 Motivation

As has been discussed above, vortex interactions have been widely studied in both two and three-dimensions. The classical concept of vortex merger as shown in figure 1.3, that is the complete merger of two vortices into one vortex is consistent with the theory of the spectral 'inverse-cascade' of energy in QG flows. However figure 1.3 shows only a fraction of the full story. Consider, for example, the case shown in figure 1.4. This has two vortices of equal volume, with the gap between the outer edges of the vortices being the same as for figure 1.3, The height-to-width aspect-ratios of the vortices are 4 for the prolate vortex and 0.5 for the oblate vortex, their vertical offset (the distance between their centroids) is 80% of the sum of their vertical half-heights. Here we witness an entirely different

behaviour, that is after merger has taken place a large filament is ejected from the main vortex which then proceeds to roll-up into several smaller vortices at later times. This would indicate that while much of the self-energy of the initial vortices is contained within one larger structure – physically consistent with the inverse-cascade – some of the self-energy is now contained at smaller scales which contributes to the direct energy cascade..

Figure 1.4 is merely an example of the complex behaviour displayed during vortex interactions. It does however indicate that vortex interactions are not trivial problems as their nature can be highly complex.

It has been seen that asymmetry between cyclonic evolutions and anti-cyclonic evolutions exists. By utilising a non-hydrostatic model it is possible to investigate the differences between cyclonic and anti-cyclonic interactions between discrete pairs of co-rotating vortices. Using this model we may also investigate the generation of IGW's during the interactions and how this may differ by changing the Rossby number.

1.3 Outline

This work will be organised as follows. In chapter 2 we will introduce the governing equations for the models we will use namely the quasi-geostrophic model and the non-hydrostatic model. Also in this chapter we will provide a short discussion on the numerical methods employed in simulating these models.

Chapter 3 will focus entirely on the results of simulating two co-rotating quasi-geostrophic vortices at an estimated margin of stability and will investigate the resulting interactions between them.

In chapter 4 we will expand our investigation to employ the non-hydrostatic model for investigating a subset of those cases in Chapter 3. We draw conclusions

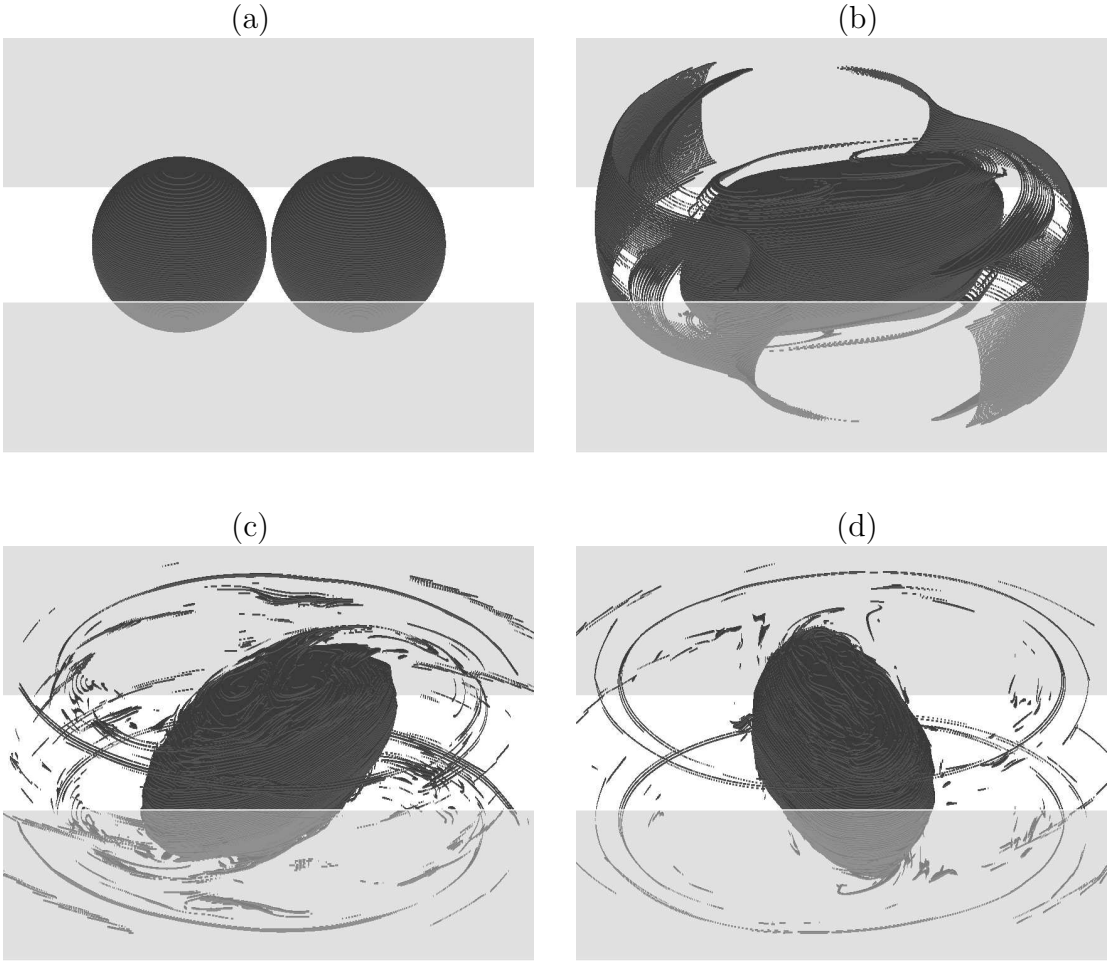

Figure 1.3: The interaction of two vertically aligned, spherical vortices. PV anomaly $q = 2\pi$, times shown at $t = 0$, $t = 14$, $t = 40$ and $t = 60$. Viewing angle is 60° from the vertical and horizontal scale is ± 1.5 centred around the origin of the domain. Light grey areas show front and back walls of the box which spans the full height of the PV distribution.

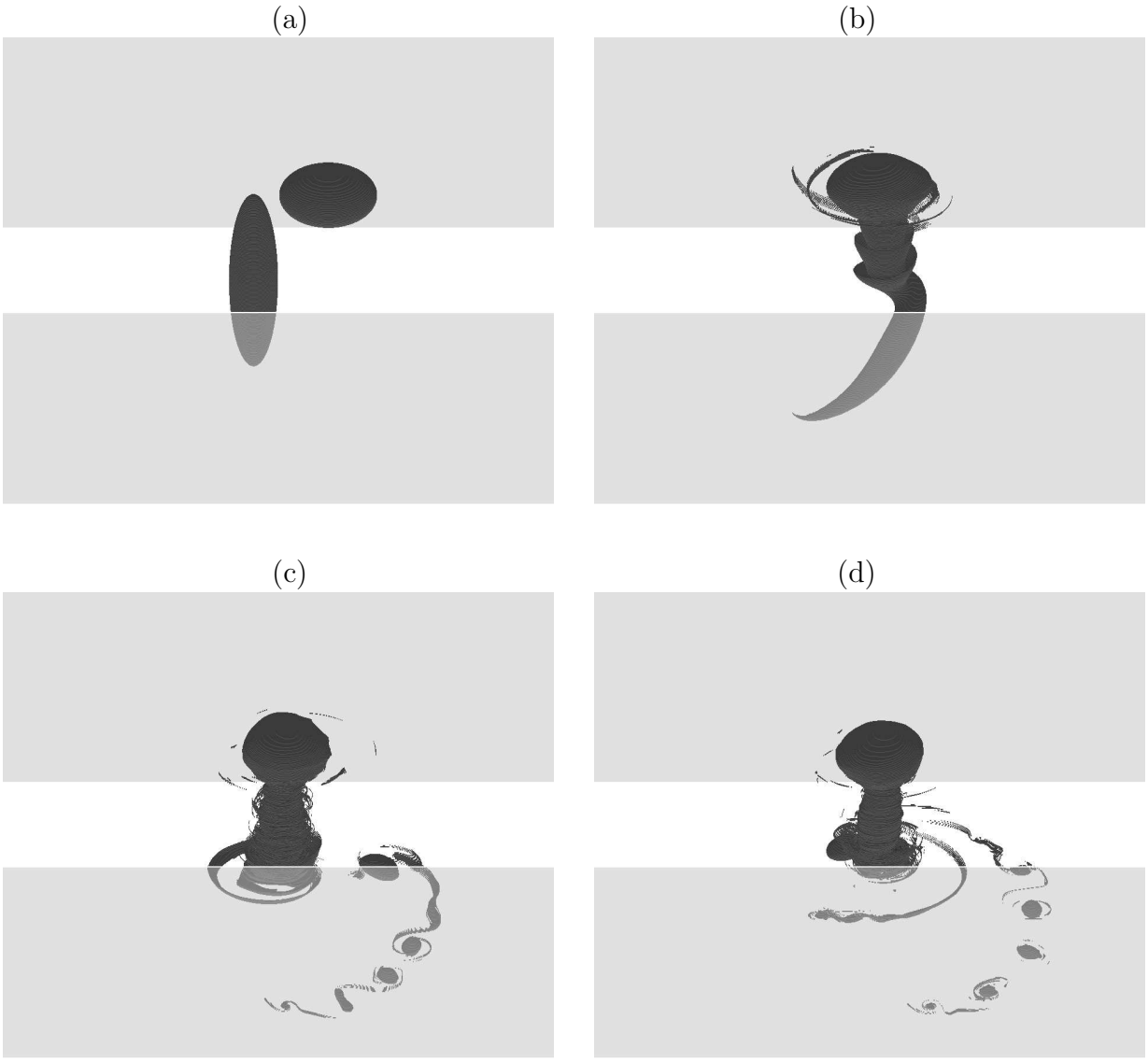

Figure 1.4: The interaction of one prolate vortex (height-to-width aspect-ratio of 4) and one oblate vortex (height-to-width aspect-ratio of 0.5) of equal volume, offset vertically by 80% of the sum of the vortex half-heights. PV anomaly $q = 2\pi$, times shown at $t = 0$, $t = 14$, $t = 40$ and $t = 60$. Viewing angle is 60° from the vertical and horizontal scale is ± 2.0 centred around the origin of the domain. Light grey areas show front and back walls of the box which spans the full height of the PV distribution.

and investigate future developments in chapter 5.

Chapter 2

Mathematical formulation and computational methods

2.1 Introduction

In this chapter we introduce the mathematical models used in this study. Section 2.2 provides a brief description of the quasi-geostrophic (QG) equations and the assumptions under which they are valid. We present the "Contour-Advective Semi-Lagrangian" algorithm in section 2.3. This algorithm is used to solve the QG equations. We go on to present the non-hydrostatic equations in section 2.4 and the algorithm used to solve them in section 2.5.

2.2 The Quasi-geostrophic Equations

The inviscid quasi-geostrophic equations for a rotating, stratified fluid may be obtained by the asymptotic expansion of Euler's equations for $\epsilon = H/L \ll 1$ where H and L are respectively the characteristic height and length scales of the fluid, and for $Fr^2 \ll Ro \ll 1$ where the Froude number, Fr, and the Rossby

number, Ro, are defined as

$$Fr = \frac{U}{NH}, \quad Ro = \frac{U}{fL}, \tag{2.1}$$

where N is the Brunt-Väisälä buoyancy frequency being the frequency of oscillation a fluid parcel would have if it was displaced a small amount in the vertical. f is the Coriolis frequency. In QG, the horizontal component of the Earth's rotation is neglected, see e.g. *Gill* (1982)[21] or *White* (2002)[48]. Only the local vertical component of the rotation vector is taken to be important, given by the 'Coriolis parameter',

$$f = 2\Omega \sin \phi, \tag{2.2}$$

where ϕ is the latitude and Ω is the planetary rotation rate.

We introduce the potential vorticity (PV) $q = q(x, y, z, t)$ or more appropriately the PV anomaly which represents the departure from the background PV, i.e. $q \equiv Q - f$ where Q is the full quasi-geostrophic potential vorticity. In the absence of relatively weak dissipative and diabatic effects and for constant N and f, the governing equations become

$$\frac{\mathrm{D}q}{\mathrm{D}t} = \frac{\partial q}{\partial t} + u\frac{\partial q}{\partial x} + v\frac{\partial q}{\partial y} = 0, \tag{2.3a}$$

$$\frac{\partial^2 \psi}{\partial x^2} + \frac{\partial^2 \psi}{\partial y^2} + \frac{f^2}{N^2}\frac{\partial^2 \psi}{\partial z^2} = q, \tag{2.3b}$$

$$\mathbf{u} = (u, v, 0) = \left(-\frac{\partial \psi}{\partial y}, \frac{\partial \psi}{\partial x}, 0\right), \tag{2.3c}$$

where ψ is the stream function. These equations are obtained under lowest-order hydrostatic and geostrophic balance. Hence there is no vertical advection at this order. Moreover, inertia-gravity waves are filtered and the velocity field $\mathbf{u}$ is the geostrophic velocity.

Equation 2.3b can be further simplified by stretching the vertical coordinate by Prandtl's ratio N/f so that it becomes Poisson's equation

$$\boldsymbol{\nabla}^2\psi = q, \tag{2.4}$$

where $\boldsymbol{\nabla}^2$ is the three-dimensional Laplacian operator. Note that the motion is layer-wise two-dimensional although equation 2.4 is isotropic. A full discussion and derivation of the quasi-geostrophic equations can be found in e.g. *Gill* (1982)[21] and *Vallis* (2006)[44].

2.3 The Contour-Advective Semi-Lagrangian algorithm

The "Contour-Advective Semi-Lagrangian" algorithm (CASL) is a computational method originally presented in *Dritschel & Ambaum* (1997)[8], for solving the 2D equations. This method is a hybrid Lagrangian-Eulerian method in that it utilises contour-advection for the advection of potential vorticity but also employs a spectral method to solve the inversion relations in equation 2.4.

CASL is able to resolve a wide range of scales due to the way in which the PV anomaly may be represented down to one-tenth of the actual grid scale, but still benefits from the efficiency of spectral methods in computing the flow field. *Dritschel, Polvani & Mohebalhojez* (1999)[10] show CASL in comparison with other models in the context of the QG shallow water equations to be the most accurate and efficient.

A summary of CASL is as follows:

(a) Initialisation: The PV distribution is defined in terms of a set of contours in each horizontal layer. Each contour is assigned nodes, connected by a

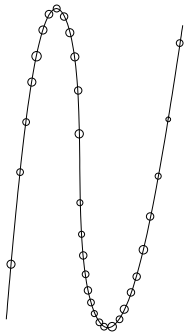

Figure 2.1: Example of node distribution along a PV contour.

cubic spline to define the contour's shape see for example figure 2.1.

(b) PV Contour-to-grid conversion: The PV contours defined in the first step are converted to a gridded field via a 'fast-fill' procedure described in full in *Dritschel & Ambaum* (1997)[8]. The PV is converted to a horizontal grid four times finer than the horizontal velocity grid and a vertical grid four times the number of vertical grid points as the number of layers. The PV is then averaged to a grid four times coarser, see figure 2.2.

(c) Inversion: CASL computes the streamfunction by inverting the Laplacian in equation 2.4 in spectral space via a Fast Fourier Transform (FFT). The streamfunction can then be used to obtain the velocity field. Note that for the purposes of this research, we adapted CASL to use the "Fastest Fourier Transforms in the West" (FFTW) version 2.1.5[19] a free, open-source FFT library.

(d) Contour Advection: The gridded velocity field is bi-linearly interpolated to get the velocity at each node. The nodes of the PV contours are advected using the velocity obtained from the interpolation. The algorithm then returns to step (b) at repeats until all 4 stages of the 4th order Runge-Kutta integration are completed.

(e) Contour Surgery: Every other time-step 'contour surgery' is performed

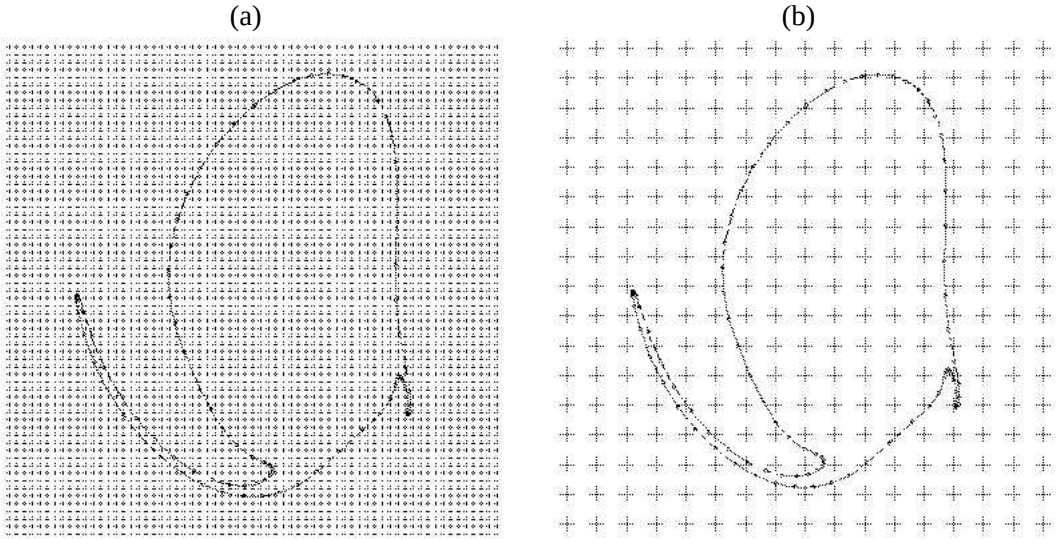

Figure 2.2: Example of PV contour on (a) the fine-scale grid for 'contour-to-grid' conversion and (b) the final velocity grid 4 times coarser than the fine-scale grid.

to remove filaments of PV that are smaller than a certain width. This can also result in the connection or disconnection of two vortices. At the end of this step the nodes are redistributed on the PV contours in such a way to provide the highest possible accuracy when the contours have high curvature.

2.4 The non-hydrostatic equations

We now present the non-hydrostatic equations for a rotating, stratified fluid. The removal of the balance restrictions in QG means that we now have access to inertia-gravity waves and the ageostrophic velocity field.

The part of the flow characterised by relatively large-scale, vortical motions is termed the 'balanced' part of the flow. The part of the flow characterised by relatively small-scale, inertia-gravity wave-like motions is known as the 'imbalanced' part of the flow.

Again the fluid is assumed to be inviscid and incompressible. The governing equations are recast in terms of new variables which explicitly distinguish between the balanced and imbalanced part of the flow. The PV anomaly is again materially conserved, that is

$$\frac{\partial q}{\partial t} + (\mathbf{u}.\boldsymbol{\nabla})q = 0 \tag{2.5}$$

where $\mathbf{u} = (u, v, w)$. Leading order imbalance is represented by the horizontal component of the vector $\mathcal{A}$, that is $\mathcal{A}_h$, where

$$\mathcal{A} = \frac{\boldsymbol{\omega}}{f} + \frac{\boldsymbol{\nabla} b}{f^2}, \tag{2.6}$$

where $b \equiv -g\rho'/\rho_0$ is the buoyancy, g is the gravity, ρ' is the anomalous density, ρ_0 is the background density and $\boldsymbol{\omega} = \boldsymbol{\nabla} \times \mathbf{u}$ is the vorticity. Note that $\mathcal{A}_h = 0$ approximately corresponds to thermal wind balance, consequently $\mathcal{A}_h$ may be thought of as the departure from this balance. The transport equation for $\mathcal{A}_h$ is

$$\frac{\mathrm{D}\mathcal{A}_h}{\mathrm{D}t} = -f\mathbf{k} \times \mathcal{A}_h + \left(1 - \frac{N^2}{f^2}\right) \boldsymbol{\nabla}_h w + \frac{1}{f}\boldsymbol{\omega} \cdot \boldsymbol{\nabla}\mathbf{u}_h + \frac{N^2}{f^2}\boldsymbol{\nabla}_h \mathbf{u} \cdot \boldsymbol{\nabla}\mathcal{D}, \tag{2.7}$$

where $\mathcal{D}$ is the isopycnal displacement defined by $\mathcal{D} \equiv -b/N^2$.

The primitive variables b and $\mathbf{u}$ are obtained by introducing a new vector potential $\boldsymbol{\varphi} = (\varphi, \psi, \phi)$ such that

$$\mathcal{A} = \boldsymbol{\nabla}^2 \boldsymbol{\varphi} \tag{2.8}$$

and

$$b = f^2 \boldsymbol{\nabla} \cdot \boldsymbol{\varphi} \tag{2.9a}$$

and

$$\mathbf{u}/f = -\boldsymbol{\nabla} \times \boldsymbol{\varphi}. \tag{2.9b}$$

The horizontal parts of $\boldsymbol{\varphi}$, that is $\boldsymbol{\varphi}_h$, can be found by directly inverting Laplace's operator

$$\boldsymbol{\varphi}_h = \boldsymbol{\nabla}^{-2}\mathcal{A}_h. \tag{2.10}$$

We wish to use the PV as the variable to represent balance, the Rossby-Ertel PV Π is given by

$$\Pi \equiv \frac{\boldsymbol{\omega}_a}{f} \cdot \boldsymbol{\nabla}\mathbf{Z} \tag{2.11}$$

in dimensionless form. Here $\boldsymbol{\omega}_a$ is the absolute vorticity, that is the vorticity plus the background vorticity $f\mathbf{k}$, and $\mathbf{Z} = z - \mathcal{D}$ is the reference height of an isopycnal. Thus Π can be expressed as

$$\Pi = (\mathbf{k} + \omega/f) \cdot (\mathbf{k} - \boldsymbol{\nabla}\mathcal{D}) = 1 + \frac{\zeta}{f} - \frac{\partial \mathcal{D}}{\partial z} - \frac{\boldsymbol{\omega}}{f} \cdot \boldsymbol{\nabla}\mathcal{D}. \tag{2.12}$$

where ζ is the vertical component of the vorticity. Now substituting for $\boldsymbol{\omega}$ we obtain an expression for the PV anomaly $q = \Pi - 1$ in terms of the vector potential

$$q = \mathcal{L}_{QG}\phi - (1 - \frac{f^2}{N^2})\frac{\partial \Theta}{\partial z} - \frac{f^2}{N^2}\mathcal{N}(\boldsymbol{\varphi}), \tag{2.13}$$

where $\mathcal{L}_{QG}$ is the quasi-geostrophic Laplacian operator

$$\mathcal{L}_{QG}\phi \equiv \frac{\partial^2 \phi}{\partial x^2} + \frac{\partial^2 \phi}{\partial y^2} + \frac{f^2}{N^2}\frac{\partial^2 \phi}{\partial z^2}, \tag{2.14a}$$

also

$$\Theta \equiv \boldsymbol{\nabla}_h \cdot \boldsymbol{\varphi}_h \tag{2.14b}$$

and

$$\mathcal{N}(\boldsymbol{\varphi}) \equiv \boldsymbol{\nabla}(\boldsymbol{\nabla}\cdot\boldsymbol{\varphi})\cdot[\boldsymbol{\nabla}^2\boldsymbol{\varphi} - \boldsymbol{\nabla}(\boldsymbol{\nabla}\cdot\boldsymbol{\varphi})]. \tag{2.14c}$$

Thus ϕ must be found from the definition of q in equation 2.13. The result is a double Monge-Ampère equation. A full discussion on the derivation and solution of these equations can be found in *Dritschel & Viúdez* (2003)[16].

2.5 Computational method for solving the non-hydrostatic equations.

A full and detailed description of the algorithm used to solve the non-hydrostatic equations discussed in the previous section can be found in the appendix of *Dritschel & Viúdez* (2003)[16]. We provide here an overview of the algorithm.

(a) Initialisation: The PV contours are defined but the PV anomaly they contained is taken to be initially zero. The PV anomaly inside these contours is then increased slowly compared with the buoyancy and inertial periods. The PV contours remain fixed whilst the PV is increased. This technique has been found to generate virtually no spurious inertia-gravity waves.

(b) PV interpolation: First the same 'fast-fill' routine is used as in QG that is interpolating PV contour nodes onto a fine-scale grid (here again four times finer than the velocity grid in each direction). Then two further interpolations are needed first to find the relative height of the isopycnal surface from the gridded displacement field, and second to find the PV at the grid points lying between these surfaces. These two interpolations are taken to be linear.

(c) Inversion: The horizontal part of the vector potential $\boldsymbol{\varphi}_h$ is found by inverting the Laplacian operator in spectral space using fast Fourier trans-

forms. The vertical part of the potential can be expressed as a double Monge-Ampère which can be solved using an iterative method described in *Dritschel & Viúdez* (2003)[16]. Having found $\boldsymbol{\varphi}$ the primitive variables can be recovered.

(d) Time integration: The recovered velocity field is used to explicitly advect the nodes representing the PV contours, this is done using a third-order, three time-level Adams-Bashforth integration procedure (see *Dritschel , Polvani & Mohebalhojeh* (1999)[10]). The imbalanced fields are evolved using an explicit leap-frog scheme with a weak time filter to avoid decoupling of even and odd time levels, see again *Dritschel, Polvani & Mohebalhojeh* (1999)[10] for details.

(e) Contour Surgery: This is identical to the method used for QG. At certain time intervals, filaments of PV less than a prescribed width, here one-twentieth of the horizontal grid scale, are removed and the nodes defining the contours are re-distributed.

Chapter 3

Interactions between two co-rotating quasi-geostrophic vortices

3.1 Introduction

In this chapter we investigate the interactions between two initially ellipsoidal QG vortices. These vortices are set up so that they reside at an estimated margin of stability which is determined using a method based on the "Ellipsoidal Model" (ELM) developed in *Dritschel, Reinaud & McKiver* (2004)[13]. First we give a brief description of the model and the method used to obtain the margin of stability. Then we describe the parameter space chosen for this investigation and present the results from the QG simulation. We finish with conclusions. These results are currently submitted to the Journal of Fluid Mechanics.

3.1.1 The quasi-geostrophic ellipsoidal model

ELM is a simplified system that models vortices as uniform ellipsoids of PV. These vortices remain ellipsoidal for all time and any non-ellipsoidal deformation is filtered out. ELM represents each ellipsoid i by a symmetric matrix $\mathcal{B}_i$ where

$$\mathcal{B}_i = \begin{pmatrix} (B_i)_1 & (B_i)_2 & (B_i)_3 \\ (B_i)_2 & (B_i)_4 & (B_i)_5 \\ (B_i)_3 & (B_i)_5 & (B_i)_6 \end{pmatrix} \tag{3.1}$$

and a centroid position $\mathbf{X}_i$. The surface of each ellipsoid is represented by the set of points $\mathbf{x}$ such that

$$(\mathbf{x} - \mathbf{X}_i)^T \mathcal{B}_i^{-1} (\mathbf{x} - \mathbf{X}_i) = 1, \tag{3.2}$$

where the superscript ^{T} represents the transpose. The governing equations of ELM for the i^{th} ellipsoid are

$$\frac{\mathrm{d}\mathbf{X}_i}{\mathrm{d}t} = -\frac{1}{\kappa_i} \mathcal{L} \frac{\partial H}{\partial \mathbf{X}_i}, \tag{3.3a}$$

$$\frac{\mathrm{d}\mathcal{B}_i}{\mathrm{d}t} = \mathcal{S}_i \mathcal{B}_i + \mathcal{B}_i \mathcal{S}_i^T, \tag{3.3b}$$

$$\mathcal{S}_i = -\frac{10}{\kappa_i} \mathcal{L} \frac{\partial H}{\partial \mathcal{B}_i}, \tag{3.3c}$$

where $\kappa_i = q_i V_i / 4\pi$ is the 'strength' of the vortex i, q_i is the PV of vortex i and V_i is its volume and

$$\mathcal{L} = \begin{pmatrix} 0 & -1 & 0 \\ 1 & 0 & 0 \\ 0 & 0 & 0 \end{pmatrix}. \tag{3.4}$$

H is the Hamiltonian of the system, i.e. the total energy divided by 4π and $\mathcal{S}_i$ is known as the flow-matrix (see *McKiver & Dritschel* (2003)[30]). This Hamiltonian formulation ensures that the vortices remain ellipsoidal.

H can be decomposed into $H = H^v + H^b$ where H^v corresponds to the self-energy of the vortex and H^b corresponds to the interaction energy. H^v is known analytically,

$$H^v = \frac{3}{5}\kappa R_F(a^2, b^2, c^2), \tag{3.5}$$

where a, b and c are the ellipsoid axis lengths and R_F is an elliptic integral of the first kind such that

$$R_F(a^2, b^2, c^2) = \frac{1}{2}\int_0^\infty \frac{\mathrm{d}t}{\sqrt{(t+a^2)(t+b^2)(t+c^2)}}, \tag{3.6}$$

see *Chandrasekhar* (1969)[4]. a^2, b^2 and c^2 are the eigenvalues of the $\mathcal{B}$-matrix and $\hat{\mathbf{a}}$, $\hat{\mathbf{b}}$ and $\hat{\mathbf{c}}$ are the eigenvectors of the $\mathcal{B}$-matrix. The eigenvectors give the direction of the corresponding axis of the ellipsoid, see figure 3.1.

H^b is calculated by modelling each ellipsoid as a finite sum of singular point vortices. The position and strength of the singularities are obtained such that the approximate streamfunction induced by them matches exactly with the streamfunction at a given order of accuracy in $1/d$, d being the distance from $\mathbf{X}_i$ to the point of evaluation. Table 3.1 shows the order of accuracy depending on the number of singularities the ellipsoid is represented by.

The flow matrices can then be expressed analytically. Full details of ELM and its derivation can be found in *Dritschel, Reinaud & McKiver* (2004)[13].

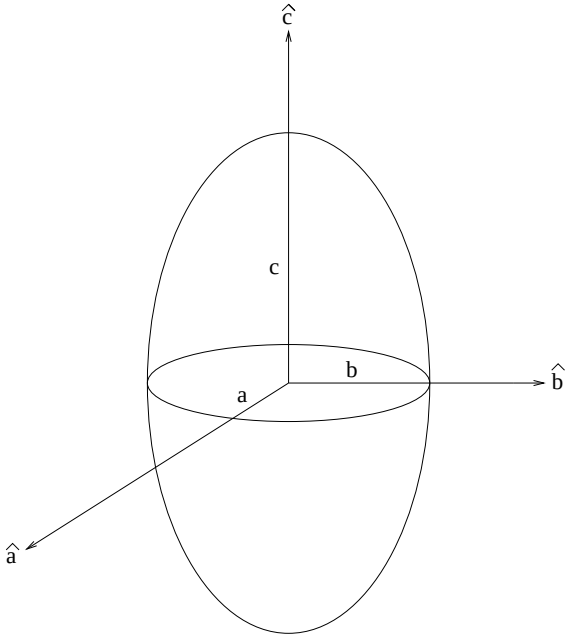

Figure 3.1: Definition of ellipsoid axis length and axis direction parameters. Figure courtesy of *McKiver & Dritschel* (2003)[30].

Number of singularities	Order of accuracy
1	$\mathcal{O}(1/d^3)$
4	$\mathcal{O}(1/d^5)$
7	$\mathcal{O}(1/d^7)$
13	$\mathcal{O}(1/d^9)$

Table 3.1: Order of accuracy in $1/d$ depending on the number of singularities representing the ellipsoid.

3.1.2 Initial conditions

Reinaud & Dritschel (2005)[37] use the ELM to determine families of equilibria for pairs of ellipsoids that have prescribed volume-ratios, ($\rho_V = V_2/V_1$), vertical offsets (Δz), and height-to-width aspect-ratios (h/r) – where h is the vertical half height of the ellipsoid and r is its mean horizontal radius. Note that in QG the vertical offset between two vortices is a special parameter due to the lack of vertical advection, see for example *Reinaud & Dritschel* (2002)[36]. δ is defined as the horizontal gap between the two innermost edges of the ellipsoids, given as

$$\delta = |\mathbf{X}_1 - \mathbf{X}_2| - \sqrt{(B_1)_1} - \sqrt{(B_2)_1}. \tag{3.7}$$

Below a critical value of δ the equilibria become unstable making strong interactions such as vortex merger possible in the full QG equations. The length scale of the problem is set by the total volume of PV, $4\pi/3$.

Starting from two well separated spheroids with fixed δ we use an iterative method to reach the equilibrium state. Note that in referring to an equilibrium state here we do not refer to the vortices being stationary, but they rotate steadily without developing any deformations. Iteration continues until the *r.m.s.* correction to the two $\mathcal{B}$-matrices is less than 10^{-12}. The horizontal gap is then reduced by 2×10^{-4} and the $\mathcal{B}$-matrices of the last state are used for the first guess for the next state. This procedure is continued until the total energy of the equilibrium is seen to decrease since in general at the margin of stability the total energy exhibits a maximum. A linear-stability analysis is then performed on four states surrounding the maximum of energy to verify that this maximum does indeed coincide with the margin of stability. The linear stability analysis is performed by superimposing the perturbation $(\tilde{\Delta}, \tilde{\mathcal{B}})$ on $\bar{\Delta}$ and $\bar{\mathcal{B}}_{i=1,2}$ where $\bar{\Delta} = \mathbf{X}_1 - \mathbf{X}_2$ describes the position of the vortices relative to each other and $\bar{\mathcal{B}}_{i=1,2}$ are their $\mathcal{B}$-matrices at equilibrium. The perturbation is chosen to have an exponential

time dependence

$$\mathcal{B} = \bar{\mathcal{B}} + \tilde{\mathcal{B}} = \bar{\mathcal{B}} + \hat{\mathcal{B}}e^{\sigma t}, \tag{3.8a}$$

$$\mathbf{\Delta} = \bar{\Delta} + \tilde{\Delta} = \bar{\Delta} + \hat{\Delta}e^{\sigma t}, \tag{3.8b}$$

where $\sigma = \sigma_r + i\sigma_i$ is a complex number with σ_r representing the growth rate and σ_i representing the frequency of the mode. Note that $\hat{\Delta} = (\hat{\Delta x}, \hat{\Delta y}, 0)$ and

$$\hat{\mathcal{B}} = \begin{pmatrix} \hat{B}_1 & \hat{B}_2 & \hat{B}_3 \\ \hat{B}_2 & \hat{B}_4 & \hat{B}_5 \\ \hat{B}_3 & \hat{B}_5 & 0 \end{pmatrix}. \tag{3.9}$$

$\hat{\Delta z}$ and $\hat{B}_6$ are zero in QG flows due to the absence of vertical advection.

Reinaud & Dritschel (2005)[37] showed that the horizontal gap corresponding to the state with maximum energy δ_m is the margin of stability.

For some cases where the ellipsoids were nearly horizontally aligned, *Reinaud & Dritschel* (2005) were unable to determine the steady states due to the presence of a spurious oscillatory mode, see in particular their figure 6. To determine these states we modify the approach used by the authors. We start with the steady state at the margin of stability for a vortex pair with the same height-to-width aspect-ratio and volume-ratio but offset in the vertical by $\Delta z = 0.2(h_1 + h_2)$. The same procedure is then adopted, decreasing the vertical offset instead of the horizontal gap. When near horizontal alignment is achieved, we then revert to the original method and search along the horizontal for the critical gap.

We illustrate the case of $h_1/r_1 = 1.0$, $h_2/r_2 = 0.8$, $\rho_V = 1.0$ and $\Delta z = 0.005(h_1 + h_2)$. Figures 3.2 and 3.3 respectively show the energy (E) and the angular impulse (J) versus the horizontal gap δ. We see a maximum energy and a minimum angular impulse at $\delta_m = 2.2318$.

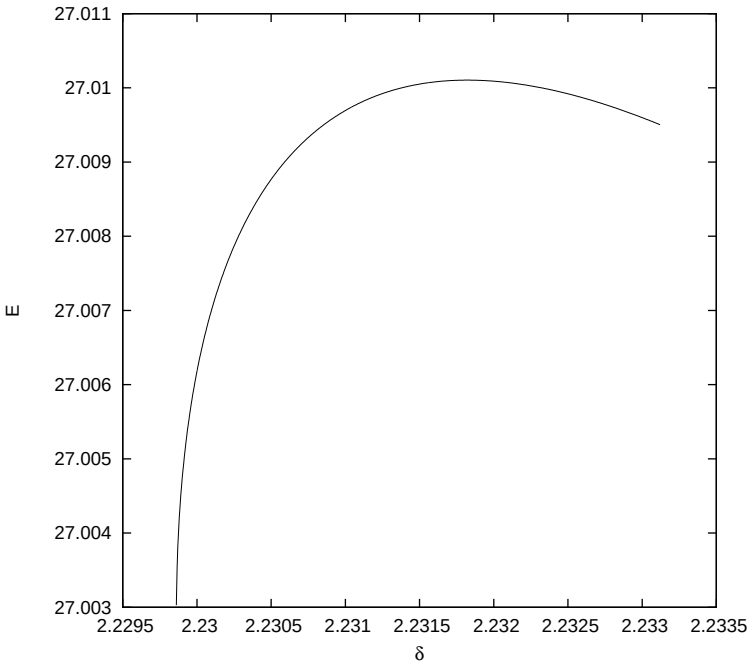

Figure 3.2: Energy (E) vs horizontal gap δ for the case $h_1/r_1 = 1.0$, $h_2/r_2 = 0.8$, $\rho_V = 1.0$ and $\Delta z = 0.005(h_1 + h_2)$.

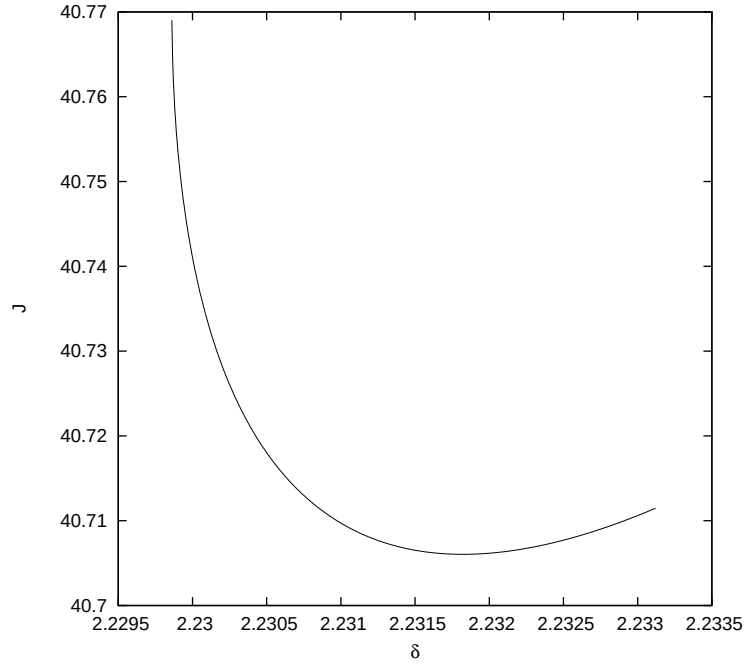

Figure 3.3: Angular impulse (J) vs horizontal gap δ for the case $h_1/r_1 = 1.0$, $h_2/r_2 = 0.8$, $\rho_V = 1.0$ and $\Delta z = 0.005(h_1 + h_2)$.

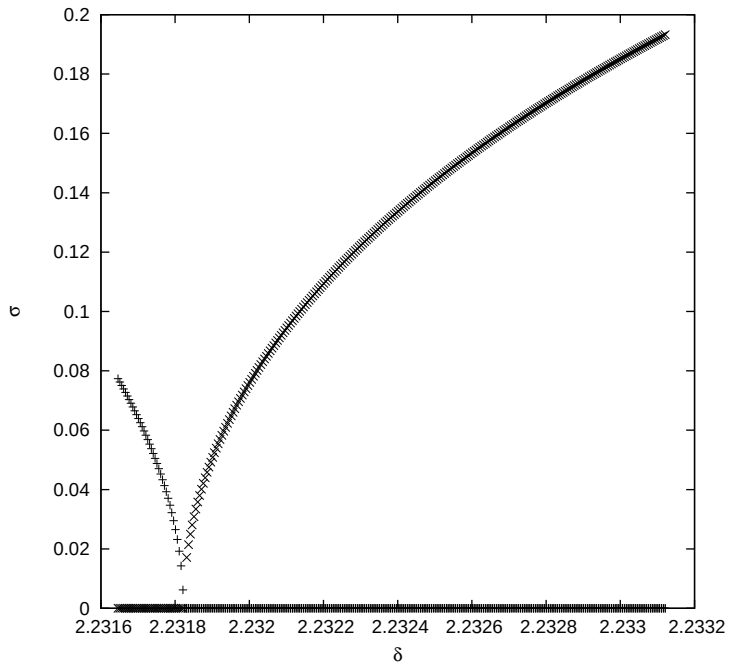

Figure 3.4: Growth rates, σ_r (shown by +) and frequencies, σ_i (shown by $\times$) vs horizontal gap δ for the case $h_1/r_1 = 1.0$, $h_2/r_2 = 0.8$, $\rho_V = 1.0$ and $\Delta z = 0.005(h_1 + h_2)$.

Figure 3.4 shows the results of the linear stability analysis by plotting σ against δ. In this plot, σ_r is shown with a + and σ_i is shown with a $\times$. We see that one of the mode's frequencies (σ_i) collapses to zero as the horizontal gap is decreased to $\delta = \delta_m$, matching to 4 decimal places the extrema in the curves for energy and angular impulse. At this value of δ, the growth rate becomes non-zero and increases further as δ is decreased. So we see from figure 3.4 that δ_m is indeed the critical gap that corresponds to the margin of stability. The geometry of this equilibrium state can be seen in figure 3.5.

This method was successful in all but a few cases. For these remaining cases it was found that repeating the calculation with the vortices being approximated by 13 singularities rather than 7 as used in *Reinaud & Dritschel* (2005) the margin of stability could be found successfully. This is due to the increased accuracy

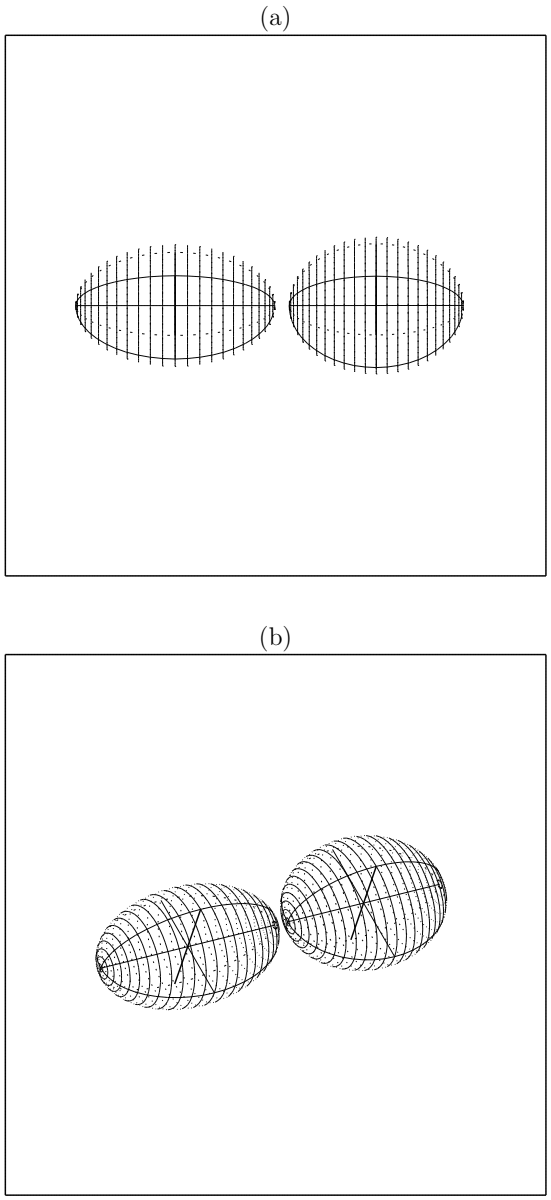

Figure 3.5: Ellipsoidal vortices at the margin of stability for the case $h_1/r_1 = 1.0$, $h_2/r_2 = 0.8$, $\rho_V = 1.0$ and $\Delta z = 0.005(h_1 + h_2)$. Viewed at co-latitude 60° and longitude (a) 0° and (b) 30°. Minor ellipsoid axes shown by bold line, middle and major axes shown by thin lines. Ellipses drawn on the surface perpendicular to the major axes using dashed lines for the back sides.

Parameter	Min	Max	Increment
h_1/r_1	0.4	1.2	0.2
h_2/r_2	0.4	1.2	0.2
ρ_V	0.2	1.0	0.2
δz	0.0*	0.8	0.2

Table 3.2: Chosen parameter space where h_i/r_i, $i = 1, 2$ is the height-to-width aspect ratio of each vortex, ρ_V is the volume ratio V_1/V_2 and δz, the vertical offset, is a fraction of the sum of the half-heights, i.e $\Delta z = \delta z(h_1 + h_2)$. * In these cases the ellipsoids were not in exact vertical alignment but had $\delta z = 0.005$ since perfectly symmetric equilibria may lead on to a spurious branch of solutions, see *Reinaud & Dritschel* (2005)[37].

obtained by using a higher number of point vortices as shown in table 3.1.

3.1.3 Parameter space

ELM was an ideal tool to use for such an investigation as that of *Reinaud & Dritschel* (2005). Its simplicity combined with its accuracy provide excellent estimates for the stability margins of 5625 cases. It is our intention to investigate the nonlinear behaviour of these pairs of vortices under time evolution. Since ELM filters all nonlinear deformations of the vortex it is not suitable for this study. Instead we use the CASL algorithm detailed in section 2.3. CASL however is computationally much more expensive than ELM therefore we need to reduce our parameter space from *Reinaud & Dritschel*'s 5625 cases by taking a sub-set of their parameter space (detailed in table 3.2) leaving us with 625 cases, still a very large sample to consider. The first unstable equilibrium state from each family is taken as the initial conditions for the calculation.

The geometry of the problem can be seen in figure 3.6. We set the PV to

Parameter	Value
Velocity field grid resolution	128^3
Fine to coarse grid ratio	4:1
Time step	0.05

Table 3.3: CASL parameters.

$q = 2\pi$ for both vortices. The computational domain is a box of $2\pi^3$ (after the rescaling of z by f/N) with periodic boundaries in x, y and z. It is necessary to minimise the influence of the periodic images of the vortices on the interaction (see *Dritschel & Macaskill* (2000)[9]). We scale the initial conditions to fit inside a 2^3 box at the centre of the domain. We rescale the results back to their original dimensions for analysis so that all cases have the same total strength,

$$\iiint q \mathrm{d}V = 8\pi^2/3. \tag{3.10}$$

We run the simulations up to $t = 60$. Recall that a spherical vortex of uniform PV, q, has a rotation period of $T = 6\pi/q$ meaning that these calculations last for approximately 20 vortex revolutions. The initial CASL parameters are given in table 3.3. The surgical cut-off scale δ_{min} which is the minimum distance two contours containing equal PV can be to each other before surgery is performed is given by $\delta_{min} = (\mu^2 L)/4$ where μL is approximately the spacing between adjacent nodes and L is the characteristic length scale of the PV structures in the flow. For our calculations $\delta_{min} = 0.005$. Δt is set $\pi/10q = 0.05$. The results of these calculations are presented in the next section.

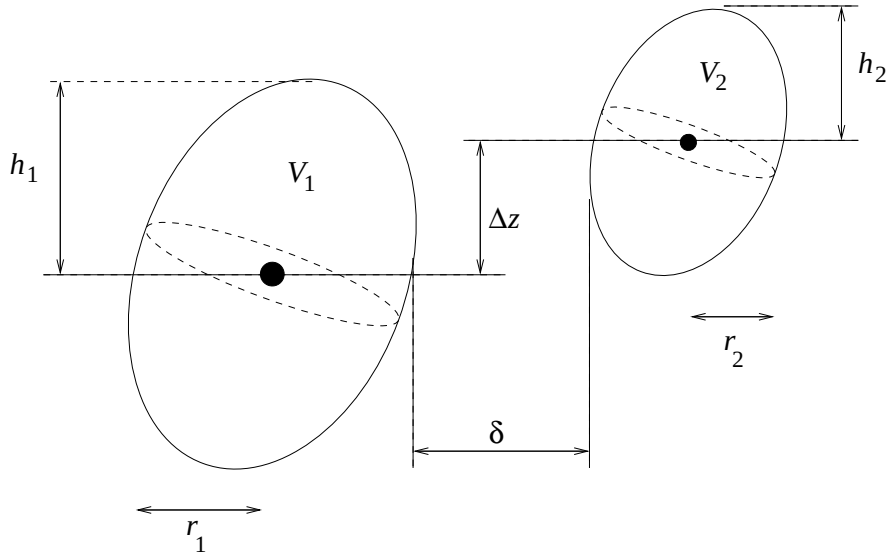

Figure 3.6: Geometry of initial conditions. Vortices ($i = 1, 2$) have vertical half-heights h_i, horizontal radii r_i and volumes V_i. They are offset in the vertical by a distance Δz such that $\Delta z = \delta z(h_1 + h_2)$ and separated in the horizontal by a distance δ.

3.2 Results

CASL outputs data sets for all PV contours in the domain at each specified time interval, this being 1 time unit in our case. We perform two operations on these contour sets to extract useful information. Firstly, we use a vortex identification procedure to identify the vortices present as contiguous 3D structures. Then we use a vortex properties analysis code to analyse the vortices that have been identified. This latter procedure returns data for the mean-radius (obtained from the cube root of the volume), the centroid position, the height-to-width aspect ratio and values describing the best fit of the vortex to an ellipse. This procedure calculates the volume of vortices by contour integration and was modified in this work to similarly compute the vortices self-energies.

Merger type	$\hat{V}_1$	$\hat{V}_2$
Elastic Interaction (EI)	1	1
Partial Straining Out (PSO)	1	< 1
Complete Straining Out (CSO)	1	0
Partial Merger (PM)	> 1	< 1
Complete Merger (CM)	> 1	0

Table 3.4: Criteria for classification of vortex interactions.

3.2.1 Classification of interactions

In previous studies, several methods of classifying vortex interactions have been introduced. The most relevant to our study is the one introduced in *Dritschel & Waugh* (1992)[17]. We define

$$\hat{V}_j = \frac{V_{f_j}}{V_{i_j}}, \qquad (j = 1, 2) \tag{3.11}$$

where V_{i_j} and V_{f_j} are respectively the initial and final volumes of vortex j, ordered by volume. The vortex interaction can now be classified according to table 3.4.

In the elastic interaction (EI) scenario, no PV is exchanged and both vortices retain their original volume. When partial straining-out (PSO) occurs, filaments of PV are 'strained out' from vortex 2. These filaments are not consumed by vortex 1 however, so vortex 1 retains its original volume and vortex 2 loses volume. Complete straining-out (CSO) is where the second vortex is entirely destroyed by the first vortex. Vortex 2 is reduced to filaments and other small scale debris, none of which is consumed by the first vortex which still retains its original volume. In partial merger (PM) the vortices temporarily merge together then re-separate. After separation, vortex 2 is seen to have reduced in volume whereas vortex 1 has grown in volume. This volume has been transferred from vortex 2 to vortex

1. When complete merger (CM) occurs, vortex 2 has been entirely consumed by vortex 1.

The resulting interaction regime for each simulation is plotted in figure 3.7. We find that for $\rho_V = 0.2$, 92% of cases involve PSO with the remaining 8% being PM. For higher initial volume-ratios, interactions are predominantly PM. For $0.4 \leq \rho_V \leq 1.0$, 85% of cases result in PM, 9.8% of cases are PSO and 4.4% of cases are CM. Of the cases that result in a CM regime, 72.7% of these occur when $\rho_V = 1.0$ and 72.7% occur when $h_1/r_1 = h_2/r_2$. Partial straining-out does not occur at all for the equal-volume cases in this parameter space. Also we note that no instances of complete straining-out or elastic interaction occur in this parameter space either.

It is interesting to observe that when one vortex is considerably larger than the other, PV is not transferred but 'strained out' of the smaller vortex. This has been shown to occur also in two-dimensional cases. *Dritschel* (1995)[6] found that whilst the smaller vortex always decreased in size, the larger vortex only increased in size (i.e. displayed PM or CM) for area ratios $\alpha \gtrsim 0.6$ meaning that if the vortices were originally very different in size the smaller vortex was subject to straining-out. One explanation of the results seen both here and in *Dritschel* (1995) is that for a large difference in size, i.e. a small ρ_V, the small vortex is weak relative to the large vortex. It cannot adapt its shape to get close to the large vortex. The smaller vortex is then simply strained-out by the larger vortex. On the other hand for a larger ρ_V, the smaller vortex is strong enough to deform without being strained-out thus it can deform so as to touch the larger vortex. The most common behaviour then is for the vortices to merge into an asymmetric – 'dumbbell'-shaped – structure which eventually breaks asymmetrically with the small vortex having transferred some of its PV to the large vortex.

We now illustrate some examples of the simulations with three-dimensional snapshots of the flow at various time frames. In figure 3.8 we show four time

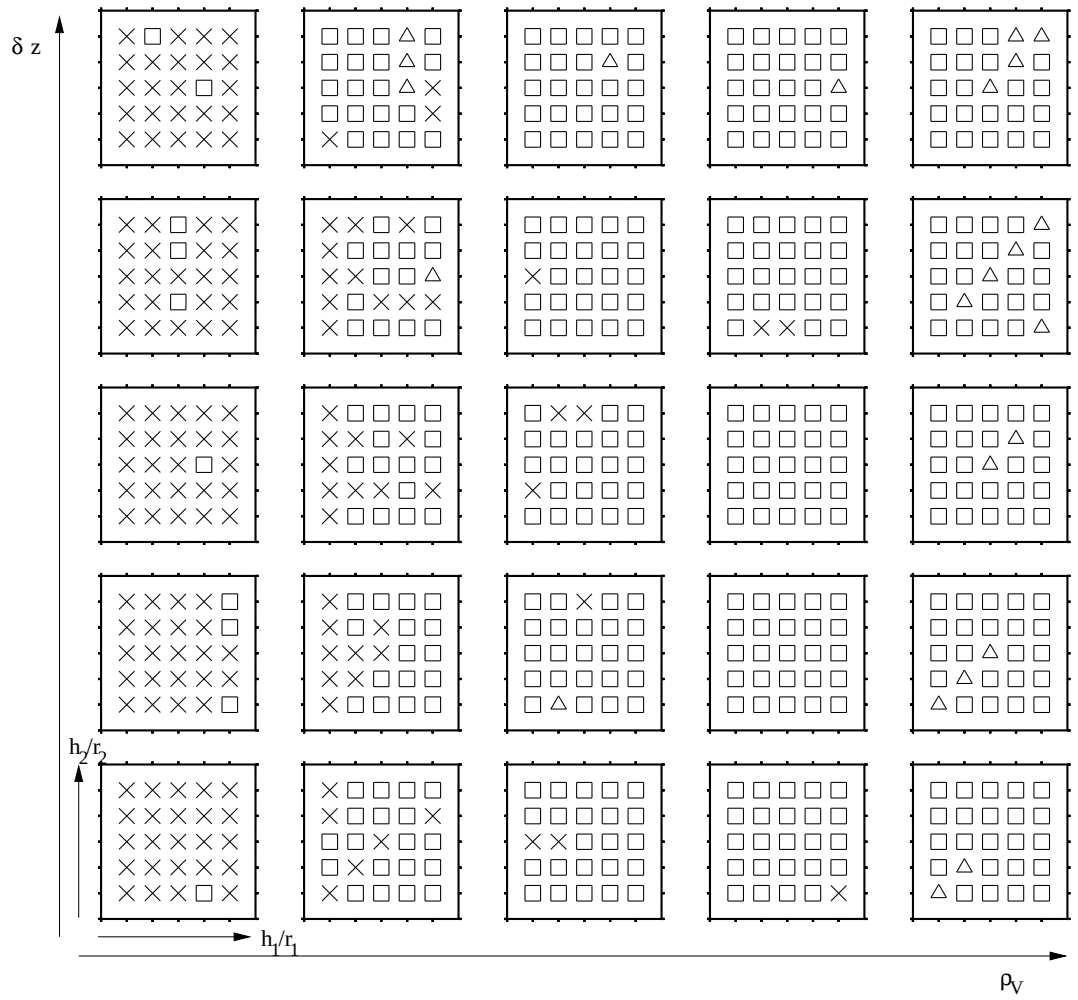

Figure 3.7: Interaction regimes for every simulation. Each graph has $0.2 \leq h_1/r_1 \leq 1.4$ on the horizontal axis and $0.2 \leq h_2/r_2 \leq 1.4$ on the vertical axis. Each separate graph in the horizontal increments ρ_V by 0.2 starting with $\rho_V = 0.2$ on the left. Each separate graph in the vertical increments δz by 0.2 starting with $\delta z = 0.005$ at the bottom. Partial straining-out is denoted by an $\times$, partial-merger by $\square$ and complete-merger by $\triangle$.

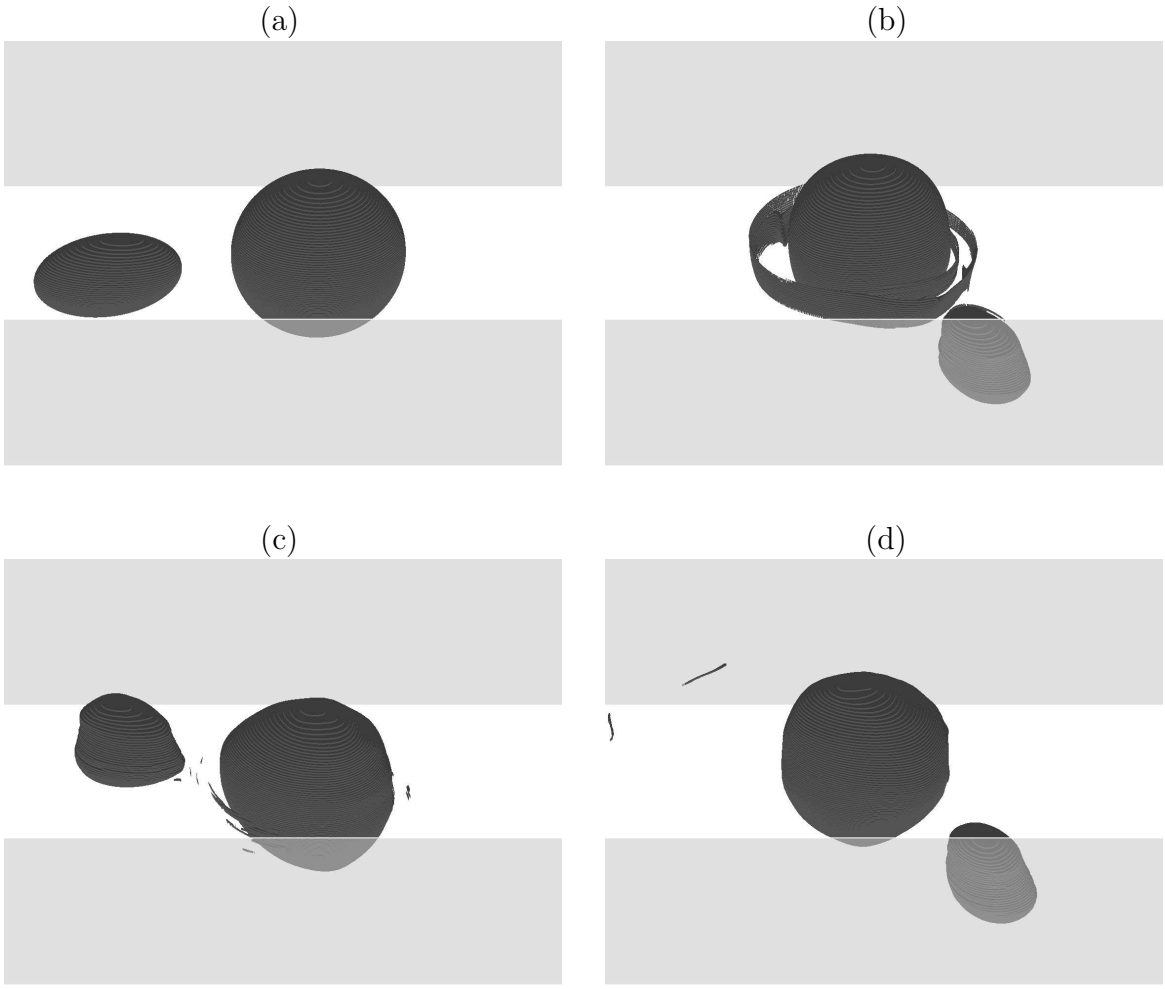

Figure 3.8: Vortex evolution in a PSO regime. $h_1/r_1 = 0.8$, $h_2/r_2 = 1.0$, $\rho_V = 0.2$ and $\delta z = 0.2$. Time frames shown are (a) $t = 0$, (b) $t = 14$, (c) $t = 40$ and (d) $t = 60$. Viewing angle is 60° from the vertical and horizontal scale is ± 1.5 centred around the origin of the domain. Light grey areas show front and back walls of the box which spans the full height of the PV distribution.

frames from an interaction in a partial straining out regime. The initial conditions are $h_1/r_1 = 0.8$, $h_2/r_2 = 1.0$, $\rho_V = 0.2$ and $\delta z = 0.2$. At time $t = 7$ filaments begin to be stripped away from the smaller vortex, these filaments orbit the larger vortex but do not merge with it. By $t = 60$ the smaller vortex has lost 5% of its original volume and now has $h/r = 0.92$. The volume and aspect ratio of the larger vortex has remained unchanged throughout.

The simulation seen in figure 3.9 has initial conditions $h_1/r_1 = 1.0$, $h_2/r_2 = 0.4$, $\rho_V = 1.0$ and $\Delta z/(h_1 + h_2) = 0.2$. In this situation the volume of PV transfered between the vortices is sufficient to classify this interaction as partial-merger. At $t = 7$ the two initial vortices merge into a "dumbbell" shaped configuration with an effective aspect-ratio of 0.58. At $t = 13$ the "dumbbell" vortex begins to eject filaments and at $t = 21$ it splits into two large scale vortices with a volume-ratio of 0.53. The larger of these vortices has $h/r = 0.79$ and the smaller has $h/r = 0.57$. It is apparent that these small scale structures are ejected by the larger vortex between $t = 21$ and $t = 40$ as its volume at $t = 40$ is 91% of what it was at $t = 21$. The smaller vortex, on the other hand, has grown by 0.4% during this time. At $t = 60$ the number of structures present has decreased. At this end time the larger vortex has grown by 2% over its original volume at $t = 21$ whereas the smaller vortex has 2% less volume than at $t = 21$. The final volume ratio of these two main vortices is 0.56.

One other interesting example is shown in figure 3.10. On first inspection one would expect this interaction to belong in the CM class and indeed displays behaviour described in *Waugh* (1992)[47] of a 'merger' scenario where the central vortex ellipse has an aspect ratio greater than 3. However using the criteria set out in table 3.4 this interaction is classified as PM due to the large quantity of filaments ejected. The initial vortices merge by $t = 2$ forming a central vortex of $h/r = 0.97$. Figure 3.10(b) shows filaments forming at both vertical apexes of the central vortex at $t = 14$. At $t = 16$ these filaments begin to separate from the

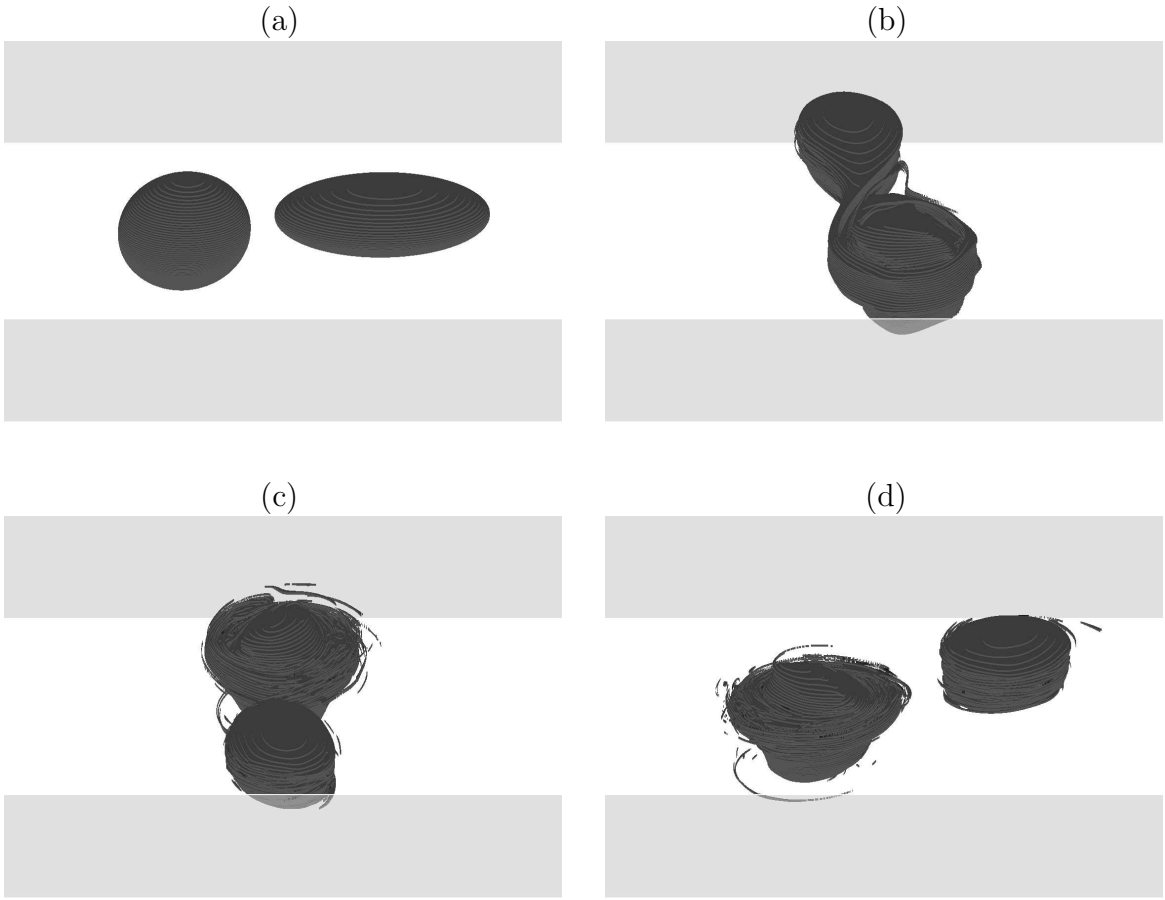

Figure 3.9: Vortex evolution in a PM regime. $h_1/r_1 = 1.0$, $h_2/r_2 = 0.4$, $\rho_V = 1.0$ and $\delta z = 0.2$. Time frames shown are (a) $t = 0$, (b) $t = 14$, (c) $t = 40$ and (d) $t = 60$. Viewing angle is 60° from the vertical and horizontal scale is ± 1.5 centred around the origin of the domain. Light grey areas show front and back walls of the box which spans the full height of the PV distribution.

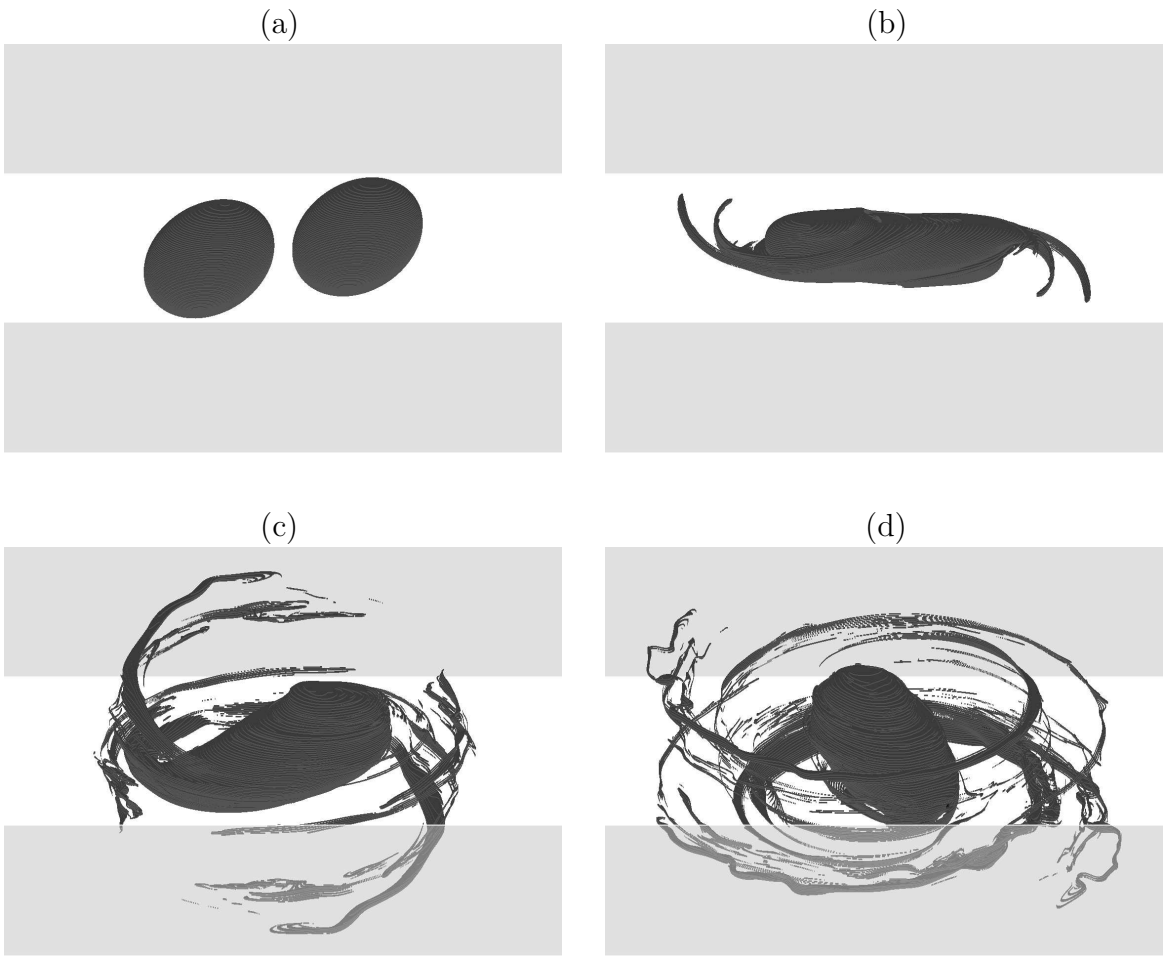

Figure 3.10: Vortex evolution in a PM regime. $h_1/r_1 = 1.2$, $h_2/r_2 = 1.2$, $\rho_V = 1.0$ and $\delta z = 0.2$. Time frames shown are (a) $t = 0$, (b) $t = 14$, (c) $t = 40$ and (d) $t = 60$. Viewing angle is 60° from the vertical and horizontal scale is ± 2.0 centred around the origin of the domain. Light grey areas show front and back walls of the box which spans the full height of the PV distribution.

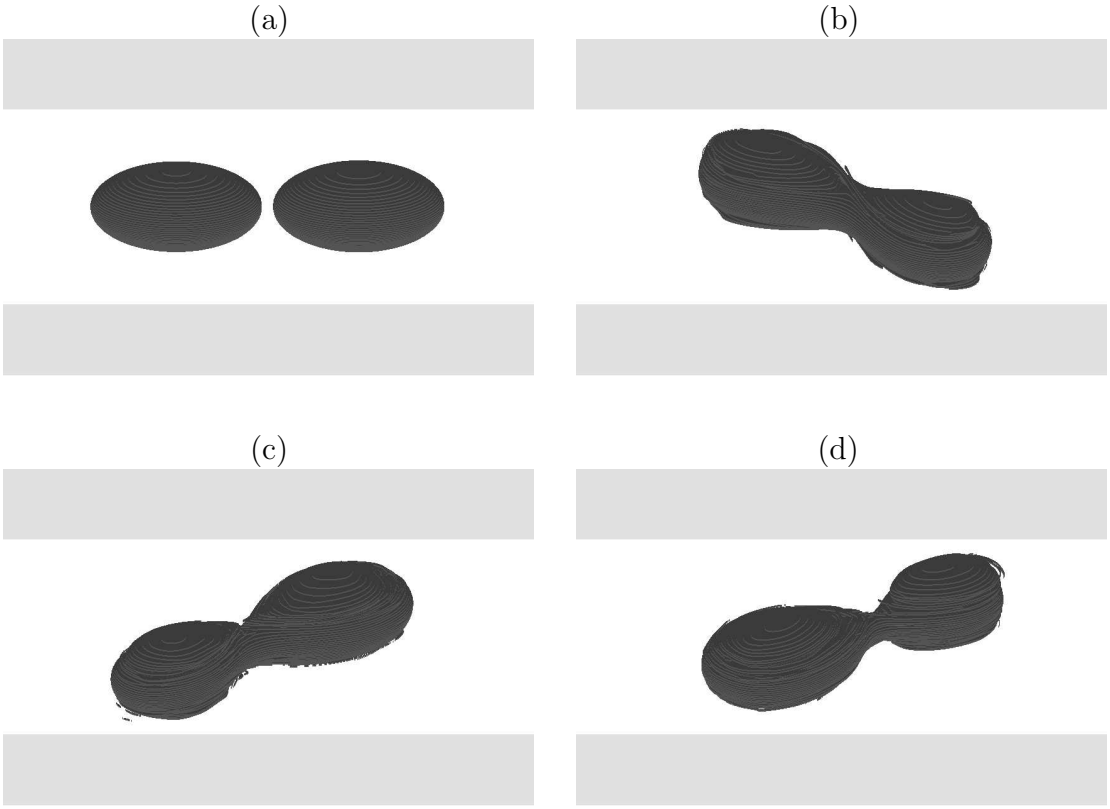

Figure 3.11: Vortex evolution in a CM regime. $h_1/r_1 = 0.6$, $h_2/r_2 = 0.6$, $\rho_V = 1.0$ and $\delta z = 0.005$. Time frames shown are (a) $t = 0$, (b) $t = 14$, (c) $t = 40$ and (d) $t = 60$. Viewing angle is 60° from the vertical and horizontal scale is ± 2.0 centred around the origin of the domain. Light grey areas show front and back walls of the box which spans the full height of the PV distribution.

central vortex. By $t = 40$ the central vortex has reduced to 90% of its volume at $t = 2$ and h/r is reduced to 0.89. At the end time, $t = 60$, the central vortex has further decreased in volume to 81% of that at $t = 2$ and its h/r is now 0.81.

In figures 3.11 and 3.12 we show flow snapshots of two cases diagnosed to be complete-merger. It is apparent in both of these cases that CM has not occurred in full. The snapshot at $t = 60$ for the nearly vertically aligned case $h_1/r_1 = 0.6$, $h_2/r_2 = 0.6$, $\rho_V = 1.0$ and $\delta z = 0.005$, that is figure 3.11(d) show two distinct vortices which are however, still connected by a thin filament, meaning that

computationally these structures are still counted as a single vortex. In this case the initial vortices merge at time $t = 3$ and again begin ejecting filaments at $t = 15$. The volume of PV lost to filamentary ejection here is small however, and the volume of the joined pair at $t = 60$ is 97% the volume of the original merged pair at $t = 3$.

Figure 3.12 shows another example of a case diagnosed at CM, here for $h_1/r_1 = 0.8$, $h_2/r_2 = 0.8$, $\rho_V = 1.0$ and $\delta z = 0.2$. Inspection of the flow shows that whilst the vortices are still merged at $t = 60$, they are configured in a "dumbbell" shape such as seen at earlier times in other cases, for example, in figure 3.9(b). Once again here we see a familiar pattern in the interaction. The initial vortices merge at time $t = 2$ and begin ejecting filaments at $t = 14$. The vortices stay merged in a "dumbbell" configuration throughout the evolution. The merged pair's volume at the end time $t = 60$ is again 97% of the volume it was when the vortices initially merged.

These last two examples have shown that complete merger, an already rare occurrence, is in fact rarer still since some cases that have been diagnosed as CM may eventually become PM once filamentary connections between vortices break and dumbbell structures re-separate.

Another interesting point to address is why CM is more frequently seen for vortices of equal height-to-width aspect-ratio. Figure 3.13 shows the interaction of the vortices with $h_1/r_1 = 1.2$, $h_2/r_2 = 0.4$, $\rho_V = 0.8$ and $\delta = 0.8$, i.e. two very different height-to-width aspect-ratios. The vortices merge by $t = 2$ and stay merged until $t = 23$, when 29% of the volume of the main structure is broken away to form a new secondary vortex. As can be seen in figure 3.13(b) the merger of the oblate (flat) vortex with the prolate (tall) vortex near the top of the prolate vortex has caused the bottom of the prolate vortex to become unstable and it is this part of the structure that is disconnected from the main structure at $t = 23$. This occurs similarly in the example shown in figure 1.4. It could be concluded

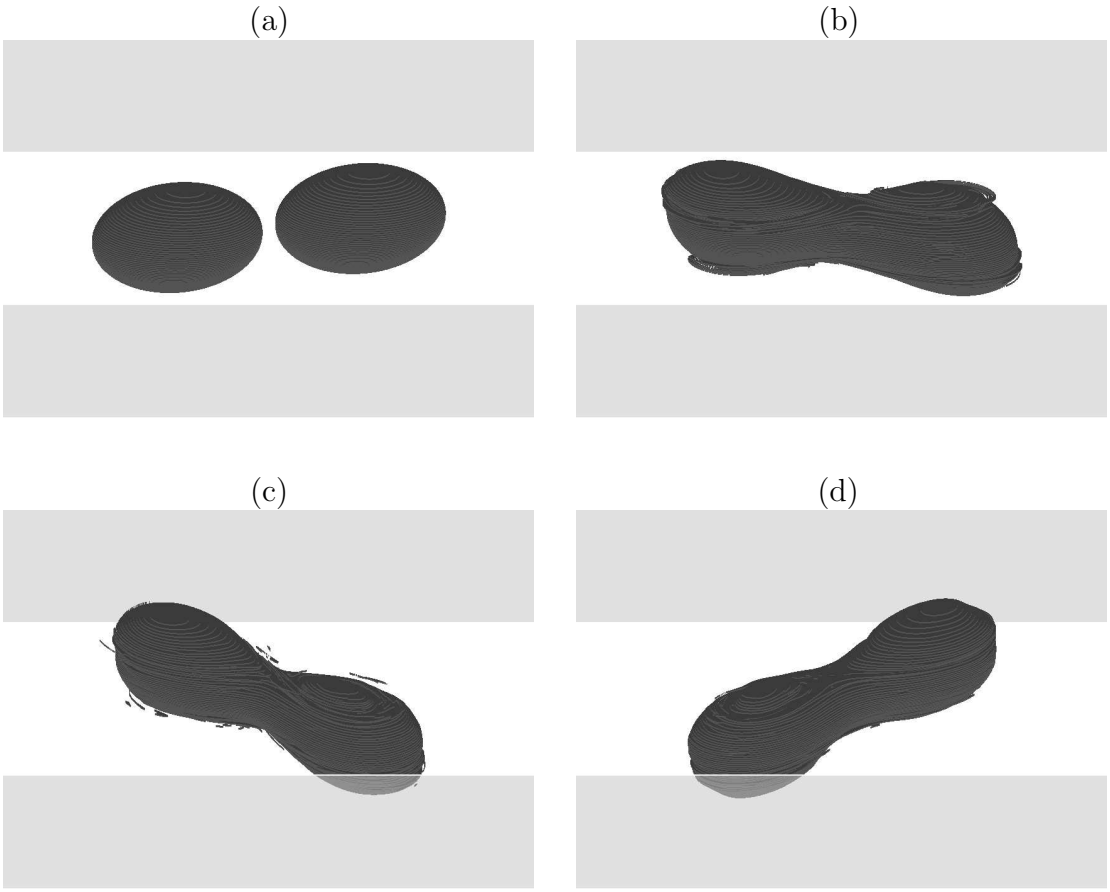

Figure 3.12: Vortex evolution in a CM regime. $h_1/r_1 = 0.8$, $h_2/r_2 = 0.8$, $\rho_V = 1.0$ and $\delta z = 0.2$. Time frames shown are (a) $t = 0$, (b) $t = 14$, (c) $t = 40$ and (d) $t = 60$. Viewing angle is 60° from the vertical and horizontal scale is ± 2.0 centred around the origin of the domain. Light grey areas show front and back walls of the box which spans the full height of the PV distribution.

then, that CM is less likely for disparate values of h/r due to this developing instability in the tall vortex.

3.2.2 Analysis over entire parameter space

As we have seen from the previous section, vortex interactions in this parameter space display a wide variety of behaviours all with significant complexity. We now turn our attention to the parameter space as a whole to seek trends in the interactions to help better understand their general aspects.

In large-scale geophysical turbulence the average inverse-cascade is an important spectral feature. To determine whether an analogous cascade exists in physical space we diagnose the self-energy (E_s) of a vortex of uniform PV, obtained by

$$E_s = -\frac{1}{2}\iiint q\psi^v \mathrm{d}V, \tag{3.12}$$

where ψ^v is the streamfunction induced by the vortex on itself and q is the PV. We note here that the total energy is dominated by the self-energies as the interaction-energy is small, see *Reinaud & Dritschel* (2005)[37] – in particular their figure 8.

Figure 3.14 shows four plots at times 0, 30, 40 and 60 of the number density of vortices of a given self-energy E_s and radius $r = (3V/4\pi)^{1/3}$ taken over the entire parameter space. We note the very high density of small scale vortices generated during the interactions such as can be seen in figure 3.10 for example.

The energy distribution, especially for the large vortices and to some extent the smallest vortices, is well approximated by the energy of a uniform sphere of PV (Q) – given by $E_s = (4\pi Q^2/15)r^5$ – the derivation of which follows.

The self-energy of a sphere can be obtained from the self-induced part of the

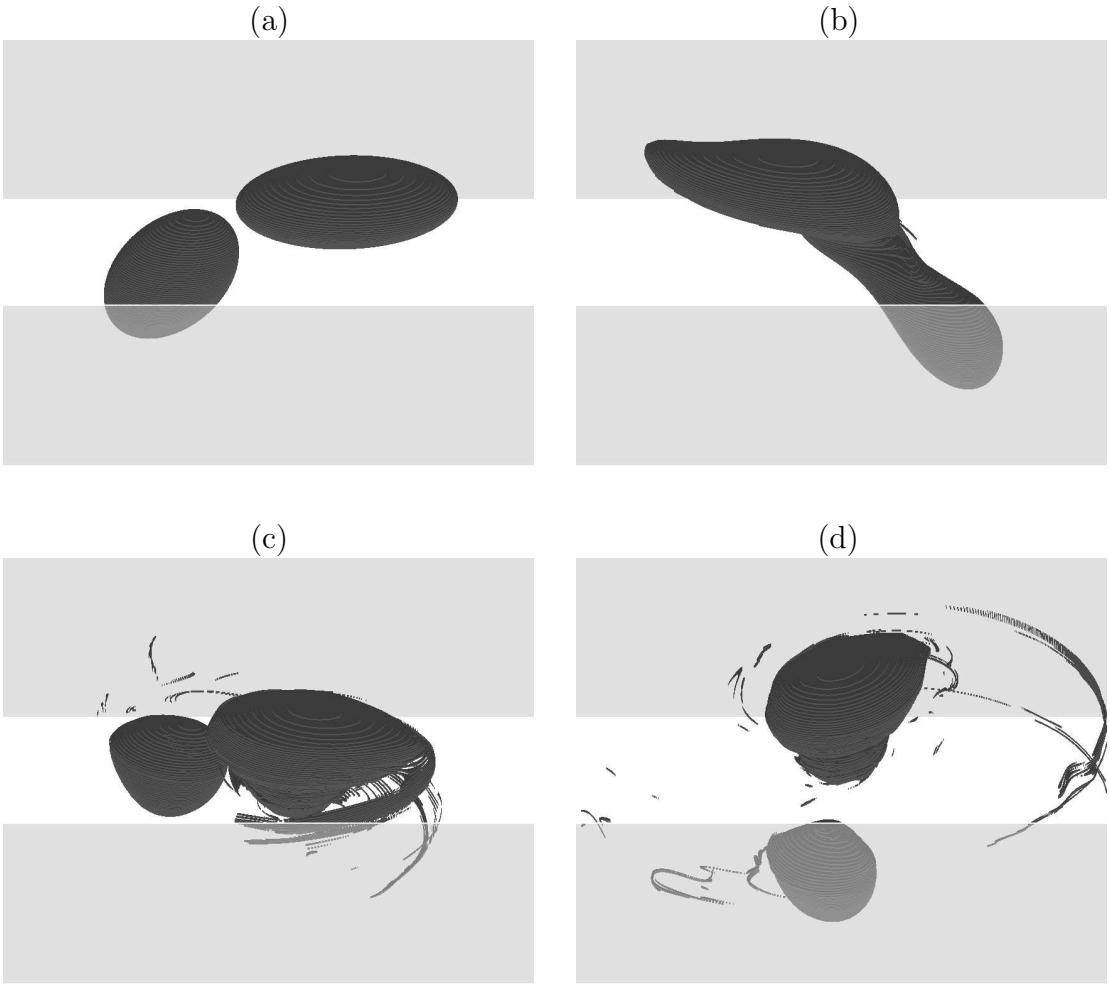

Figure 3.13: Vortex evolution in a PM regime. $h_1/r_1 = 1.2$, $h_2/r_2 = 0.4$, $\rho_V = 0.8$ and $\delta z = 0.8$. Time frames shown are (a) $t = 0$, (b) $t = 14$, (c) $t = 40$ and (d) $t = 60$. Viewing angle is 60° from the vertical and horizontal scale is ± 1.5 centred around the origin of the domain. Light grey areas show front and back walls of the box which spans the full height of the PV distribution.

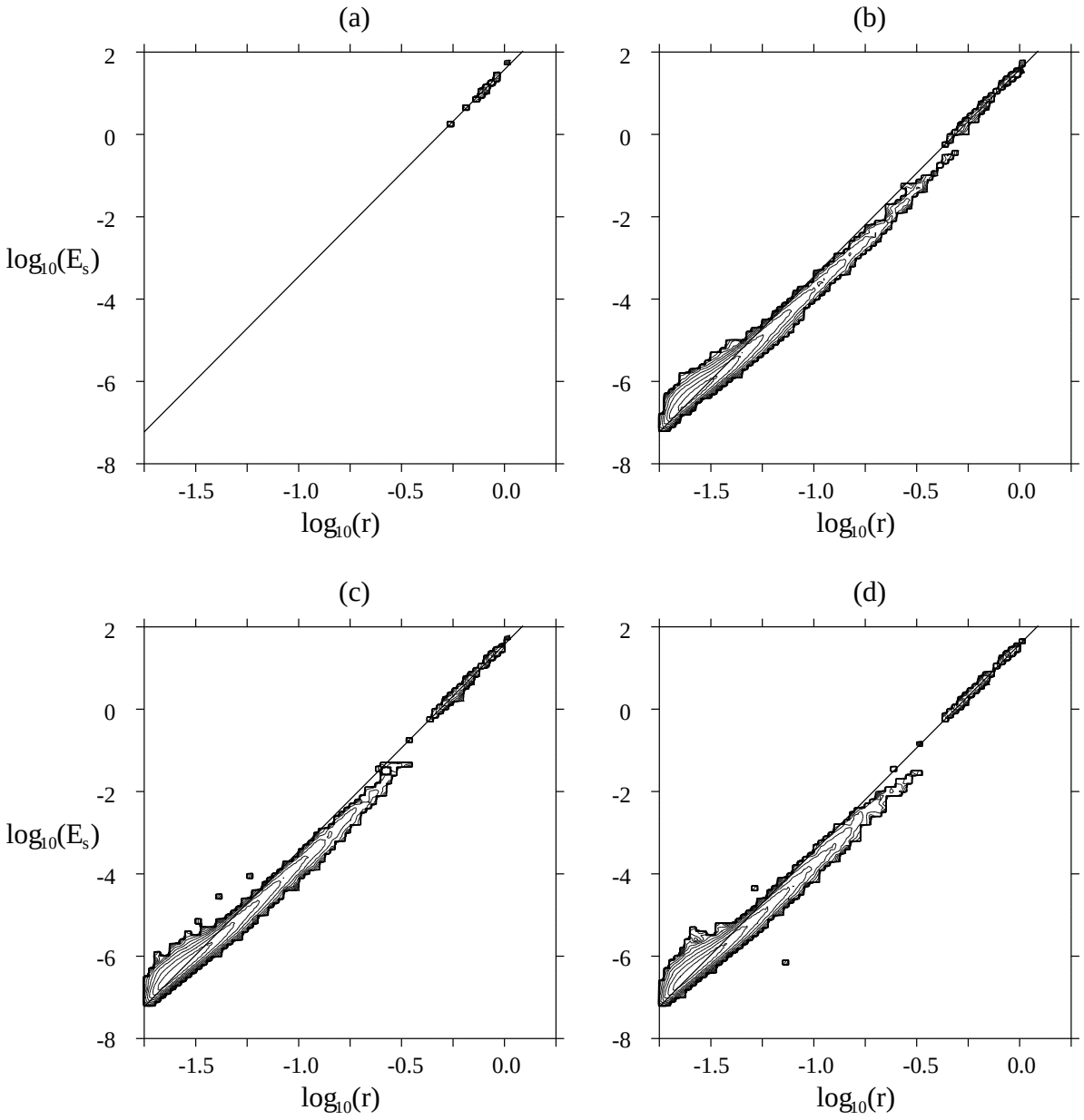

Figure 3.14: Contours of the number density (n) of vortices (contoured as $\log_{10} n$. The first (outermost) contour has $\log_{10} n = 0$, the innermost contour has $\log_{10} n = 11$, the contour increment is $\log_{10} \Delta n = 0.5$. 100 intervals were used in each direction, equally spaced in logarithmic scales. Times shown are (a) $t = 0$, (b) $t = 30$, (c) $t = 40$ and (d) $t = 60$. We add for reference the line corresponding to the energy of a sphere of PV Q, $E_s = (4\pi Q^2/15)r^5$.

Hamiltonian H^v by

$$E_s = 4\pi H^v = 4\pi.\frac{3}{5}R_F(r^2, r^2, r^2)\left(\frac{qV}{4\pi}\right)^2, \tag{3.13}$$

where R_F is an elliptic integral of the first kind thus

$$R_F(r^2) = \frac{1}{2}\int_0^\infty \frac{\mathrm{d}t}{\sqrt{t + r^2{}^3}}, \tag{3.14}$$

therefore

$$\begin{aligned} E_s = 4\pi.\frac{3}{5}.\underbrace{\frac{1}{2}\int_0^\infty \frac{\mathrm{d}t}{\sqrt{t + r^2{}^3}}}_{r^{-1}}.\left(\frac{Q\frac{4\pi}{3}r^3}{4\pi}\right)^2 \\ = 4\pi.\frac{3}{5}.\frac{1}{3^2}.\frac{r^6}{r}.Q^2 \\ = \frac{4\pi}{15}Q^2r^5. \end{aligned} \tag{3.15}$$

The line corresponding to equation 3.15 is included in figure 3.14 for reference. Since the streamfunction in equation 3.12 is quadratic one would expect such a power law dependence, however it is remarkable how well the data fit to the energy of a spherical vortex.

An interesting feature of figure 3.14 is the formation of a gap in the distribution of the self-energy in the region $10^{-0.6} \leq r \leq 10^{-0.4}$, i.e. $0.25 \leq r \leq 0.40$. It would appear that in this parameter space, vortices of this size cannot survive the interaction. We note that the energy levels for vortices in this range at earlier times are considerably less than those of spherical vortices indicating that these vortices have been highly deformed. There are two possibilities as to the fate of these intermediate sized structures, they are either destroyed by shear effects, or re-absorbed into the larger vortices.

We attempt to analyse the shear effects on a vortex by considering a simple case using point vortices. Initially we take two point vortices with strengths $\Gamma_1 = \Gamma_2 = \Gamma$ so the total strength is 2Γ. The point vortices are initially situated a distance d apart such that they are equidistant from the origin (and hence the global centroid) $x = 0$. Thus we can say $x_1 = -d/2$ and $x_2 = d/2$. The angular momentum of the system will be conserved around the global centroid, the global centroid itself will also be conserved by conservation of linear impulses. Initially the angular momentum is given by

$$J = \Gamma_1 x_1^2 + \Gamma_2 x_2^2 = \frac{\Gamma d^2}{2}. \tag{3.16}$$

We now say that after an "interaction" the volume of vortex 1 has increased by a factor λ and, since $\Gamma = qV$, we can also say vortex 1 has increased its strength by the same factor. So now

$$\tilde{\Gamma}_1 = \lambda\Gamma, \tag{3.17}$$

and by conservation of total strength

$$\tilde{\Gamma}_2 = 2\Gamma - \lambda\Gamma = (2 - \lambda)\Gamma. \tag{3.18}$$

The point vortices are now at new positions $\tilde{x}_1$ and $\tilde{x}_2$ such that the new distance between them is $\tilde{d} = \tilde{x}_2 - \tilde{x}_1$. The angular momentum can now be expressed as

$$J = \tilde{\Gamma}_1 \tilde{x}_1^2 + \tilde{\Gamma}_2 \tilde{x}_2^2 = \frac{\Gamma d^2}{2}. \tag{3.19}$$

Remembering that $\tilde{\Gamma}_1 \tilde{x}_1 + \tilde{\Gamma}_2 \tilde{x}_2 = 0$ one can derive an expression for $\tilde{d}$ in terms of the original gap d and the scale factor λ:

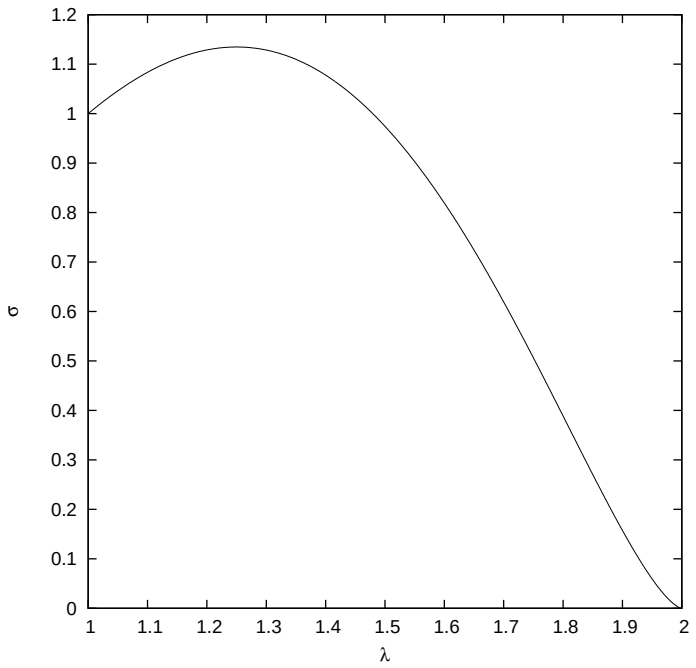

Figure 3.15: Strain on point-vortex 2 by point-vortex 1 against scale factor λ. $\Gamma = 1$, $d = 1$

$$\tilde{d} = \sqrt{\frac{d^2}{\lambda(2-\lambda)}}. \tag{3.20}$$

This can then be used to calculate the strain imposed by vortex 1 on vortex 2 by

$$\sigma = \lambda\Gamma \left(\frac{d^2}{\lambda(2-\lambda)} \right)^{-3/2}, \tag{3.21}$$

as defined in *McKiver & Dritschel* (2003)[30], see in particular their equation 27.

The variation of σ with λ can be seen in figure 3.15. The strain is seen to peak at $\lambda = 1.25$ indicating that there is a maximum strain associated with the generation of intermediate sized vortices. Whilst this value of λ does not correspond quantitatively to the scales seen in the 'gap' in figure 3.14, we see that there is indeed a maximum strain associated with intermediate sized structures emerging from interactions. This simplified model indicates that the vortices in

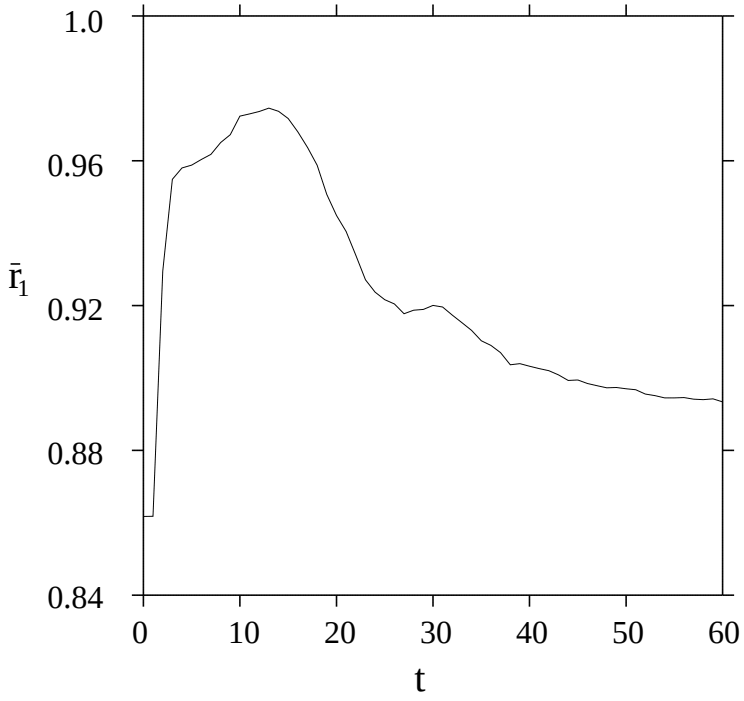

Figure 3.16: Time evolution of the average mean-radius of the largest vortex ($\bar{r}_1$).

this intermediate range are preferentially destroyed by high strains.

To provide further insight into whether intermediate sized vortices are strained-out or re-absorbed into the larger vortex, we plot the time evolution of the average radius of the largest vortex ($\bar{r}_1$) in figure 3.16. We conclude from this figure that since there are no prominent increases of mean-radius during the formation of the gap that the intermediate sized vortices are destroyed by shear effects as suggested earlier in this section. It is also interesting to notice that the smaller vortices are not destroyed by the same shear effects. This appears to be related to the fact that smaller vortices can get further away from the main vortex whilst still conserving angular impulse and thus, as seen in figure 3.15 for values of $\lambda > 1.5$, are subject to weaker strains.

Judging by the apparently even spacing between the contours for smaller vortices in figure 3.14 it appears that the number density of these smaller vortices is related to the radius by a power-law. We confirm this in figure 3.17 which shows

that the number density (n) for small vortices follows $n \propto r^{-4}$, as indicated by the reference line in the figure. This power-law dependency in the number density can be related to the slope of the inertial-range of the energy spectrum, as done in *Dritschel & Reinaud* (2002)[11]. As has already been shown, $E_s(r) \propto r^5$, thus the energy density $e(r) \propto r^5 n(r)$. Integrating we get

$$\int e(r)dr = \int n(r)E_s(r)dr \propto \int r^{-4}r^5 dr = \int r dr. \tag{3.22}$$

We relate r to the wave number k by $r \propto k^{-1}$, this changes the integral to

$$\int \left(\frac{1}{k}\right) \mathrm{d}\left(\frac{1}{k}\right) \sim \int \left(\frac{1}{k}\right) k^{-2} dk \sim \int k^{-3} dk \propto \int \mathcal{E}(k)\mathrm{d}k. \tag{3.23}$$

Thus the resulting power-law slope for this parameter space is therefore $\mathcal{E}(k) \propto k^{-3}$. This slope exactly matches the prediction of k^{-3} by *Charney* (1971)[5].

Another surprising result from figure 3.14 is the high quantity of small scale structures being generated during the interaction. It is not possible from this figure to ascertain the direction in which the energy is transfered. We define F as the integral with respect to radius of the self-energy of all vortices in the parameter space at a time t. Thus at a given r we can see the sum of the self-energy contained in scales less than that value of r allowing us to have a quantitative view of the transfer of self-energy across the parameter space

$$F = \frac{1}{n} \int E_s(r)\mathrm{d}r, \tag{3.24}$$

where n is the number of simulations, i.e. $n = 625$.

In figure 3.18 which shows the variation of $F(r)$ with r we see two distinct regions to the $t = 60$ curve. The initial increase in $F(r)$ between $r = 0.5$ and $r = 0.76$ shows that the amount of energy contained at scales below $r = 0.76$

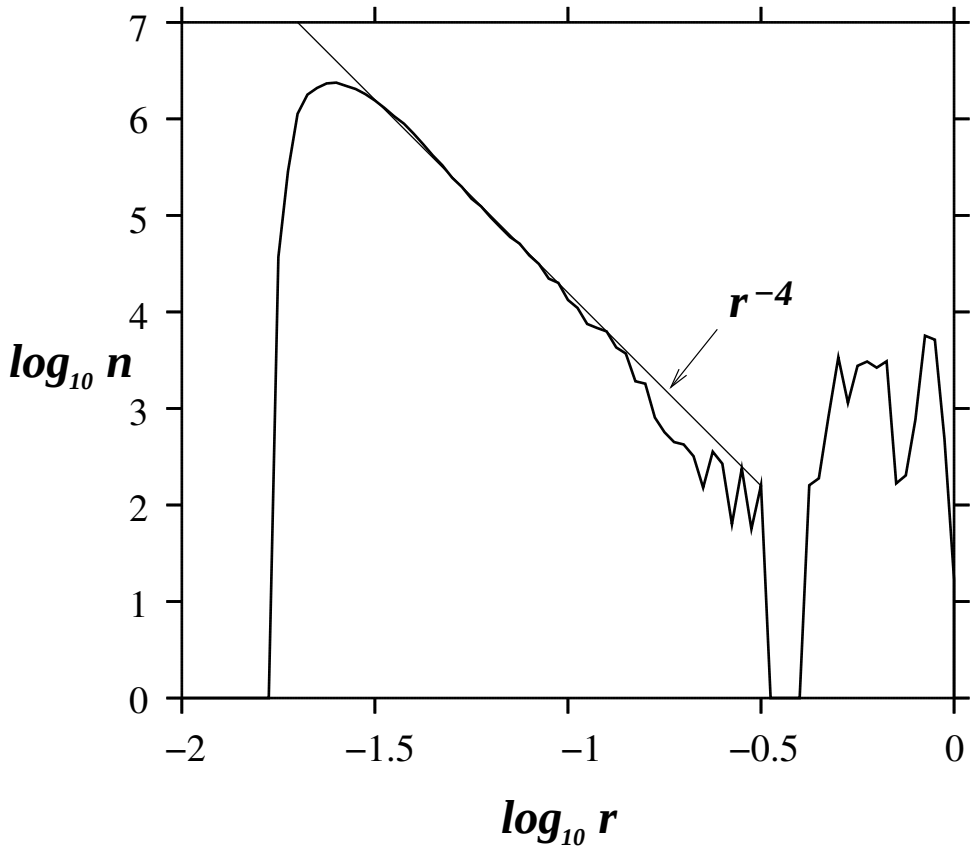

Figure 3.17: Number density of vortices as a function of radius. As in the previous figure we use 100 intervals in the direction of $\log_{10} r$. This is at $t = 60$. We add for reference the slope r^{-4}.

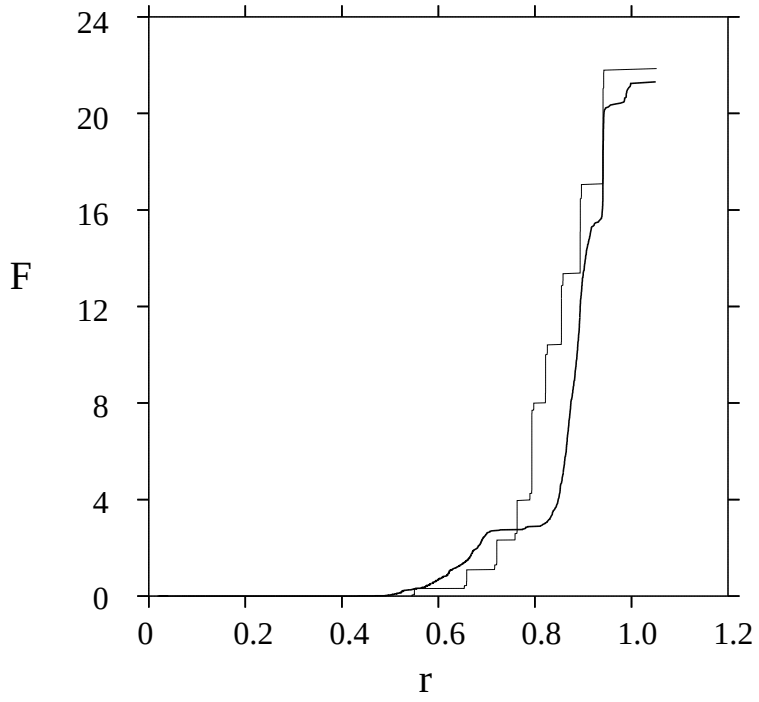

Figure 3.18: F plotted against r where $F = (1/n) \int E_s \mathrm{d}r$ at times $t = 0$ (thin line) and $t = 60$ (bold line).

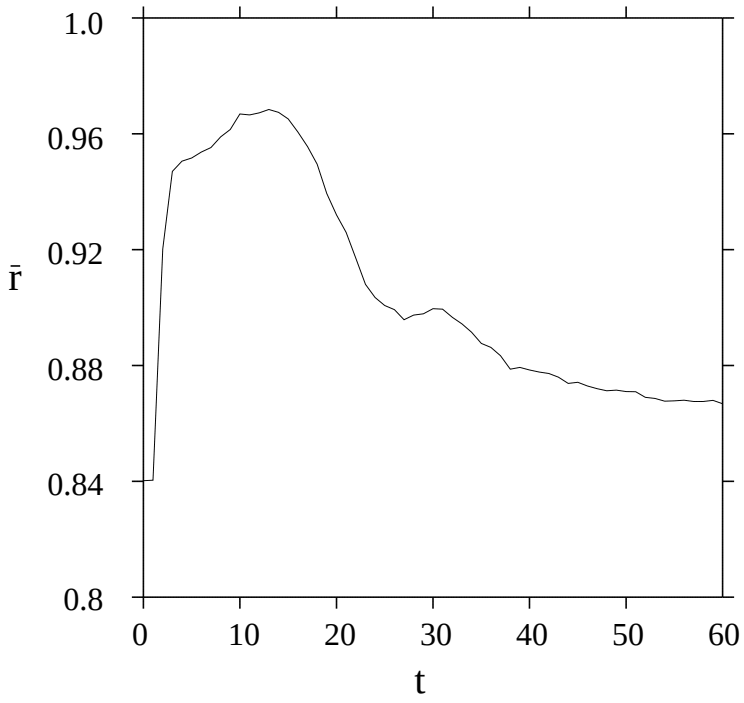

Figure 3.19: Time evolution of the energy-weighted mean-radius ($\bar{r}$).

has increased. For $r > 0.76$ the curve is shifted to the right meaning that the self-energy is contained at larger scales i.e. it has undergone an inverse-cascade.

To investigate the mean spatial scale carrying energy we define the energy-weighted mean-radius ($\bar{r}$) at a time t as

$$\bar{r} = \frac{\sum_{i=1}^{m} E_{si} r_i}{\sum_{i=1}^{m} E_{si}}, \tag{3.25}$$

where m is the total number of vortices present in the entire parameter space at time t. In figure 3.19 we show the variation of $\bar{r}$ with time. Over the first 14 time units, $\bar{r}$ increases showing that in most cases vortex merger is occurring. After $t = 14$, $\bar{r}$ begins to decrease as the vortices separate and begin to eject filaments. We see a convergence of $\bar{r}$ to 0.87 by $t = 50$ showing that the mean-radius has, on average, increased by 3.5%.

We define $\bar{r}_0$ to be the value of $\bar{r}$ at time $t = 0$. Then, at any time, we can

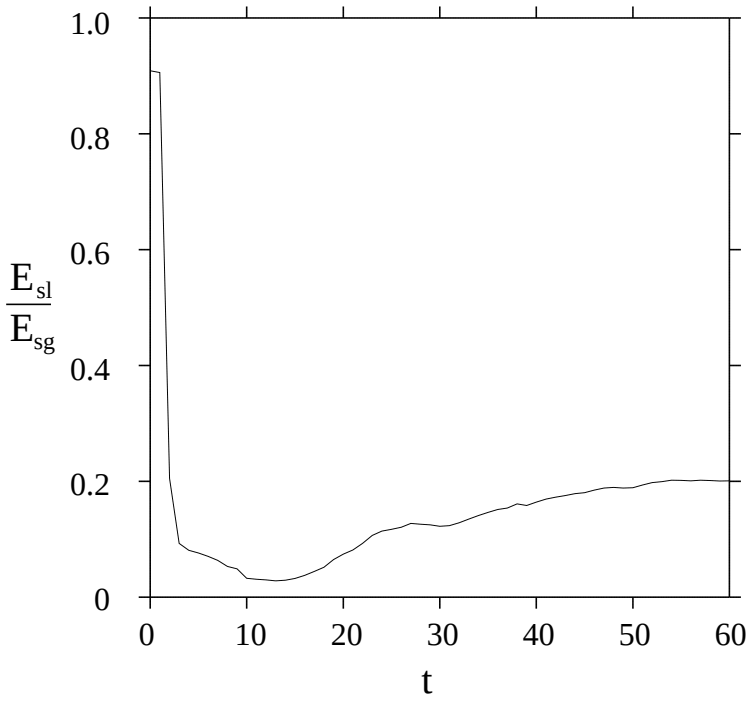

Figure 3.20: Time evolution of E_{sl}/E_{sg}.

define E_{sl} as being the average self-energy of all vortices in the parameter space at that time that have a mean-radius r such that $r < \bar{r}_0$. Similarly we define E_{sg} to be the average self-energy of all vortices in the parameter space at the same time that satisfy $r > \bar{r}_0$. By plotting the time evolution of E_{sl}/E_{sg} in figure 3.20 we obtain a qualitative summary of the energy transfers. Note that in figure 3.20 at $t = 0$, E_{sl}/E_{sg} is not equal to 1. This is due to the fact that we only have a discrete sample of initial conditions. As the number of cases considered tends to ∞ we would expect $(E_{sl}/E_{sg})_{t=0} \rightarrow 1.0$.

We see a rapid decrease in E_{sl}/E_{sg} at early times, once again showing that an inverse cascade of self-energy is occurring. However, at $t = 14$ E_{sl}/E_{sg} begins to increase again when smaller scale structure start to be ejected. By the final time ($t = 60$), 70% of the self-energy is contained in structures that have $r > \bar{r}_0$. We show values of E_{sl} and E_{sg} in table 3.5.

Figure 3.21 shows the growth of the largest vortex between $t = 0$ and $t = 60$

Time (t)	E_{sl}	E_{sg}
0	10.41	11.45
14	0.73	23.83
30	2.49	20.32
40	3.09	18.84
60	3.30	17.09

Table 3.5: Values of E_{sl} and E_{sg} at times 0, 14, 30, 40 and 60.

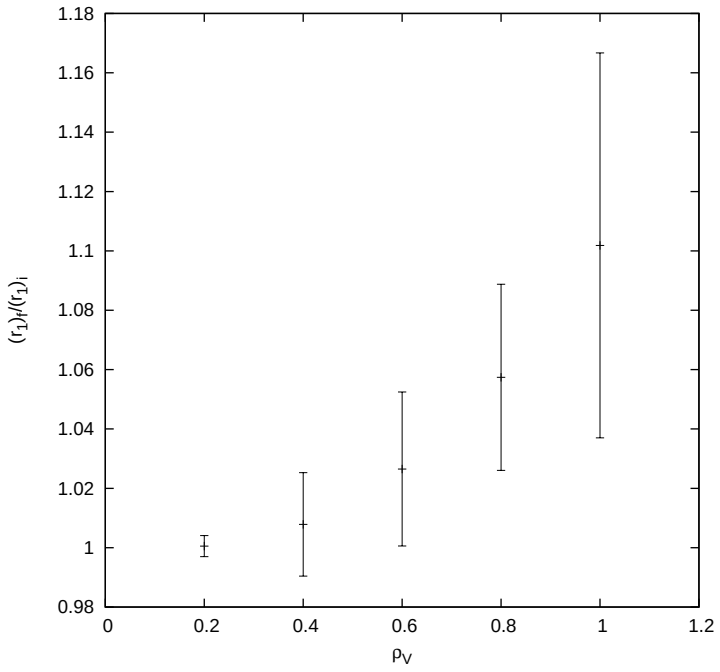

Figure 3.21: Ratio of the radius of the largest vortex at $t = 60$ ($(r_1)_f$) to the radius of the largest vortex at $t = 0$ ($(r_1)_i$) plotted against initial volume-ratio (ρ_V), ensemble averaged over all initial height-to-width aspect-ratios and vertical offsets. The error-bars here are 2 standard-deviations high.

depending on the initial volume-ratio; this is averaged over all height-to-width aspect-ratios and vertical offsets. We see that the closer the initial volume-ratio is to unity the larger the main vortex is likely to be and hence the larger its self-energy will be. We notice that there is a high degree of variance shown by the error bar for $\rho_V = 1.0$, the size of this error bar is not dependent on the initial vertical offset as a similarly high variance is seen for $\rho_V = 1.0$ for any single value of initial vertical offset.

3.3 Conclusions

In this chapter we have studied the interactions occurring between two co-rotating QG vortices of varying initial height-to-width aspect-ratios, volume-ratios and vertical offsets at the margin of stability. These vortices are of uniform and equal potential vorticity.

We define five types of merger regime as done by *Dritschel & Waugh* (1992)[17] and find three of these occur in our parameter space, namely complete-merger (CM), partial-merger (PM) and partial straining-out (PSO). We see that for initial volume-ratio $\rho_V = 0.2$, interactions are most likely to fall in to the PSO regime - 92% of our 625 cases do. The remaining 8% of cases at $\rho_V = 0.2$ result in PM. The predominant interaction regime for cases $0.4 \leq \rho_V \leq 1.0$ is PM with rare occurrences of CM and PSO. We also show that when vortices do undergo complete-merger, it is mostly likely to occur when they have equal volumes and/or equal height-to-width aspect-ratios. Upon closer inspection, CM turns out to be even rarer than first shown since some cases diagnosed as CM display the onset of re-separation at later times in the evolution. The vertical offset appears to have little influence on the interaction-type between the vortices.

Generally in this parameter space vortex interactions are made up of two distinct phases. The first of these phases is generally merger, in the majority

of cases the vortices join together very early on in the evolution. In the second phase, usually from about 5 characteristic vortex rotations, the vortices begin ejecting filaments regardless of whether the pair remain merged or not.

Despite the large number of filamentary structures ejected in the second phase of the interactions, self-energy is on average transfered to larger scales i.e. it displays an 'inverse-cascade' over time. Intermediate scale vortices whose mean-radii lie in the range $0.25 \leq r \leq 0.4$ generally do not survive the interaction and are destroyed (i.e. broken into filaments or smaller vortices) by the proximity of the larger vortices. We also see that at $t = 60$, the remaining vortices fall into two distinct vortex populations, those with mean-radii between 0.40 and 1.0 and those with mean-radii below 0.25. Virtually no vortices are found between these two populations.

A connection between the initial volume-ratio and the growth of the largest vortex is found such that vortices are likely to grow more when ρ_V is closer to unity. At unity volume-ratio however the degree of variance is so high that a vortex radius can grow anywhere between 4.8% and 17.7%. However, statistically, in a turbulent flow containing an ever-increasing number of vortices with decreasing scale (see *Reinaud et al.* (2003)[39]), interactions between like sized vortices are relatively rare compared to interactions between disparate-sized vortices as found by *Dritschel & Reinaud* (2002)[11].

In this chapter we have used the quasi-geostrophic approximation. This is valid for a vanishing Rossby and Froude numbers and filters gravity-waves from the flow. The next chapter deals with interaction between co-rotating vortices in regimes beyond QG that allow for finite Rossby numbers. This will allow for the spontaneous generation of inertia-gravity waves and for ageostrophic advection to occur. The impact of these effects on the overall flow will be investigated.

Chapter 4

Interactions between two co-rotating non-hydrostatic vortices

4.1 Introduction

In this chapter we investigate the interactions occurring between two initially ellipsoidal vortices at a finite Rossby number (Ro). Using the non-hydrostatic (NH) equations described in section 2.4 and the algorithm described in section 2.5, we perform time evolution simulations on each given initial configuration of vortices.

In section 4.1.1 we describe the initial conditions used in this study. The initial conditions for the PV contours are identical to those used for QG. The algorithm used to solve the NH equations is computationally more expensive than the QG equations, therefore we use a velocity grid of resolution 64^3 for these calculations. We also re-calculate the necessary QG simulations using a velocity grid of resolution 64^3, identical to that used for the NH calculations, so that

comparisons between NH and QG may be made. Snapshots of the flow for the QG case $h_1/r_1 = 0.8$, $h_2/r_2 = 0.8$, $\rho_V = 1.0$ and $\delta z = 0.2$ are shown at grid resolution 64^3 and 128^3 in figure 4.1. As can be seen, there is no qualitative difference between the flows except for very fine-scale filaments in the high resolution case that cannot be resolved at the lower resolution. In the absence also of quantitative differences between the different resolutions we conclude that a velocity grid of 64^3 is still of sufficiently high resolution to study. *Dritschel & Viúdez* (2003)[16] show comparisons between 64^3 and 128^3 grid resolutions for non-hydrostatic cases and demonstrate that the differences between them are negligible.

Section 4.2 presents the results of these calculations, including identification of the interaction regimes and their dependencies on the initial conditions, the effects (if any) of the Rossby number and the generation of inertia-gravity waves during the evolution. We present conclusions on the study in section 4.3.

4.1.1 Initial Conditions

The spatial initial conditions for this study are taken to be exactly the same as for the corresponding cases in QG. That is for given height-to-width aspect-ratios, volume-ratios and vertical offsets we use an identical configuration of the ellipsoids as in QG, with the horizontal separation being also identical. We introduce a new dimension to the parameter space, that is the Rossby number (Ro). The computational cost of modelling the time evolution of these cases with finite Rossby number, however, is much higher than that for QG. To reduce the size of the parameter space, we consider only cases where the vortices have equal height-to-width aspect-ratios, $h/r = h_1/r_1 = h_2/r_2$. This effectively reduces the parameter space by one dimension and since figure 3.7 shows these cases to exhibit a large variety of behaviours we feel this simplification is justified. We perform calculations for three values of h/r, three values of ρ_V and two values of

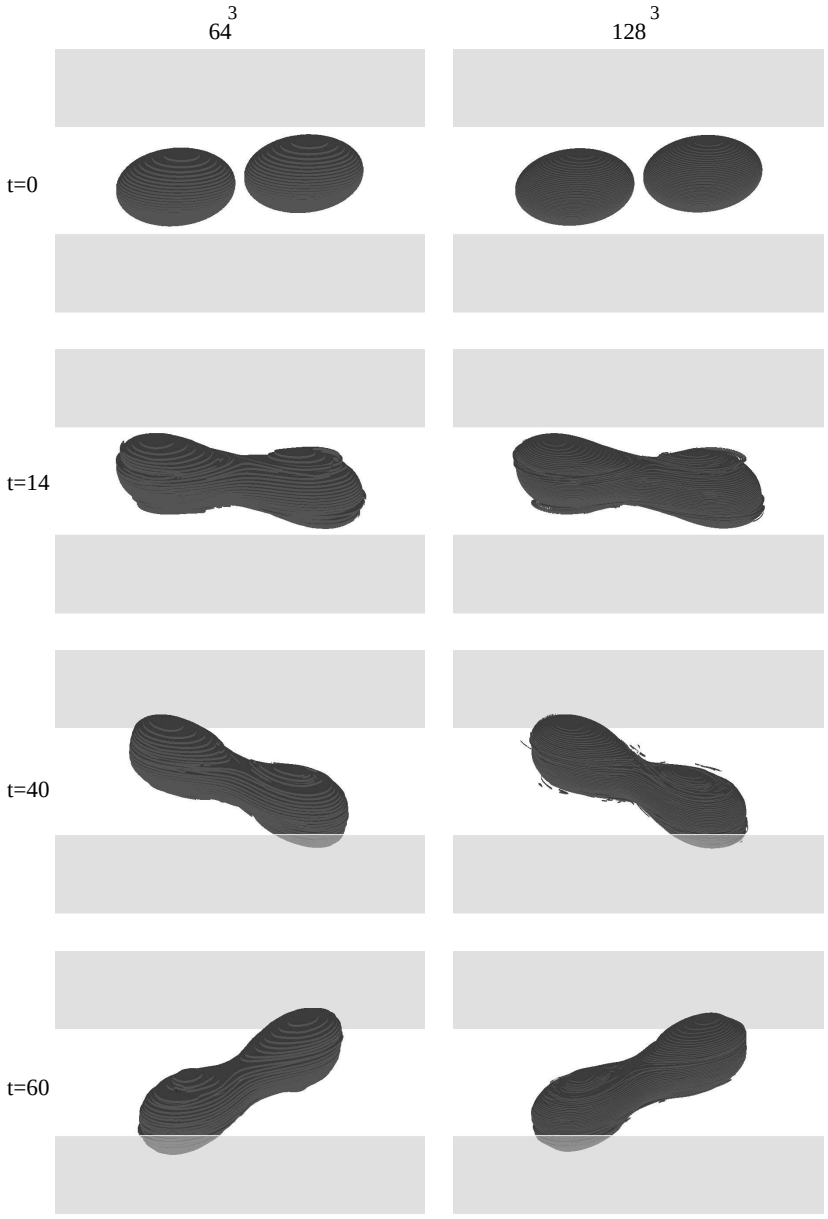

Figure 4.1: Comparison of QG simulations using grid resolutions of 64^3 and 128^3 for the case $h_1/r_1 = 0.8$, $h_2/r_2 = 0.8$, $\rho_V = 1.0$ and $\delta z = 0.2$. View is 60° from the vertical and covers ± 1.5 from the domain centre in the horizontal. Light grey areas show front and back walls of the box which spans the full height of the PV distribution.

Parameter	Minimum	Maximum	Increment
h/r	0.4	1.2	0.4
ρ_V	0.2	1.0	0.4
δz	0.2	0.6	0.4
Ro	-0.5	0.5	0.25*

Table 4.1: Parameter space for simulations at finite Rossby number. $h/r \equiv h_1/r_1 = h_2/r_2$ is the vortex height-to-width aspect-ratio, ρ_V is the volume ratio of the vortices (V_2/V_1), δz is the vertical offset as a fraction of the sum of the half heights and Ro is the Rossby number. Negative Rossby number means an anti-cyclonic case. * Note that we use a QG simulation calculated on a velocity grid resolution of 64^3 to represent cases where $Ro = 0.0$. A total of 72 non-hydrostatic simulations are performed.

δz. We consider 5 values of Ro – two cyclonic and two anti-cyclonic and a fifth, at $Ro = 0.0$, is taken as being QG which we re-calculate on a grid resolution of 64^3 to coincide with the grid resolution to be used for the NH calculations. The parameter space for this investigation is set out in table 4.1.

These calculations are performed over the equivalent of 60 QG time units, the corresponding time for the non-hydrostatic code is given by

$$t_{NH} = \frac{t_{QG}}{(f/N)|Ro|}, \tag{4.1}$$

where f/N is taken as 0.1, this being typical for an oceanic case. The velocity field grid resolution is taken as 64^3 and the fine-to-coarse grid-ratio is taken as 4:1. The time step is taken as 0.1 this being $\Delta t_{QG}/(f/N)|Ro|$ at $|Ro| = 0.5$ and $0.5\Delta t_{QG}/(f/N)|Ro|$ at $|Ro| = 0.25$.

4.1.2 Diagnosing balance

To distinguish between the balanced part of the flow and the imbalanced part of the flow we use two different methods. The first of these is NQG (nonlinear QG), developed by *McKiver & Dritschel* (2006)[31]. This method is based on a quasi-geostrophic scaling of the non-hydrostatic equations to directly recover the balanced part of the flow to second order Rossby number. The second of these is OPV (optimal PV) developed by Viúdez & Dritschel (2004)[45]. The OPV balanced field is obtained by backwards and forwards time integrations to arrive at the desired configuration of PV. The IGW's are removed and the PV restored at each loop of the integration.

4.2 Results

4.2.1 Interaction regimes

As with the QG calculations in section 3.2.1, we first investigate the types of interaction arising from the vortex evolution under the NH equations. We use the same criteria as we did to identify the interaction regimes in the QG cases, that is the criteria adapted from *Dritschel & Waugh* (1992)[17], (see §3.2.1 for details). We show the interaction types arising from the NH calculations and the corresponding lower resolution QG cases in figure 4.2.

It is interesting to see that, unlike for the QG cases shown in figure 3.7, the interaction regimes for finite Rossby number cases display a dependence on the vertical offset as well as on the volume ratio. For a small vertical offset, PM is the dominant regime and PSO generally only occurs when there is a large difference between the vortex volumes. For a larger vertical offset however PSO is more prevalent and mostly PM only occurs for equal volume vortices. For non-equal

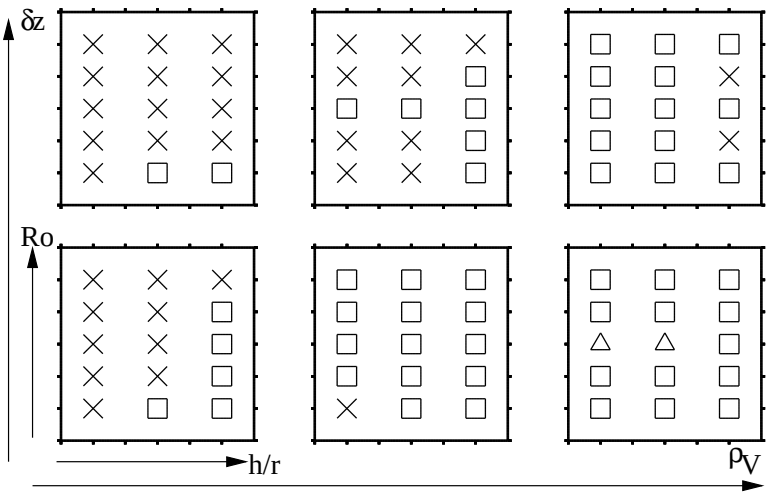

Figure 4.2: Merger regimes over entire parameter space for non-hydrostatic simulations. Plots across the horizontal correspond to $\rho_V = 0.2, 0.6$ & 1.0 starting on the left hand side and plots in the vertical correspond to $\delta z = 0.2$ and 0.6 starting at the bottom. Each plot has h/r on its horizontal axis between 0.2 and 1.4 and has Ro from -0.75 to 0.75 in the vertical. $\times$ represents partial straining-out, $\square$ represents partial merger and $\triangle$ represents complete-merger.

volume vortices, PM generally only occurs when both vortices are slightly prolate i.e. $h/r = 1.2$.

Figure 4.2 does not indicate any strong dependence of interaction type upon the Rossby number. One of the few exceptions to this is the case of $h/r = 1.2$, $\rho_V = 1.0$ and $\delta z = 0.6$ where for $Ro = 0.25$ we see a PSO regime and for $Ro = 0.5$ we see a PM regime emerge. To gain a qualitative view of these two cases we show the flow diagrams in figure 4.3

We see that these cases are qualitatively very similar. The major difference between them is that the vortices in the $Ro = 0.25$ case do not come as close to one another as they do for the $Ro = 0.5$ case so undergo PSO rather than PM. The reason the vortices do not come as close for $Ro = 0.25$ as they do for $Ro = 0.5$ is likely to be due to the 'bunching' of the vortex lines (see figure 4.6 in section 4.2.2). At $Ro = 0.5$ the rotation of the vortices will be stronger, that is the density of the vortex lines within the vortex will be higher and also the isopycnals will be pulled closer together inside the vortices. These two effects will make the vortices more stable for the higher Rossby number, allowing the smaller vortex to deform sufficiently to approach closer to the larger vortex.

We now investigate closely two simulations, one resulting in PSO and the other resulting in PM. Figure 4.4 shows the case $h/r = 1.2$, $\rho_V = 0.2$, $\delta z = 0.6$ and $Ro = -0.25$ at QG times 0, 14, 40 and 60. This case displays a partial straining-out of the smaller vortex by the larger vortex. The larger vortex causes a filament of PV to be strained-out from the smaller vortex. This filament begins to become detached from the smaller vortex at QG time 7. By the end of the simulation ($t_{QG} = 60$), the smaller vortex has been reduced to 81% its original volume while the larger vortex has not changed in volume throughout the entire evolution.

Figure 4.5 shows the case $h/r = 1.2$, $\rho_V = 0.2$, $\delta z = 0.2$ and $Ro = -0.25$ which

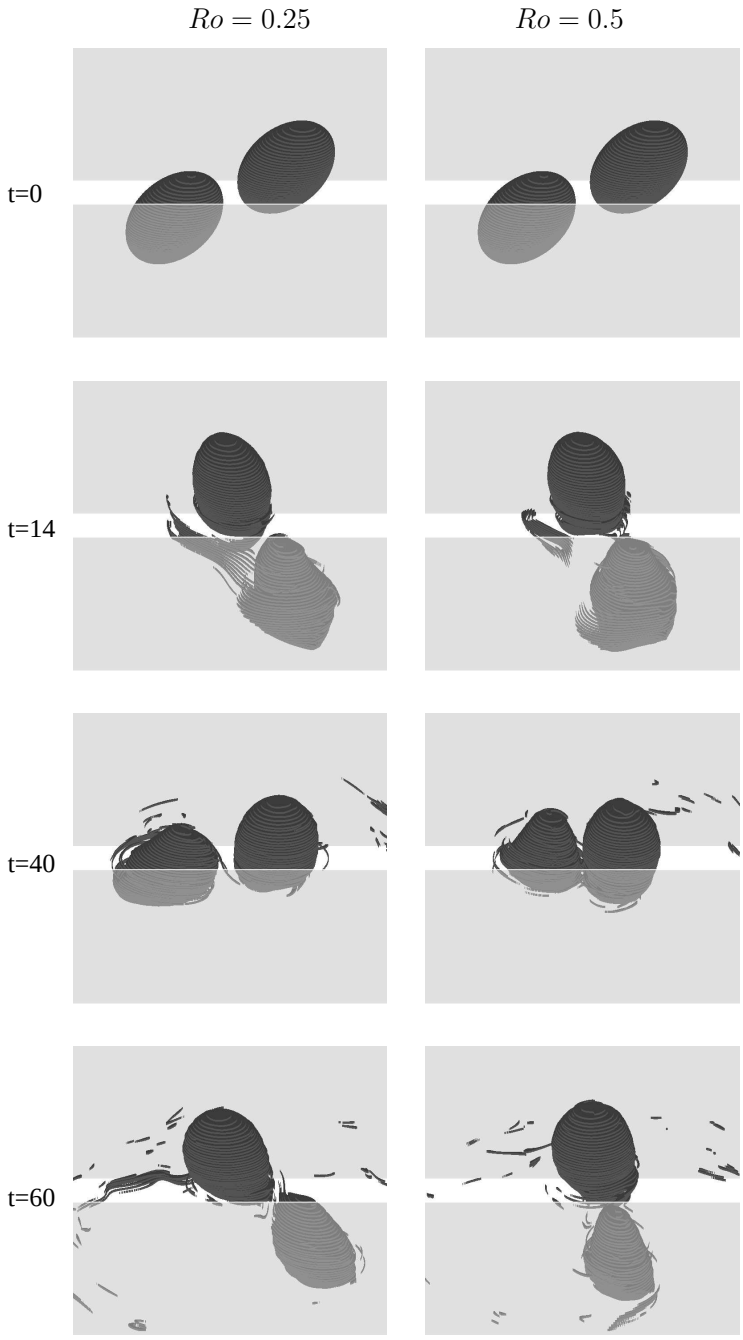

Figure 4.3: Comparison of cases for $h/r = 1.2$, $\rho_V = 1.0$, $\delta z = 0.6$ at Rossby numbers $Ro = 0.25$ and $Ro = 0.5$. Views are at 60° from the vertical covering ± 1.5 from the domain centre in the horizontal. Light grey areas show front and back walls of the box which spans the full height of the PV distribution.

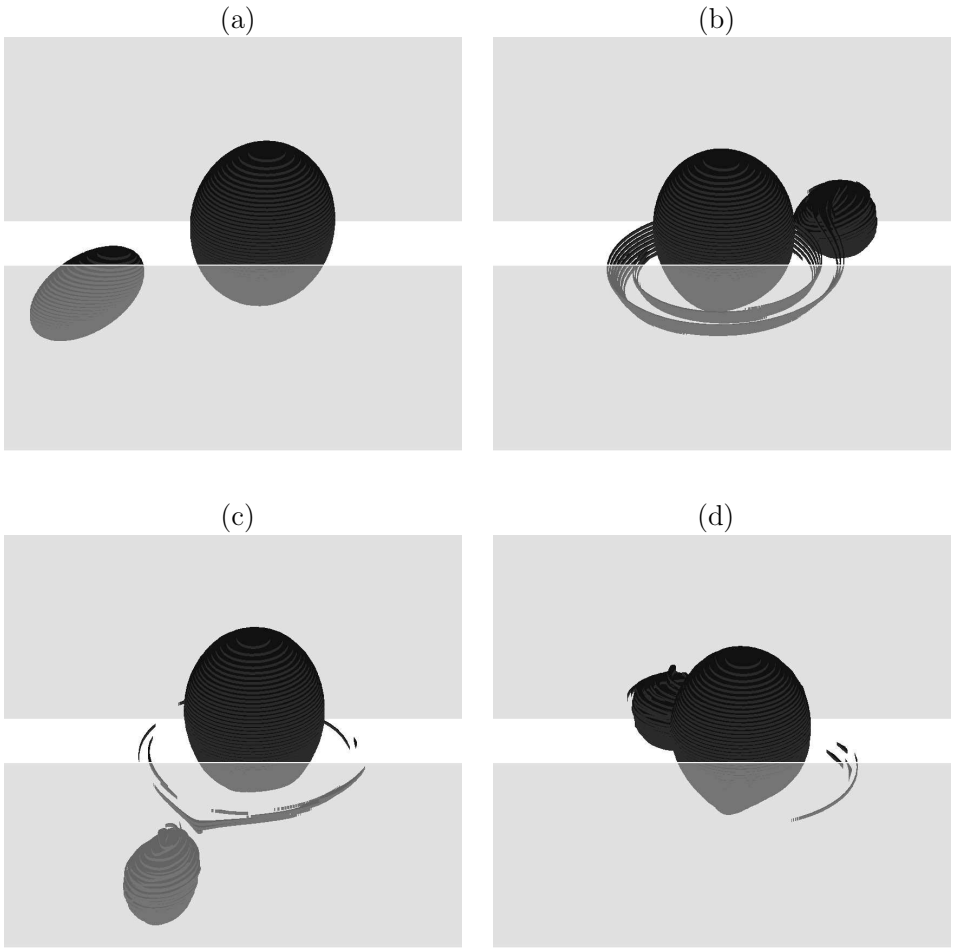

Figure 4.4: Figure showing a non-hydrostatic vortex interaction resulting in a partial straining-out regime. Initial conditions are $h/r = 1.2$, $\rho_V = 0.2$, $\delta z = 0.6$ and $Ro = -0.25$. View is 60° from the vertical and covers ± 1.5 from the domain centre in the horizontal. Light grey areas show front and back walls of the box which spans the full height of the PV distribution. Times shown are QG times (a) $t = 0$, (b) $t = 14$, (c) $= 40$ and (d) $t = 60$.

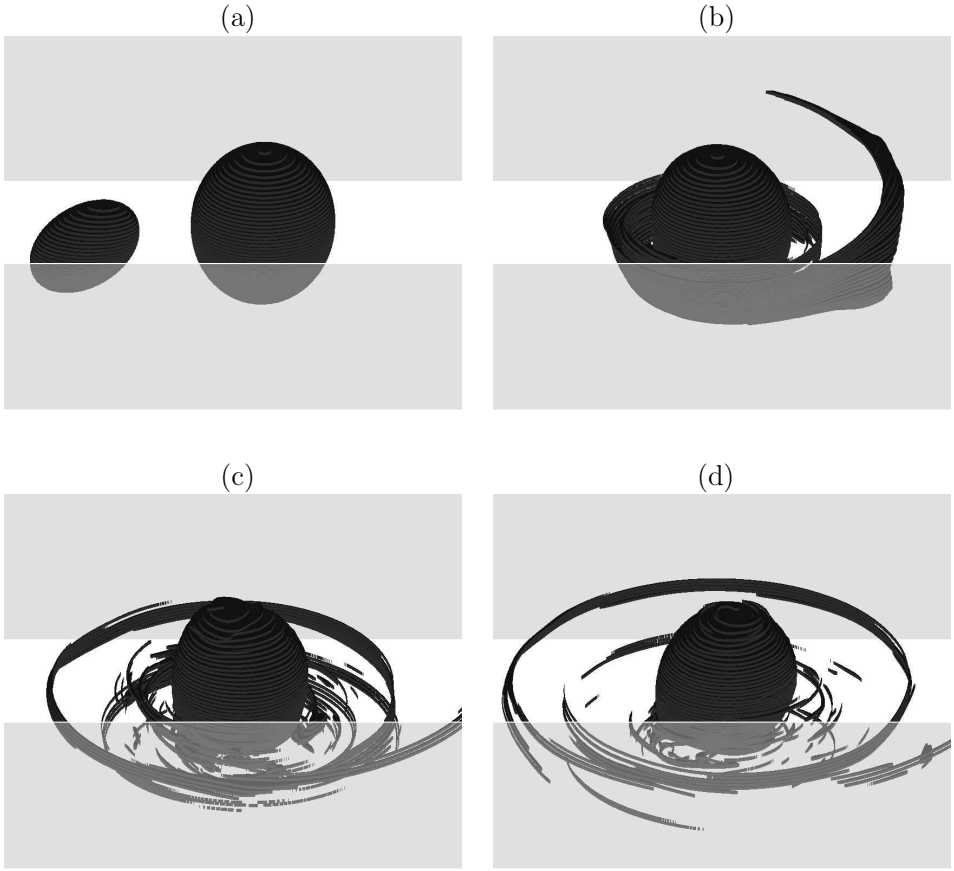

Figure 4.5: Figure showing a non-hydrostatic vortex interaction resulting in a partial merger regime. Initial conditions are $h/r = 1.2$, $\rho_V = 0.2$, $\delta z = 0.2$ and $Ro = -0.25$. View is 60° from the vertical and covers ± 1.5 from the domain centre in the horizontal. Light grey areas show front and back walls of the box which spans the full height of the PV distribution. Times shown are QG times (a) $t = 0$, (b) $t = 14$, (c) $= 40$ and (d) $t = 60$.

results in partial merger. Qualitatively one could expect this case to be classified as either complete straining-out or complete merger. However, as happened with the QG case in figure 3.10, a sufficient volume of the PV exists as filaments and small vortices at the end of the evolution to classify this as PM. Over the first 11 QG time periods, both vortices maintain a steady volume. The larger vortex remains approximately ellipsoidal while the smaller vortex is strained-out. At QG time 12 the smaller vortex begins to disintegrate into smaller structures. The larger vortex begins to absorb these structures at QG time 24 and over over the next two time units grows to 115% of its original volume. Then at QG time 26 the large vortex ejects a smaller structure and returns again to its original volume with the sum of the volumes of the two main vortices now being 95% of the total volume at the beginning of the simulation, the rest of the PV existing now in filaments and other small scale vortices. By the end of the simulation ($t_{QG} = 60$), the main vortex has reduced to 94% of its original size due to the ejection of filaments. Why then is this interaction not classified as complete straining-out? The reason is that, although apart from very small scale material there is only one main vortex which has not dramatically altered its volume, there are structures in the debris that still have sufficient volume to be classed as the second main vortex under the tolerance we specify. Again we see, as before in figure 3.10 that although the technique used to determine merger regimes is quantitatively accurate, there are discrepancies between the regimes calculated and how one may qualitatively classify interactions.

4.2.2 Effects of the Rossby number on interaction behaviour

In this section we investigate the effects that different Rossby numbers have in determining the behaviour of the flow evolution. In particular we wish to see

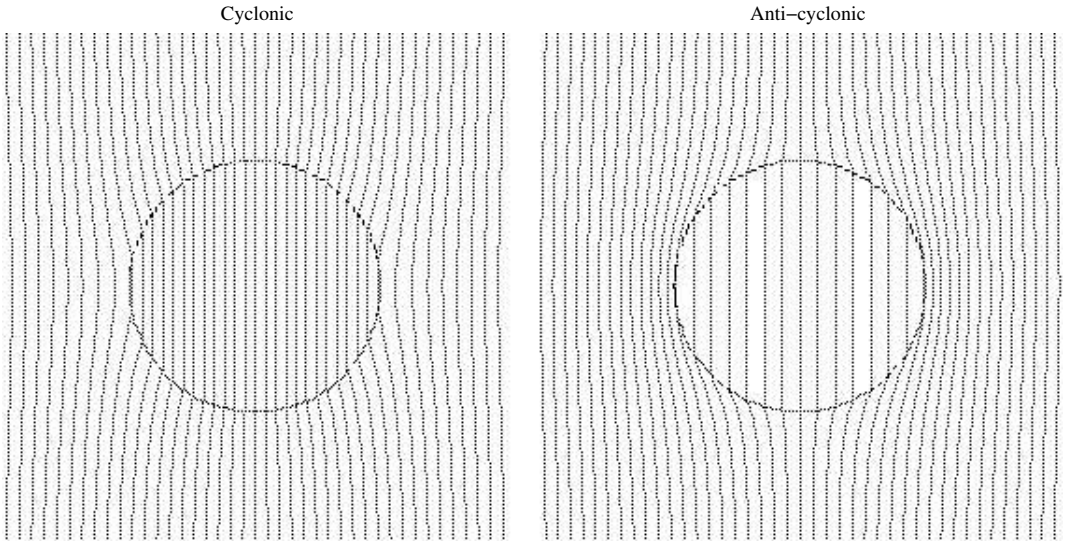

Figure 4.6: Vortex lines in and around a spherical cyclonic ($Ro = +0.5$) vortex and a spherical anti-cyclonic ($Ro = -0.5$) vortex. Figure shown in $x - z$ plane. Used here courtesy of David Dritschel.

what effects having opposite signed Rossby numbers, that is cyclonic and anti-cyclonic regimes, have. Figure 4.6 shows the behaviour of the vortex lines in and around cyclonic and anti-cyclonic vortices. In cyclonic vortices the vortex lines become 'bunched' tighter together, making them more robust to rotational instabilities, whereas they are spread apart in an anti-cyclonic vortex. This effect similarly occurs horizontally to the isopycnals in and around the vortices, making cyclonic vortices more robust to baroclinic instabilities.

Figure 4.7 shows the comparison between $Ro = 0.5$, $Ro = -0.5$ and a QG case for $h/r = 1.2$, $\rho_V = 1.0$ and $\delta z = 0.2$ for five different times. We see that the cyclonic case ($Ro = 0.5$) does not begin ejecting filaments as early as the anti-cyclonic case or indeed the QG case. In the case shown here in figure 4.7 more PV is seen to be ejected as filaments during the course of the evolution than was seen for the QG case. In the QG case, the main vortex at the end of the evolution was 81% of its initial volume whereas for $Ro = 0.5$ the main vortex

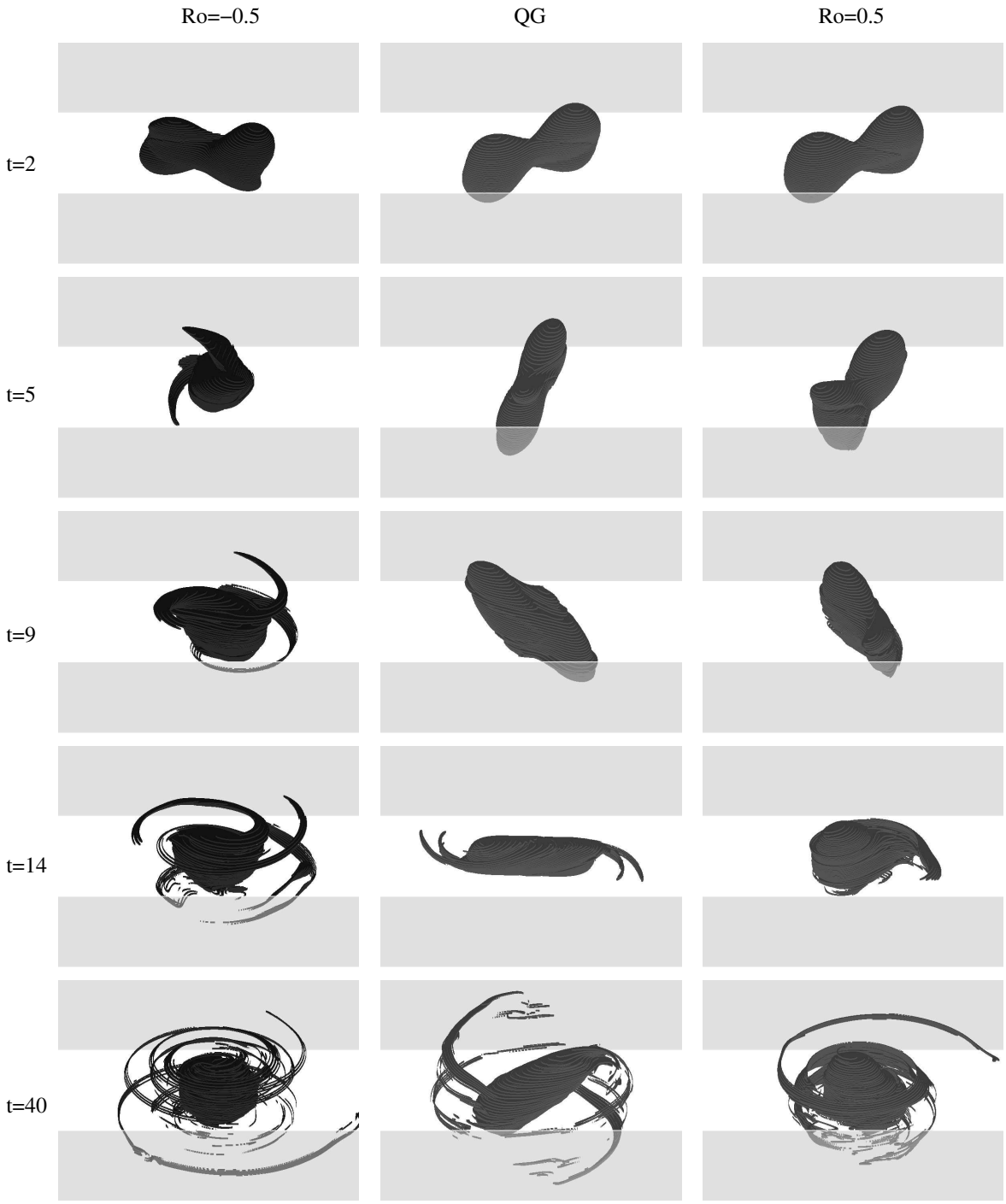

Figure 4.7: Comparison of QG, cyclonic and anti-cyclonic cases for $h/r = 1.2$, $\rho_V = 1.0$, $\delta z = 0.2$. Non-hydrostatic cases are at Rossby numbers $Ro = 0.5$ and $Ro = -0.5$. Views are at 60° from the vertical covering ± 2.0 from the domain centre in the horizontal. Light grey areas show front and back walls of the box which spans the full height of the PV distribution.

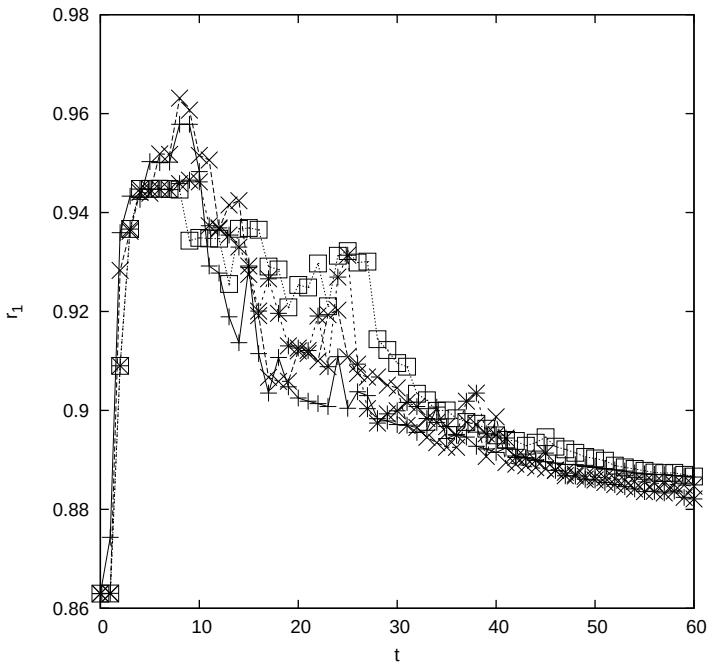

Figure 4.8: Evolution of the size of the largest vortex averaged over h/r, ρ_V and δz for $Ro = -0.5$ $(+)$, $Ro = -0.25$ $(\times)$, $Ro = 0.25$ $(*)$ and $Ro = 0.5$ $(\Box)$.

at the same time is 75% of its initial volume and for $Ro = -0.5$ the main vortex at this final time is 71% of its initial volume.

Figure 4.8 shows the evolution of the largest vortex against time for each Rossby numbers averaged over all h/r, ρ_V and δz. We see that in each case, the peak radius occurs around $t_{QG} = 9$, being around 2 vortex rotations earlier than was seen in QG. Again we see the size of the largest vortex decrease with time after this initial peak indicating the re-separation of vortices and the ejection of filaments. We note that the average size of the largest vortex in cyclonic cases does not decrease as rapidly as anti-cyclonic cases. This again can be attributed to the behaviour of the vortex lines and isopycnals described above, see figure 4.6.

Figures 4.9 and 4.10 show comparisons between flows at each chosen Rossby number (and QG) at various time intervals during the first third of the total

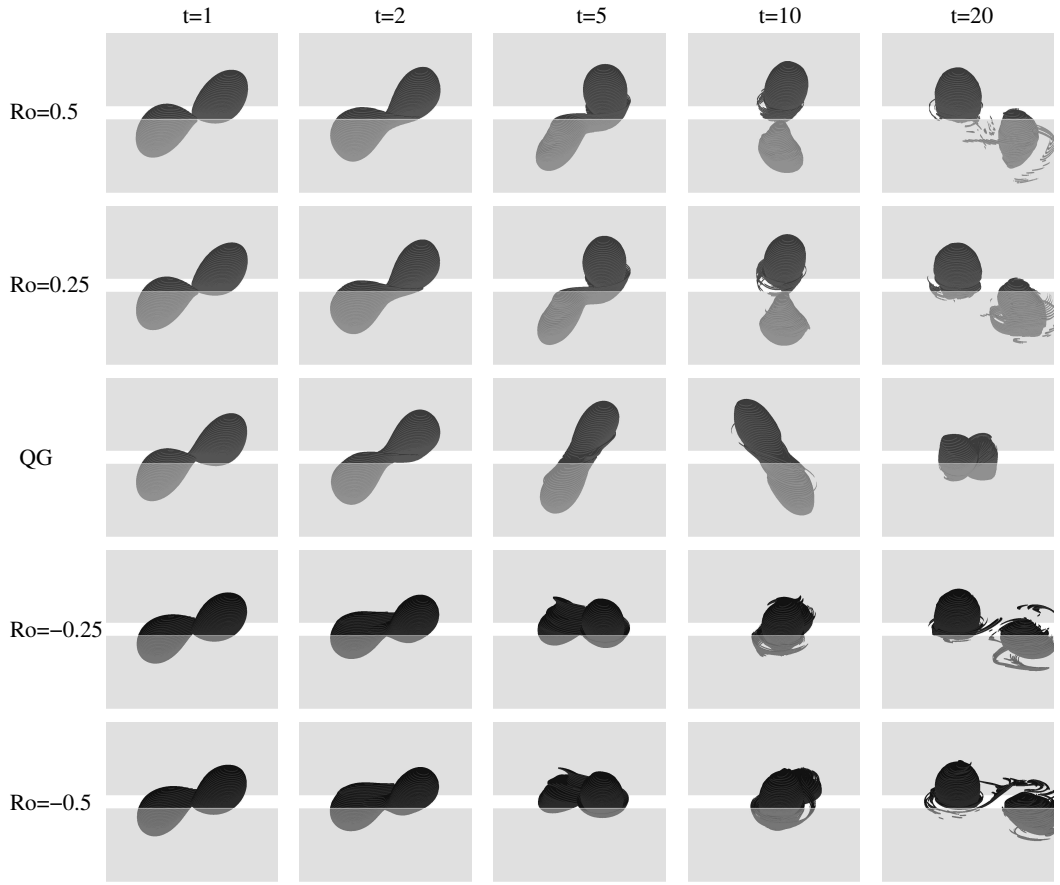

Figure 4.9: Flow diagrams of the NH cases $h/r = 1.2$, $\rho_V = 1.0$, $\delta z = 0.6$ at Rossby numbers $Ro = 0.5$, $Ro = 0.25$, QG, $Ro = -0.25$ and $Ro = -0.5$, at times $t_{QG} = 1, 2, 5, 10$ & 20. Span of the horizontal region shown is ± 1.5 from the domain centre. Views are 60° from the vertical. Light grey areas show front and back walls of the box which spans the full height of the PV distribution.

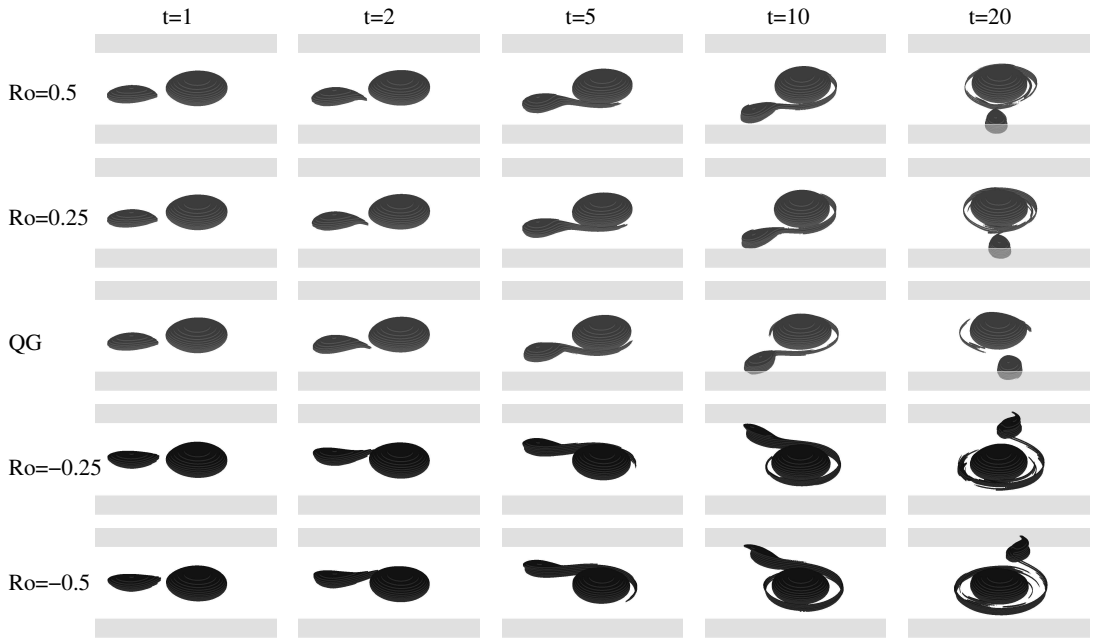

Figure 4.10: Flow diagrams of the NH cases $h/r = 0.4$, $\rho_V = 0.2$, $\delta z = 0.2$ at Rossby numbers $Ro = 0.5$, $Ro = 0.25$, QG, $Ro = -0.25$ and $Ro = -0.5$, at times $t_{QG} = 1, 2, 5, 10$ & 20. Span of the horizontal region shown is ± 1.5 from the domain centre. Views are 60° from the vertical. Light grey areas show front and back walls of the box which spans the full height of the PV distribution.

time evolution. It is noticeable that the interactions in both of these cases are remarkably similar. The most noticeable difference between the Rossby numbers shown in these figures can be seen at $t_{QG} = 20$ where anti-cyclonic, that is negative Rossby number, cases show a marginally larger amount of filamentary debris. This is again likely to be due to the weakened rotation and stratification described above (see figure 4.6).

4.2.3 Imbalance

We now turn our attention to the imbalanced part of the flow i.e. that part of the flow that is characterised by wave motions. In figure 4.11 we plot the r.m.s. percentage of the vertical velocity that is imbalanced i.e.

$$\%w_{imb} = 100\frac{||w_{imb}||_{rms}}{||w||_{rms}}, \tag{4.2}$$

averaged over all h/r, ρ_V and δz for each Rossby number as calculated by NQG.

We see a generally similar trend to the amount of imbalance for all Rossby numbers except in the strongly anti-cyclonic case $Ro = -0.5$ where approximately 10% more of the vertical velocity is given over to the imbalanced part of the flow. With the rotation and stratification weakened within the strongly anti-cyclonic vortices (see figure 4.6) it is reasonable to expect a greater degree of imbalance to be generated here. It is also interesting to note that all Rossby numbers have the trend that the percentage of imbalanced vertical velocity increases over approximately the first 15 QG times steps and is then seen to more or less level out with variations in the amount of imbalance being around $\pm 2.5\%$. The first 14–15 QG time units, as we have seen previously, correspond to the times when the initial vortices are usually merged together in the first part of the interaction process, it is not surprising that this is when a large amount of the imbalance is generated.

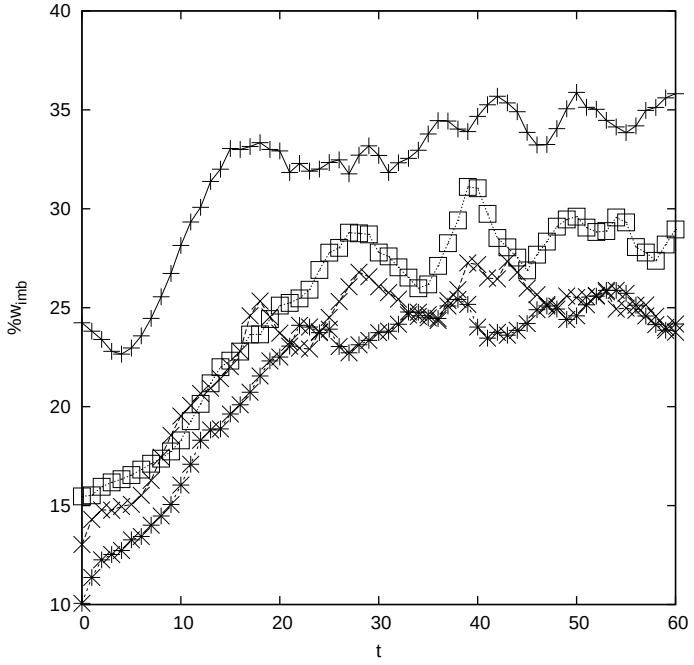

Figure 4.11: R.m.s. percentage of vertical velocity that is imbalanced ($\%w_{imb}$) averaged over all h/r, ρ_V and δz for $Ro = -0.5$ ($+$), $Ro = -0.25$ ($\times$), $Ro = 0.25$ ($*$) and $Ro = 0.5$ ($\Box$) plotted against time (t). Time given in QG time units

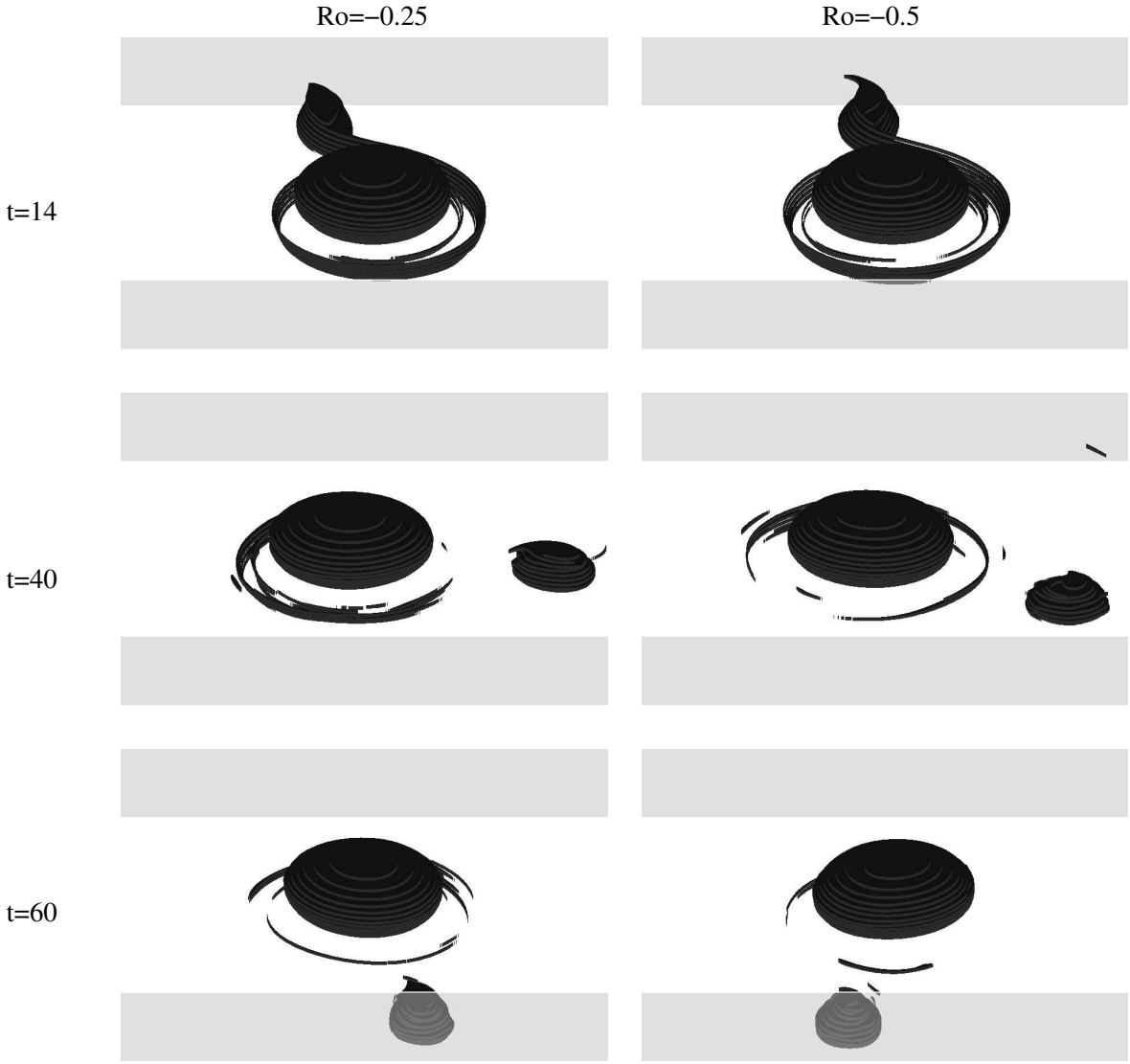

Figure 4.12: Flow diagrams of the NH cases $h/r = 0.4$, $\rho_V = 0.2$, $\delta z = 0.6$ at Rossby numbers $Ro = -0.25$ and $Ro = -0.5$ at times $t_{QG} = 14, 40$ & 60. Span of the horizontal region shown is ± 1.5 from the domain centre. Views are 60° from the vertical. Light grey areas show front and back walls of the box which spans the full height of the PV distribution.

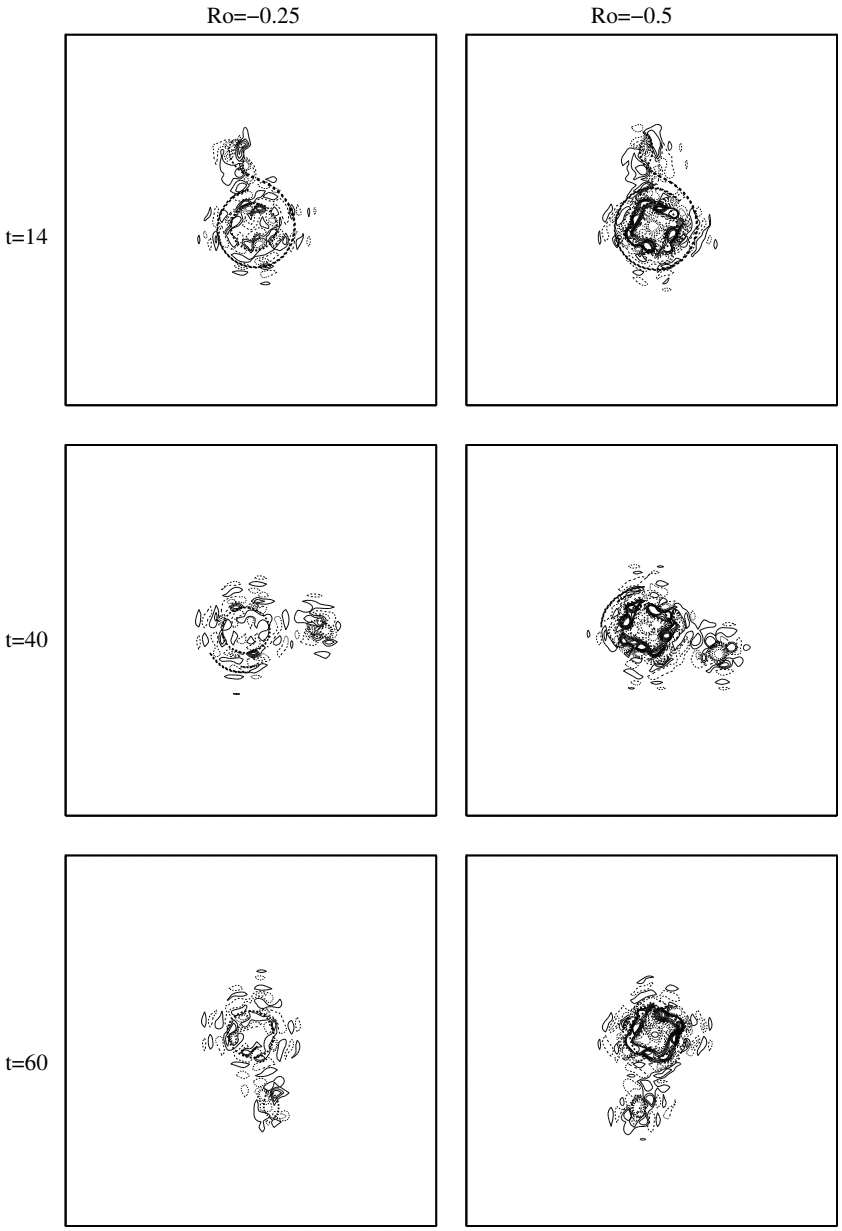

Figure 4.13: Horizontal slices showing contours of w_{imb} for cases $h/r = 0.4$, $\rho_V = 0.2$, $\delta z = 0.6$ at Rossby numbers $Ro = -0.25$ and $Ro = -0.5$ at times $t_{QG} = 14, 40$ & 60. Contour intervals are $\Delta = 2 \times 10^{-6}$ at $Ro = -0.25$ and $\Delta = 10^{-5}$ at $Ro = -0.5$. Slices are in the $x - y$ plane at constant $z = -\pi/32$ and span the full horizontal domain, i.e. $\pm\pi$ from the domain centre. Solid lines show positive values and broken lines show negative values. Dashed bold contours show the PV contours for this layer.

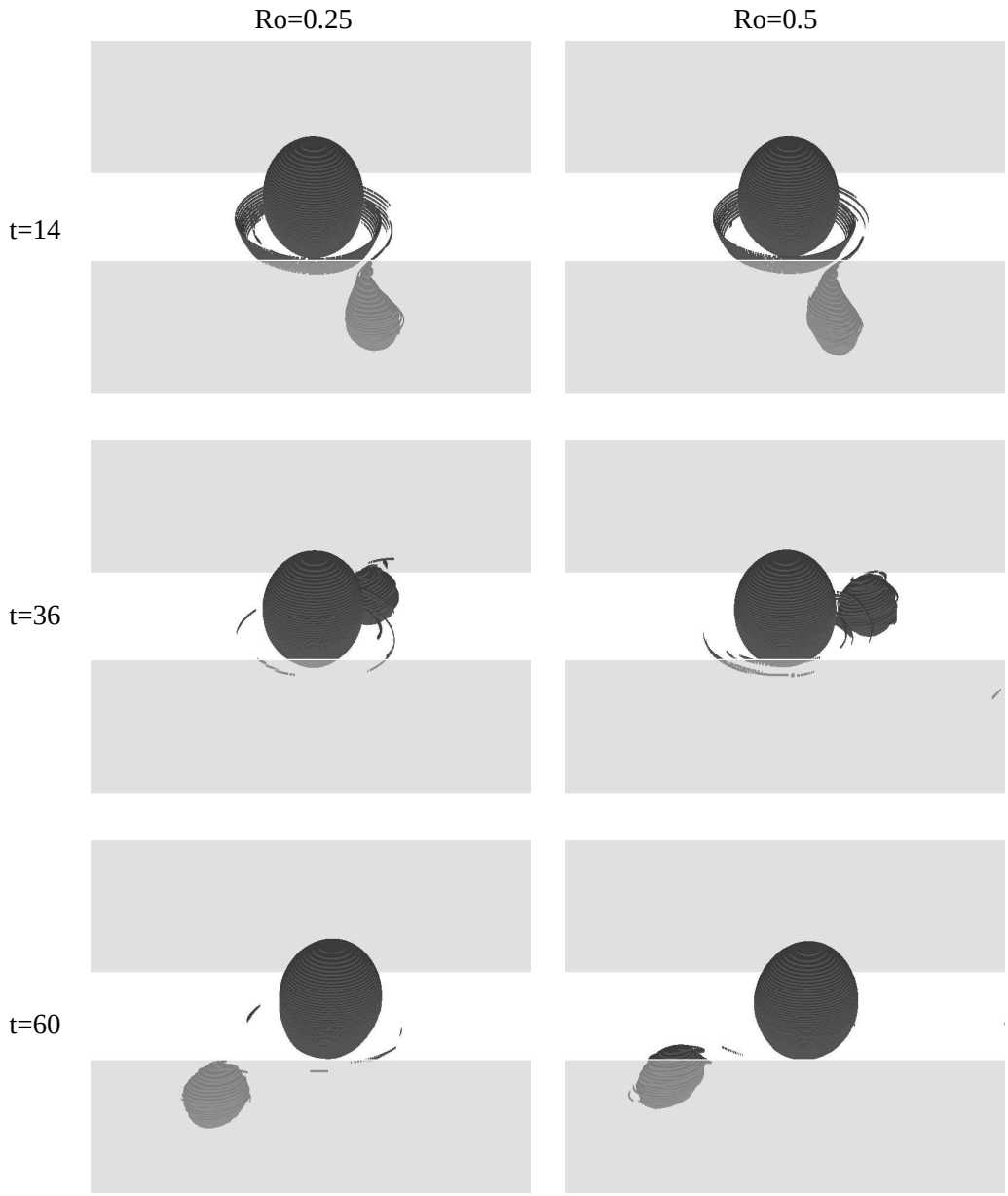

Figure 4.14: Flow diagrams of the NH cases $h/r = 1.2$, $\rho_V = 0.2$, $\delta z = 0.6$ at Rossby numbers $Ro = 0.25$ and $Ro = 0.5$ at times $t_{QG} = 14, 35$ & 60. Span of the horizontal region shown is ± 1.5 from the domain centre. Views are 60° from the vertical. Light grey areas show front and back walls of the box which spans the full height of the PV distribution.

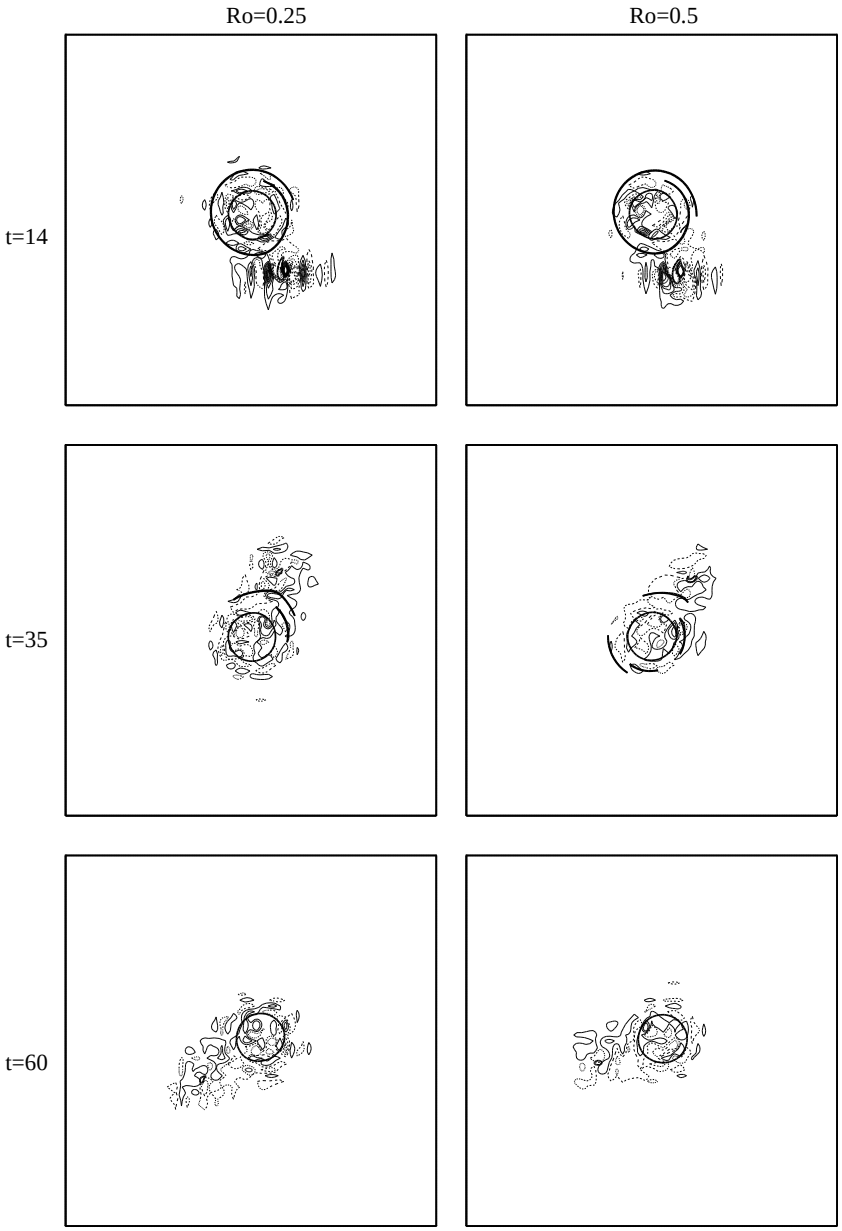

Figure 4.15: Horizontal slices showing contours of w_{imb} for cases $h/r = 1.2$, $\rho_V = 0.2$, $\delta z = 0.6$ at Rossby numbers $Ro = 0.25$ and $Ro = 0.5$ at times $t_{QG} = 14, 35$ & 60. Contour intervals are $\Delta = 2 \times 10^{-6}$ at $Ro = 0.25$ and $\Delta = 10^{-5}$ at $Ro = 0.5$. Slices are in the $x - y$ plane at constant $z = -\pi/16$ and span the full horizontal domain, i.e. $\pm\pi$ from the domain centre. Solid lines show positive values and broken lines show negative values. Bold contours show the PV contours for this layer.

We now present examples of the simulations to compare the nature of the full flow to the imbalanced flow. In figure 4.12 we plot an orthographic view of the full flow of the cases $h/r = 0.4$, $\rho_V = 0.2$, $\delta z = 0.6$ for Rossby numbers $Ro = -0.25, -0.5$. The flow is plotted at QG times $t_{QG} = 14, 40$ & 60. For comparison, we plot contours of the imbalanced part of the vertical velocity, w_{imb} in the $x-y$ plane at constant $z = 0$ for the same cases in figure 4.13. We similarly show the case $h/r = 1.2$, $\rho_V = 0.2$, $\delta z = 0.6$ for Rossby numbers $Ro = 0.25, 0.5$ which also evolves in a PSO regime, in figures 4.14 and 4.15 at times $t_{QG} = 14, 35$ & 60.

We see that the vortices in each case undergo a standard PSO type interaction for both Rossby numbers. Part of the smaller vortex is strained-out by the larger vortex but does not merge with it, thus the smaller vortex decreases in volume whilst the larger vortex maintains a constant volume. In the imbalanced part of the flow plotted in figures 4.13 and 4.14, we see definite wave-like structures propagating from both vortices. In this plane these waves generally appear to propagate in a direction parallel to the horizontal radial axis of the vortex. In the case of the smaller, orbiting vortex, these waves are most prominent in a direction parallel to the orbital direction of the vortex. We see that the amplitude of the waves is higher for larger values of $|Ro|$.

In figures 4.16 and 4.18 we show a three-dimensional view of the full flow for two PM interactions with the corresponding contours of w_{imb} in the $x - y$ plane at constant $z = 0$ in figures 4.17 and 4.18. Figures 4.16 and 4.17 are for the cases $h/r = 0.8$, $\rho_V = 0.6$, $\delta z = 0.2$ and $Ro = 0.25, 0.5$ and figures 4.18 and 4.19 are for the cases $h/r = 0.8$, $\rho_V = 1.0$, $\delta z = 0.2$ and $Ro = -0.25, -0.5$.

In figures 4.17 and 4.19 we see a large amount of imbalance occurring in the regions where the smaller vortex is being destroyed. Again we see here that the imbalanced part of the vertical velocity is larger for higher values of $|Ro|$. In these cases, it appears that imbalance is more prevalent at earlier times than later in

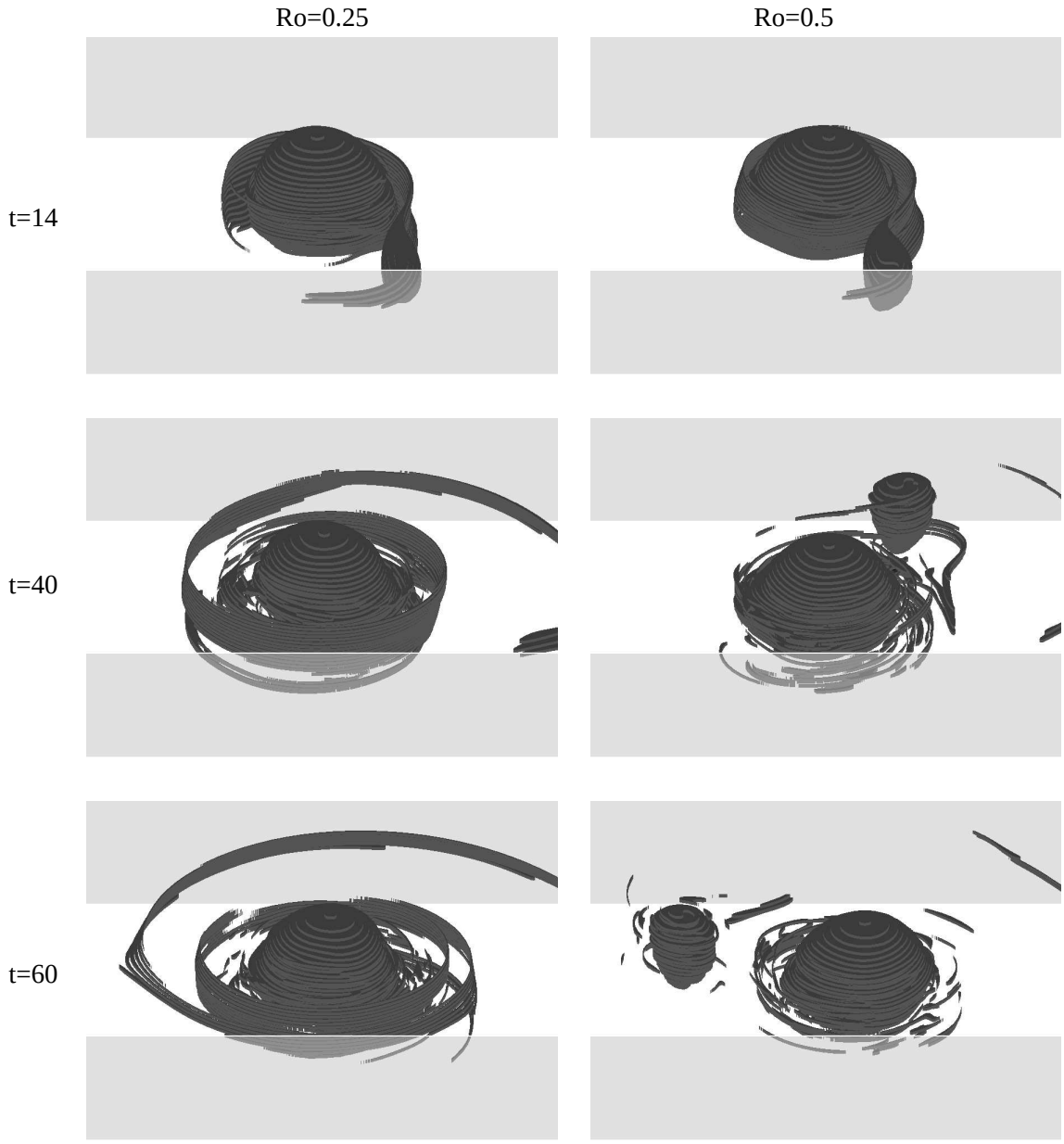

Figure 4.16: Flow diagrams of the NH cases $h/r = 0.8$, $\rho_V = 0.6$, $\delta z = 0.2$ at Rossby numbers $Ro = 0.25$ and $Ro = 0.5$ at times $t_{QG} = 14, 40$ & 60. Span of the horizontal region shown is ± 1.5 from the domain centre. Views are 60° from the vertical. Light grey areas show front and back walls of the box which spans the full height of the PV distribution.

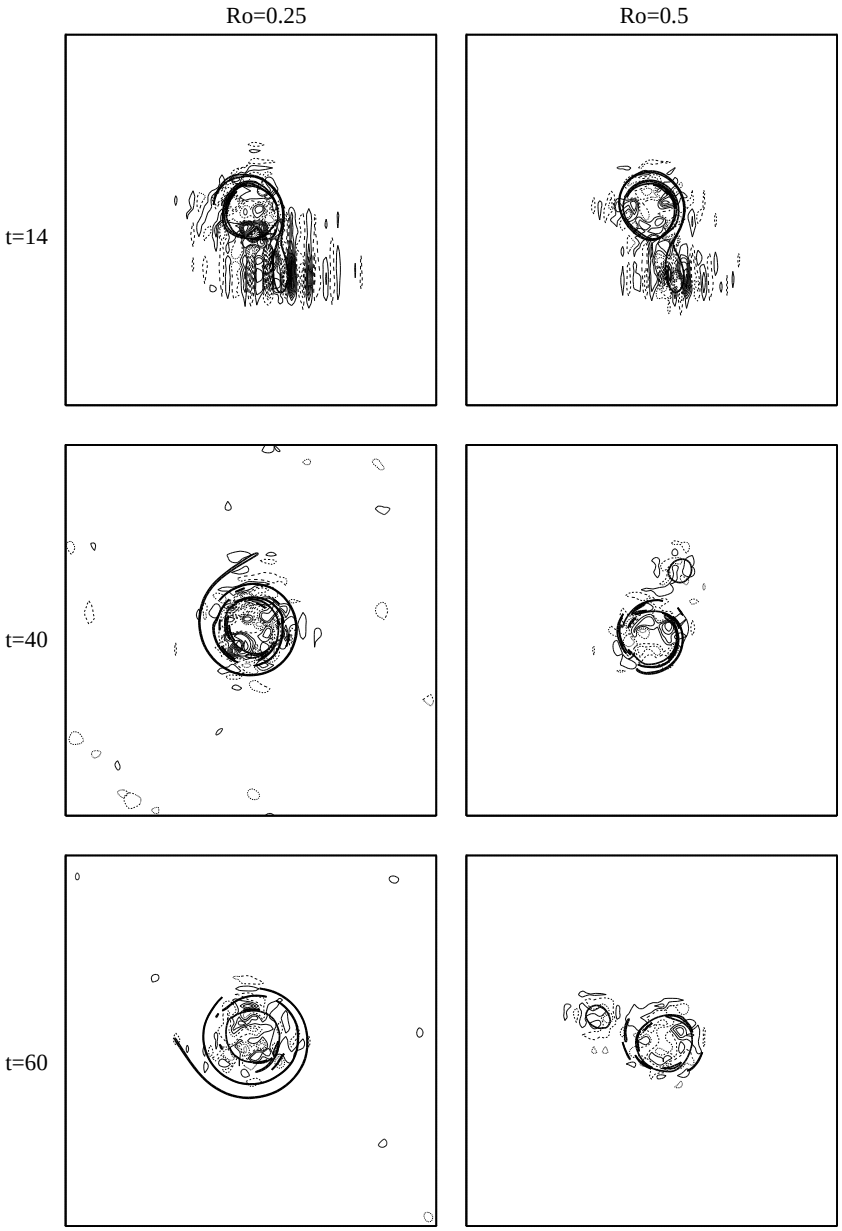

Figure 4.17: Horizontal slices showing contours of w_{imb} for cases $h/r = 0.8$, $\rho_V = 0.6$, $\delta z = 0.2$ at Rossby numbers $Ro = 0.25$ and $Ro = 0.5$ at times $t_{QG} = 14, 40$ & 60. Contour intervals are $\Delta = 2 \times 10^{-6}$ at $Ro = 0.25$ and $\Delta = 10^{-5}$ at $Ro = 0.5$. Slices are in the $x - y$ plane at constant $z = 0$ and span the full horizontal domain, i.e. $\pm\pi$ from the domain centre. Solid lines show positive values and broken lines show negative values. Bold contours show the PV contours for this layer.

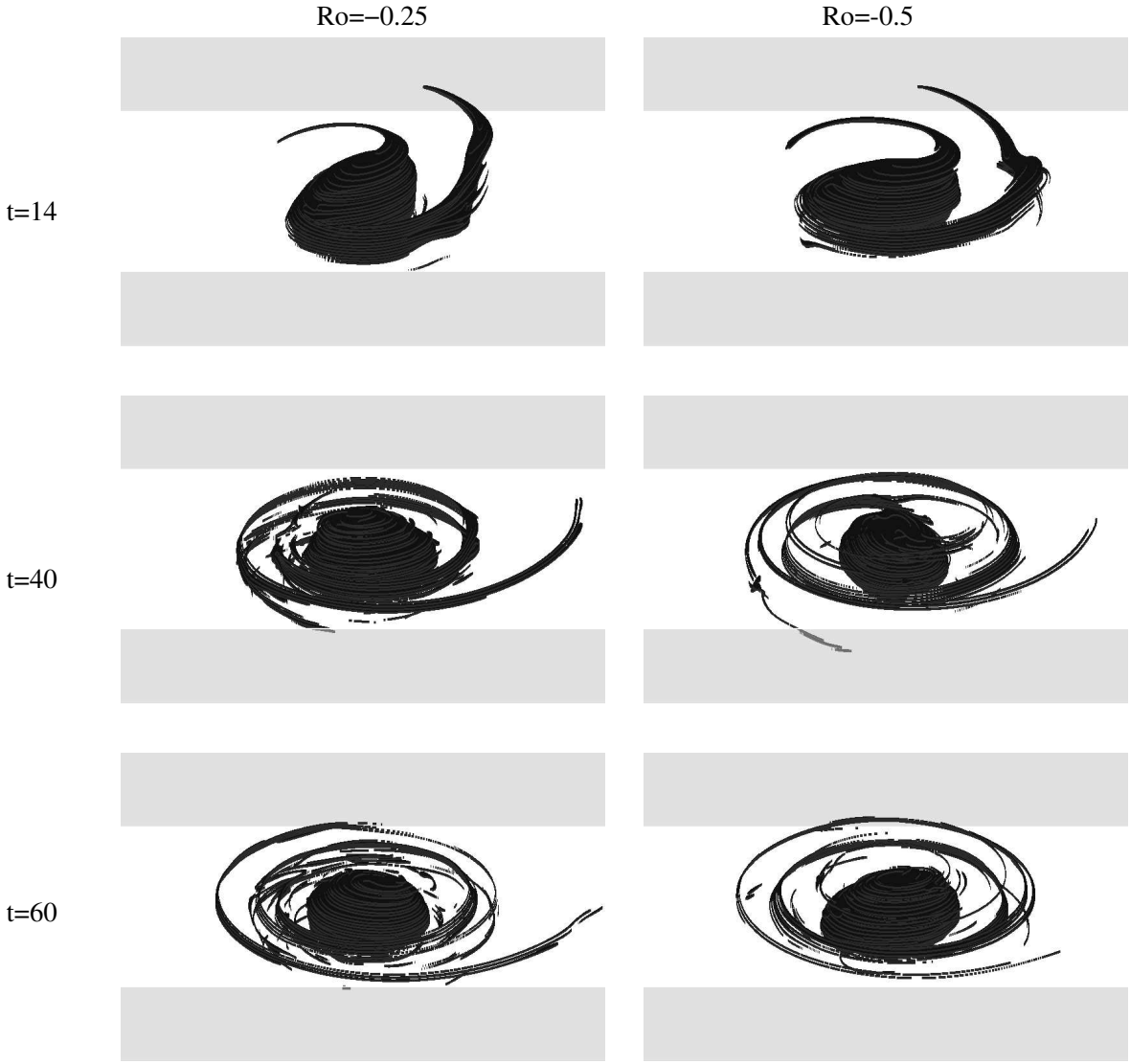

Figure 4.18: Flow diagrams of the NH cases $h/r = 0.8$, $\rho_V = 1.0$, $\delta z = 0.2$ at Rossby numbers $Ro = 0.25$ and $Ro = 0.5$ at times $t_{QG} = 14, 40$ & 60. Span of the horizontal region shown is ± 1.5 from the domain centre. Views are 60° from the vertical. Light grey areas show front and back walls of the box which spans the full height of the PV distribution.

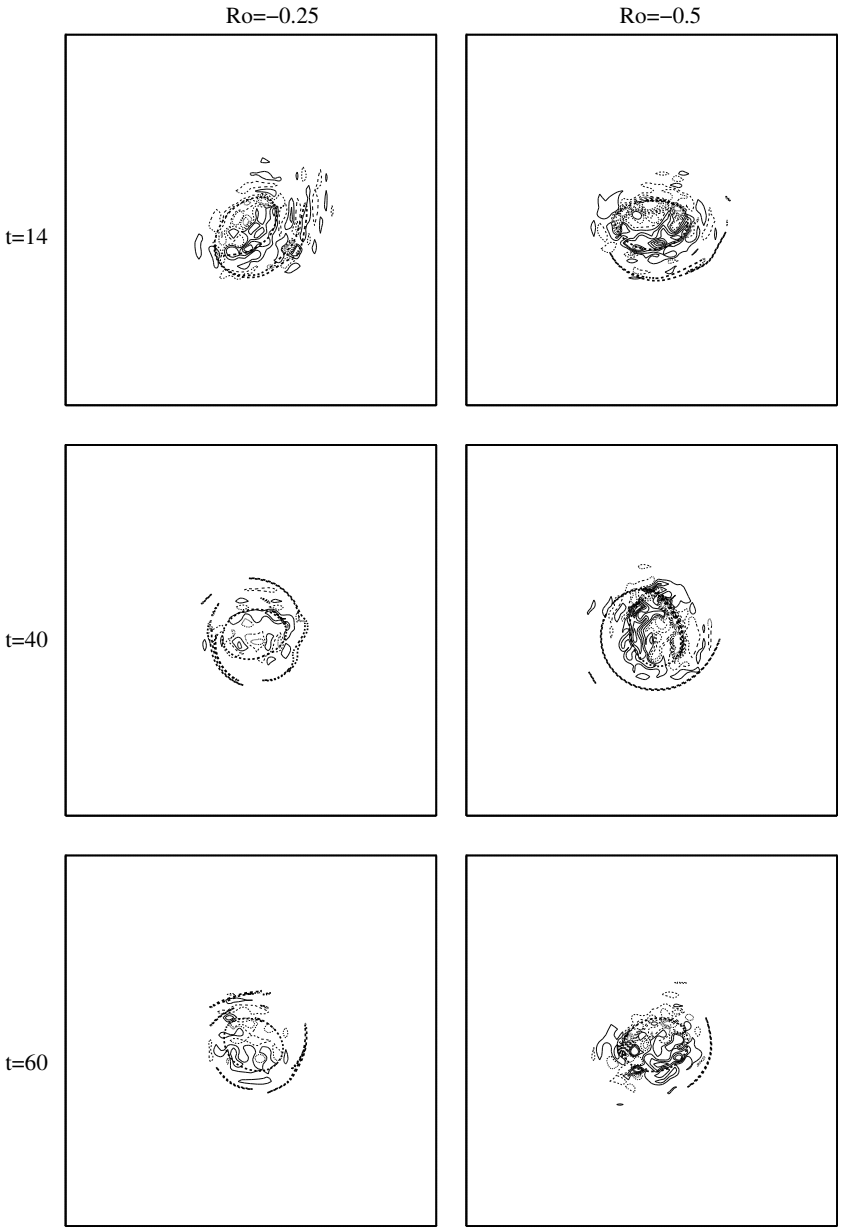

Figure 4.19: Horizontal slices showing contours of w_{imb} for cases $h/r = 0.8$, $\rho_V = 1.0$, $\delta z = 0.2$ at Rossby numbers $Ro = -0.25$ and $Ro = -0.5$ at times $t_{QG} = 14, 40$ & 60. Contour intervals are $\Delta = 5 \times 10^{-6}$ at $Ro = -0.25$ and $\Delta = 2 \times 10^{-5}$ at $Ro = -0.5$. Slices are in the $x - y$ plane at constant $z = 0$ and span the full horizontal domain, i.e. $\pm\pi$ from the domain centre. Solid lines show positive values and broken lines show negative values. Dashed bold contours show the PV contours for this layer.

the evolution.

The contour plots of w_{imb} above have only considered a horizontal slice of the domain. In figure 4.20 we present contours of w_{imb} in the $x-z$ plane for constant $y = 0$ for the cases $h/r = 0.8$, $\rho_V = 0.6$, $\delta z = 0.2$ and $Ro = 0.25, 0.5$ which maybe compared with the view of the full flow in figure 4.16 and the contours of w_{imb} in the $x-y$ plane in figure 4.17. Again we see a larger amount of imbalance for the higher Rossby number case. We see that the angle of the contours is around 30° to 45° from the vertical here. *Viúdez & Dritschel* (2006)[46] showed that IGW's are consistent with the theory of plane waves which in the $x-z$ plane are complex solutions of the form

$$\tilde{g} = \tilde{g}_0 e^{i(kx+mz-\omega_p t)}, \tag{4.3}$$

where k and m are horizontal and vertical wavenumbers. This satisfies the relations

$$\tilde{u} = i\omega_p m k^{-1}\tilde{\mathcal{D}}, \quad \tilde{v} = fmk^{-1}\tilde{\mathcal{D}}, \quad \tilde{w} = -i\omega_p\tilde{\mathcal{D}}, \tag{4.4}$$

where $\tilde{\mathcal{D}}$ is the vertical isopycnal displacement. The frequency ω_p satisfies

$$\omega_p^2 = \frac{f^2m^2 + N^2k^2}{k^2 + m^2}. \tag{4.5}$$

This predicts that $|\tilde{u}_0|/|\tilde{w}_0| = m/k$. When $m/k \simeq N/f = 10$, the angle of the IGW's will be 45°. The ratios seen for the example in figure 4.20 justify the range of angles seen in the waves.

We now turn our attention to one single configuration of vortices being $h/r = 1.2$, $\rho_V = 1.0$, $\delta z = 0.2$ and $Ro = 0.5$.. Firstly, to ensure that inertia-gravity waves are not being generated spuriously as a consequence of a low resolution

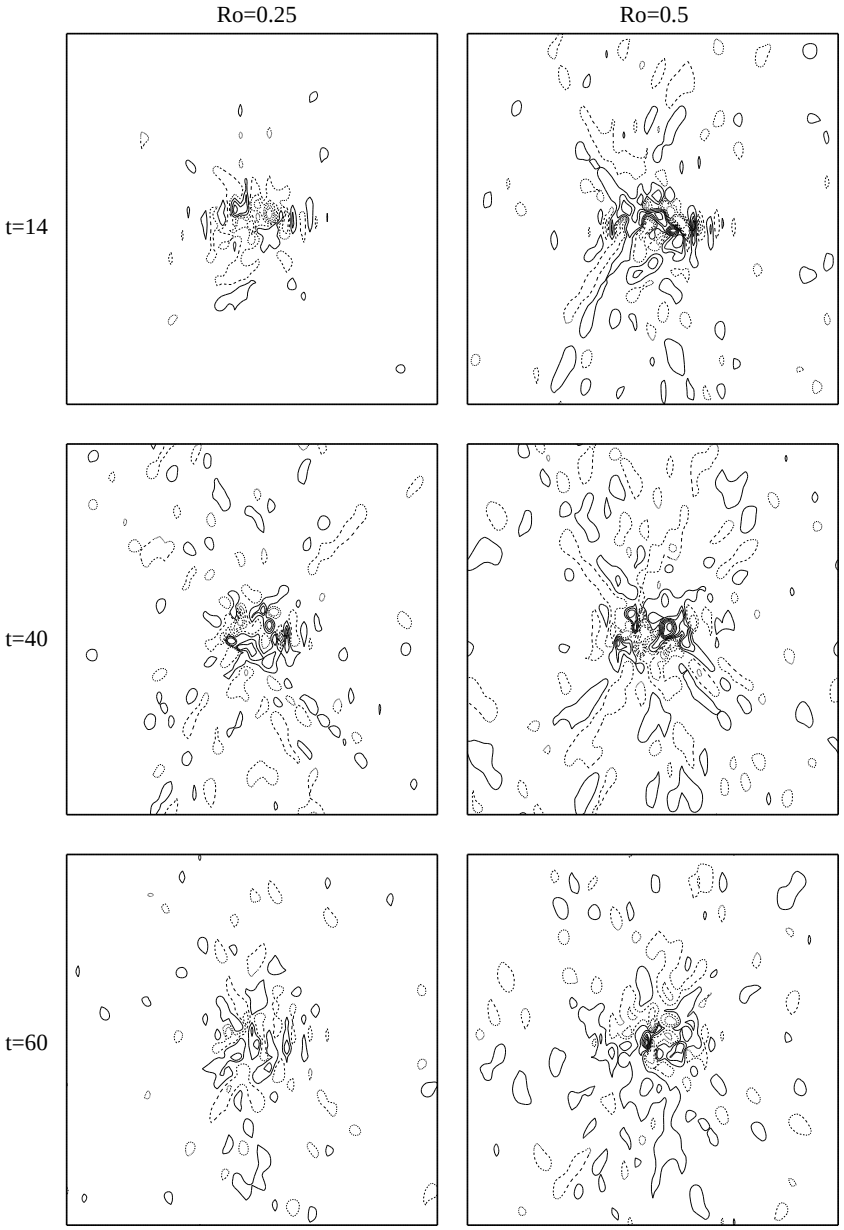

Figure 4.20: Vertical slices showing contours of w_{imb} for cases $h/r = 0.8$, $\rho_V = 0.6$, $\delta z = 0.2$ at Rossby numbers $Ro = 0.25$ and $Ro = 0.5$ at times $t_{QG} = 14, 40$ & 60. Contour intervals are $\Delta = 2 \times 10^{-6}$ at $Ro = 0.25$ and $\Delta = 5 \times 10^{-6}$ at $Ro = 0.5$. Slices are in the $x - z$ plane at constant $y = 0$ and span the full vertical domain, i.e. $\pm\pi$ from the domain centre. Solid lines show positive values and broken lines show negative values.

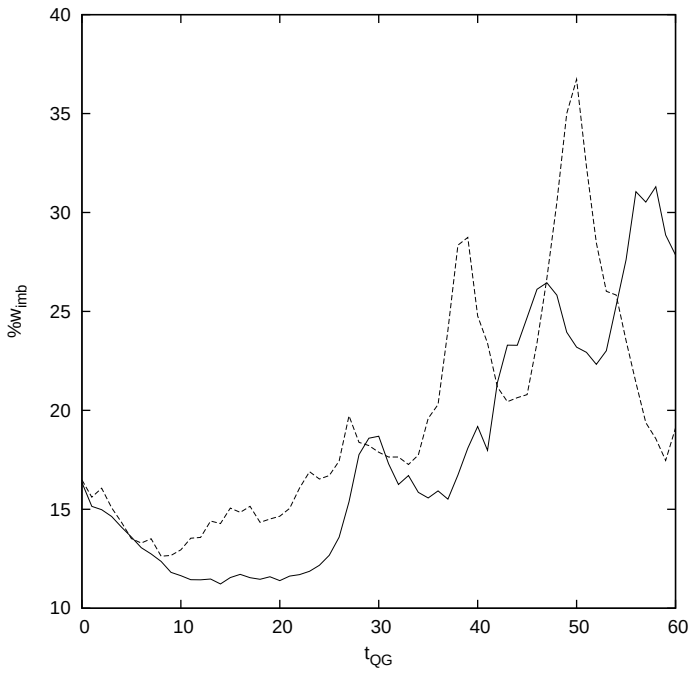

Figure 4.21: Comparison of the r.m.s. percentage of imbalanced vertical velocity against QG time for the case $h/r = 1.2$, $\rho_V = 1.0$, $\delta z = 0.2$ and $Ro = 0.5$ for grid resolutions of 128^3 (solid line) and 64^3 (broken line).

we perform a test calculation using a 128^3 grid (i.e. doubling the number of grid points in each direction).

Figure 4.21 shows the r.m.s. $\%w_{imb}$ for both the standard resolution and the high resolution cases. We see that whilst the local maxima and minima, corresponding to the generation and propagation of IGW's, are not synchronised and tend to be slightly larger for the standard resolution, the order of magnitude of imbalance is similar thus we conclude that the imbalance we see at lower resolutions here is not being generated spuriously during the simulation.

In figure 4.22 we compare contours of imbalanced vertical velocity obtained from NQG at a horizontal slice through the centre of the domain, $z = 0$, for grid resolutions of 64^3 and 128^3 at time $t_{QG} = 29$. These slices are noticeably different in that very definite wave-like motions are apparent in the 128^3 case i.e. in the

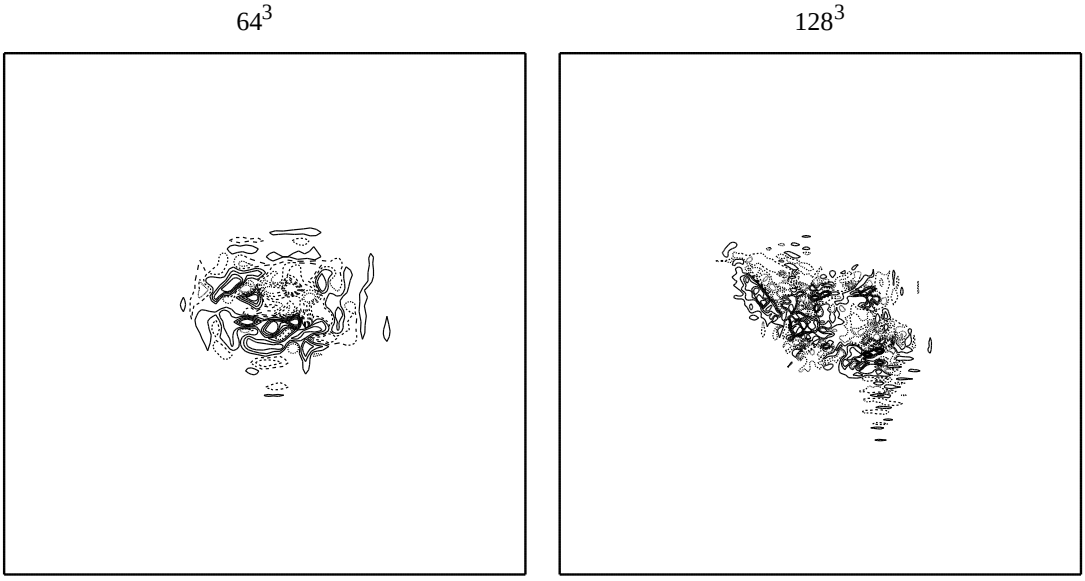

Figure 4.22: Contours of imbalanced vertical velocity obtained using NQG in the $x - y$ plane at $z = 0$ for grid resolutions of 64^3 and 128^3. Initial conditions are $h/r = 1.2$, $\rho_V = 1.0$, $\delta z = 0.2$ and $Ro = 0.5$. Contour interval is $\Delta = 10^{-5}$, solid contours show positive values and broken contours show negative values. Figures generated at QG time $t_{QG} = 29$.

bottom right of the figure. It should be noted by referring back to figure 4.21 that these figures were generated at a local maximum in the r.m.s. $\%w_{imb}$ for the 128^3 which does not correspond with a maximum for the 64^3 case.

In figure 4.23 we show a comparison of using NQG and OPV to obtain the imbalanced vertical velocity at two different times $t_{QG} = 29$ and $t_{QG} = 57$. As can be seen from the figure, a lot less of the field is attributed to imbalance using OPV than NQG. We do however see that OPV still resolves the apparent wave structures seen bottom right at $t_{QG} = 29$ and centre left at $t_{QG} = 57$. It seems then that for a qualitative view of the imbalanced field, NQG is a sufficiently accurate tool.

4.3 Conclusions

In this chapter we have investigated the interactions of two co-rotating non-hydrostatic vortices of uniform and equal potential vorticity over a parameter space of the vortices' height-to-width aspect-ratio, taken to be equal for both vortices, the volume-ratio of the vortices, their vertical offset and the Rossby number. The vortices are initially situated at the margin of stability as described in section 3.1.2.

Over the parameter space investigated we found that the type of interaction occurring during the vortex evolution is dependent on both the volume-ratio and the vertical offset. This is in contrast to the interaction regimes occurring between two co-rotating QG vortices which appeared only to depend on the volume ratio – see section 3.2.1. In this parameter space, non-hydrostatic co-rotating vortices mostly underwent partial-merger at small vertical offsets with partial straining-out mostly only occurring when the vortices were of disparate sizes. At larger vertical offsets the interaction types were generally seen to be PSO with PM generally only occurring for equal volume vortices. Partial mergers

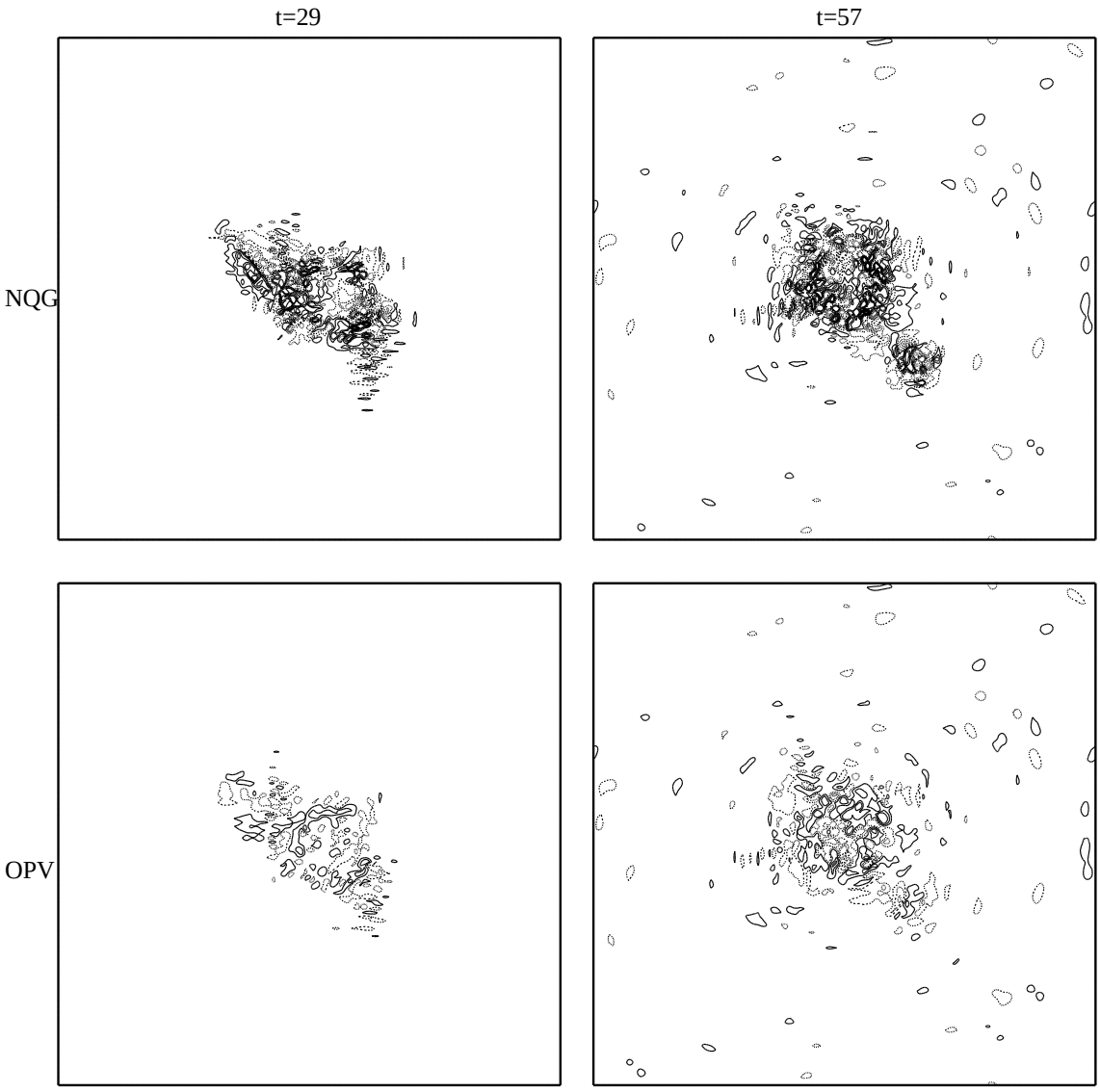

Figure 4.23: Comparison of imbalanced vertical velocity obtained from NQG and OPV at QG times $t = 29$ and $t = 57$ for the case $h/r = 1.2$, $\rho_V = 1.0$, $\delta z = 0.2$, $Ro = 0.5$ with grid resolution 128^3. Contour intervals are $\Delta = 10^{-5}$ at $t = 29$ and $\Delta = 5 \times 10^{-6}$ at $t = 57$. All figures are shown in the $x - y$ plane taken at $z = 0$. Solid contours show positive values and broken contours show negative values.

are frequently seen in this parameter space, not as the merger then re-separation of the two initial vortex but as the destruction of the smaller vortex by the larger vortex. This type of interaction is still classed as PM under the test adapted from *Dritschel & Waugh* (1992)[17] due to the large volume of small vortices and filaments generated during the destruction of the smaller vortex. No significant dependence of the interaction regime on the Rossby number was seen.

The size of the largest vortex averaged over all non-hydrostatic cases for each Rossby number did not exhibit the same growth as seen for QG interactions. This does not necessarily mean that the non-hydrostatic cases generate more debris, more that the amount of PV gained by the largest vortex from the smaller vortex is less, particularly since a higher percentage of cases in this parameter space result in PSO.

By studying the evolution of the average r.m.s. imbalanced part of the vertical velocity over time we see that the amount of imbalance increases over the first 15 QG time units. This period is interestingly similar to the period that the vortices undergo the first phase of their interaction as described in section 3.3. After this period the amount of imbalance remains roughly steady with variations of around $\pm 2.5\%$. We also see that around 10% more imbalanced vertical velocity is generated at $Ro = -0.5$ than any other Rossby number used in this study and also that more imbalanced vertical velocity is seen for $Ro = -0.25$ than for $Ro = 0.25$. Furthermore, it is shown that more imbalance is generated for high absolute values of Ro.

We consider horizontal slices of the domain and view contours of the imbalanced part of the vertical velocity w_{imb}. In cases of PSO, structures resembling wave-trains are seen to be generated by both vortices during the interaction. These wave-trains are generated in a radial direction to the vortex, and in the case of the smaller, orbiting vortex in a PSO regime, are most prominent in the direction of orbit. In PM regimes, where the smaller vortex is destroyed by the

larger vortex to generate a large volume of debris, strong IGW generation is seen in the region that the smaller vortex is being destroyed in.

Comparing identical initial conditions simulated at two different velocity grid resolutions produces qualitative differences in the imbalanced field. However, no order of difference was found in the r.m.s. imbalanced vertical velocity when comparing these simulations. This serves to satisfy us that the imbalance seen is not an unphysical consequence of too low a resolution.

OPV diagnosis was performed at two separate times on one simulation for comparison with NQG. It was seen that whilst OPV provided better separation of the balanced and imbalanced part of the flows, no great qualitative difference was apparent. Since OPV is computationally much more expensive than NQG, the latter is considered as being sufficiently accurate for the current study.

Chapter 5

Conclusions

5.1 Conclusions

In this thesis we have investigated the interactions between two co-rotating vortices of varying volume-ratios, height-to-width aspect-ratios and vertical offsets residing separated in the horizontal so that they reside at the margin of stability under the QG approximation. This margin of stability was determined using a method based on the Ellipsoidal Model (see §3.1.1 and *Dritschel, Reinaud & McKiver* (2004)[13]).

Firstly in chapter 3 we studied the time evolution of these vortices over a four-dimensional parameter space consisting of 625 cases under the quasi-geostrophic model. We identified three different types of strong interaction occurring between the vortices, these being partial straining-out (PSO), partial merger (PM) and complete merger (CM) as defined in *Dritschel & Waugh* (1992)[17]. We found that when vortices are more unequal in size, that is they have a low volume-ratio $\rho_V = 0.2$, the predominant interaction was where the smaller vortex loses some of its volume but the larger vortex did not increase in volume. We conjectured that this occurred due to the smaller vortex being incapable of deforming sufficiently

to get close enough to the larger vortex to allow merger to occur. For cases where $0.4 \leq \rho_V \leq 1.0$, the main interaction regime emerging was partial-merger where some of the volume of the smaller vortex was transfered to the large one. We found that the classical view of vortex merger, that is complete merger, was extremely rare over this parameter space. When complete merger did occur it did so mainly when the vortices were of equal volume and equal height-to-width aspect-ratio. Interestingly we did not find any particular dependence of the interaction type on the vertical offset of the vortices.

Over the parameter space considered in this study, vortex interactions generally underwent two stages in the evolution. The first interaction tended to be merger, this happened extremely quickly usually in less than one characteristic vortex rotation. After around 5 characteristic rotations ($t = 15$) the pair would either separate in PM cases or remain merged in CM cases but would regardless begin ejecting a large quantity of small scale structures. Despite the large number of small scale structures produced, energy was seen to exhibit an 'inverse-cascade' that is the transfer of self-energy to larger physical scales over time.

We find that vortices in an intermediate range of scales, here between $r \approx 0.25$ and $r \approx 0.40$ were unlikely to survive the interaction. By considering the trend in strain from a simple point-vortex model and the absence of significant growth of the larger vortex at the times when this gap became apparent, we concluded that vortices in this range were sheared out into filaments by the larger vortices. We were then left with two distinct vortex populations – those with $r < 0.25$ and those with $0.4 < r < 1.0$. Almost no vortices were found between these two populations.

The largest vortex in an interaction tended to grow by a greater amount the closer the volume-ratio of the initial vortex pair was to unity. At unity ρ_V however there was a high degree of variance in the growth with the radius growing any where between 4.8% and 17.7%. It should be noted that this variance was

not dependent on the vertical offset. In a turbulent flow containing an increasing number of vortices of decreasing scale (see *Reinaud, Dritschel & Koudella* (2003)[39]) statistically interactions between similar sized vortices are rare compared to the interactions between disparate sized vortices, the latter of these leading to only small growth of the largest vortex.

In chapter 4 we consider the interactions arising from a subset of the parameter space used in chapter 3 using non-hydrostatic dynamics. We considered vortices of three separate equal height-to-width aspect-ratios, three volume-ratios and two vertical offsets for different Rossby numbers. The Rossby numbers were chosen such that we had two cyclonic and two anti-cyclonic, i.e. $Ro = \pm 0.25$ and $Ro = \pm 0.5$.

As previously for QG, we investigated the types of interactions arising from the vortex evolutions. We found no cases of CM at all over this parameter space. Furthermore, we witnessed a dependence of the interaction regime on the vertical offset as well as the volume-ratio. Dependence on vertical offset was seen as being negligible in the QG cases. For larger vertical offsets the interaction regimes were seen to be more frequently PSO, with PM only occurring when the vortices were of equal volume. At lower vertical offsets PM was the more predominant interaction regime and PSO occurred mainly when the difference in the volumes between the vortices was very high, i.e. a low volume-ratio. No significant dependence of the interaction regime on the Rossby number was witnessed.

Many of the partial mergers seen in this parameter space showed CSO type behaviour. The smaller vortex in these cases was destroyed by the larger vortex. However, since this vortex was torn into filaments and smaller vortices, the interaction was classed quantitatively as PM due to the size of the structures remaining from the destroyed vortex.

The evolution of the average percentage of the vertical part of the imbal-

anced velocity field, $\%w_{imb}$, was seen to grow over the first 15 QG time units. As has been seen previously this corresponded to the initial interaction phase of the vortices. After $t_{QG} = 15$ the amount of $\%w_{imb}$ was seen to plateau. Negative Rossby numbers, showing an anti-cyclonic situation, were seen to generate more imbalance than their positive, cyclonic counterparts. It was also seen that more imbalance was generated at higher Rossby numbers than for lower Rossby numbers of the same sign.

Structures in the imbalanced part of the flow resembling wave-trains were seen to be generated during the interactions. In PSO interactions these wave-trains were seen to be aligned in the horizontal with the radial axis of the vortex and for the smaller vortex were particularly prevalent in the direction of the vortex orbit.

We compared NQG, the method we used to separated the balanced flow from the full flow, to another method, OPV. We concluded that while OPV is a more accurate method of separating the flow fields, its computational cost is such that using it for the study conducted in chapter 4 is infeasible.

5.2 Future Developments

This work has covered in detail a very wide parameter space. This parameter space has been chosen to represent a good cross-section of the types of structures commonly seen in decaying turbulent flows (see *Reinaud et al.* (2003)[39]). While this is the case, we have naturally had to limit our parameter space to reasonable bounds. Work is currently in progress concerning both the interactions between un-equal strength co-rotating QG vortices, *Özugurlu, Reinaud & Dritschel* (2007)[34], and the interactions between counter-rotating QG vortices, *Reinaud & Dritschel* (2007)[38]. Expansions on these topics would also include investigations in the NH model.

Further developments would also include the comparison of the results obtained for QG vortices in chapter 3 with a larger scale flow populated by many vortex structures chosen randomly from the parameter space given here. A simpler development could also include the study of QG vortex interactions in the presence of a background shear flow to represent the influence of distant vortices as done for a single vortex in *McKiver* (2003)[29] and *McKiver & Dritschel* (2003)[30].

The non-hydrostatic cases studied have only covered the interactions between equal height-to-width aspect-ratio vortices at two different Rossby numbers for cyclonic and anti-cyclonic situations. This study is open for expansion into interactions between vortices of different aspect-ratios and also at more extreme Rossby numbers.

Bibliography

[1] Arai, M. & Yamagata, T. Asymmetric evolution of eddies in rotating shallow water. *Chaos* 4(2): 163–175

[2] Aristotle, *trans.* Webster, E. W. Meteorology, Book 3. http://classics.mit.edu/Aristotle/meteorolgy.3.iii.html

[3] Billant, P., Dritschel, D. G. & Chomaz, J.-M. Bending and twisting instabilities of columnar elliptical vortices in a rotating stratified fluid. *J. Fluid Mech.*, 561: 73–102, 2006.

[4] Chandrasekhar, S. *Ellipsoidal Figures of Equilibrium.* Dover, 1969.

[5] Charney, J. Geostrophic turbulence. *J. Atmos. Sci.*, 28: 1087–1095, 1971.

[6] Dritschel, D. G. A general theory for two-dimensional vortex interactions. *J. Fluid Mech.*, 293: 269–303, 1995.

[7] Dritschel, D. G. Vortex merger in rotating stratified flows. *J. Fluid Mech.*, 455: 83–101, 2002.

[8] Dritschel, D. G. & Ambaum, M. H. P. A contour-advective semi-lagrangian algorithm for the simulation of fine-scale conservative fields. *Q. J. Roy. Meteorol. Soc.*, 123: 1097–1130, 1997.

[9] Dritschel, D. G., Macaskill, C. The role of boundary conditions in the simulation of rotating, stratified turbulence. *Geophys. Astrophys. Fluid Dyn.*, 92: 233–253, 2000.

[10] Dritschel, D. G., Polvani, L. M. & Mohebalhojez, A. R. The contour-advective semi-lagrangian algorithm for the shallow-water equations. *Mon. Wea. Rev.*, 127(7): 1151–1165, 1999.

[11] Dritschel, D. G. & Reinaud, J. N. Vortex dynamics in rotating, stably-stratified turbulence. In: Proceeding of the International Symposium on Dynamics and Statistics of Coherent Structures in Turbulence: Roles of Elementary Vortices. *ed. Shigeo Kida*, Tokyo, 21–23 October, 2002.

[12] Dritschel, D. G. & Viúdez, Á The persistence of balance in geophysical flows. *J. Fluid Mech.*, 570: 365-383, 2007.

[13] Dritschel, D. G., Reinaud, J. N. & McKiver, W. J. The quasi-geostrophic ellipsoidal model. *J. Fluid Mech.*, 505: 201–223, 2004.

[14] Dritschel, D. G. & de la Torre Juárez, M. The instability and breakdown of tall columnar vortices in a quasi-geostrophic fluid. *J. Fluid Mech.*, 328: 129–160, 1996.

[15] Dritschel, D. G., de la Torre Juárez, M. & Ambaum, D. H. P. On the three-dimensional vortical nature of atmospheric and oceanic flows. *Phys. Fluids*, 11(6): 1512–1520, 1999.

[16] Dritschel, D. G., & Viúdez, A. A balanced approach to modelling rotating stratified geophysical flows. *J. Fluid Mech.*, 488, 123–150, 2003.

[17] Dritschel, D. G., & Waugh, D. W. Quantification of the inelastic interaction of unequal vortices in two-dimensional vortex dynamics. *Phys. Fluids A*, 4(8): 1737–1744, 1992.

[18] Ebbesmeyer, C. C., Taft, B. A., McWilliams, J. C., Shen, C. Y., Riser, S. C., Rossby, H. T., Biscaye, P. E. & Östlund, H. G. Detection, structure and origin of extreme anomalies in a western Atlantic oceanographic section. *J. Phys. Ocean*, 16: 591–612, 1986.

[19] Frigo, M. & Johnson, S. G. FFTW C subroutine libraries for computing discrete Fourier transforms. *http://www.fftw.org/*

[20] Garret, C., *eds.* Batchelor, G. K., Moffat, H. K. & Worster, M. G. The Dynamic Ocean, chapter 10. *Cambridge University Press*, 2000.

[21] Gill, A. E. Atmosphere-Ocean Dynamics. *Academic Press*, 1982.

[22] von Hardenberg, J., McWilliams, J. C., Provenzale, A., Shchepetkin, A. & Weiss, J. B. Vortex merging in quasi-geostrophic flows. *J. Fluid Mech.*, 412: 331–353, 2000.

[23] Holton, J. R., Haynes, P. H., McIntyre, M. E., Douglass, A. R., Rood, R. B. & Pfister, L. Stratosphere-troposphere exchange. *Revs. Geophys.*, 33(4): 403–439, 1995.

[24] Hoskins, B. J., McIntyre, M. E. & Robertson, A. W. On the use and significance of isentropic potential-vorticity maps. *Q. J. Meteorol. Soc.*, 111: 877–946, 1985.

[25] Edens, H. Weather photography. Image ©Harald Edens, reproduced with permission. *http://www.weather-photography.com/*

[26] Hua, B. L. & Haidvogel, D. B. Numerical simulations of the vertical structure of quasi-geostrophic turbulence. *J. Atmos. Sci.*, 43(23): 2923–2936, 1986.

[27] Marcus, P. S. Numerical simulations of Jupiter's great red spot. *Nature*, 331: 693–696

[28] Melander, M. V., Zabusky, N. J. & McWilliams, J. C. Symmetric vortex merger in two dimensions: causes and conditions. *J. Fluid Mech.*, 195: 303–340, 1988.

[29] McKiver, W. J. The motion of a quasi-geostrophic ellipsoidal vortex in a background shear flow. *Ph.D thesis*, 2003.

[30] McKiver, W. J. & Dritschel, D. G. The motion of a fluid ellipsoid in a general linear background flow. *J. Fluid Mech.*, 474: 147–173, 2003.

[31] McKiver, W. J. & Dritschel, D. G. Balance in non-hydrostatic rotating stratified turbulence *J. Fluid Mech.*, *Submitted*, 2006.

[32] Mohebalhojeh, A. R. & Dritschel, D. G. On the representation of gravity waves in numerical models of the shallow water equations. *Q. J. R. Meteorol. Soc.* 126: 669–689, 2000.

[33] Munk, W., Armi, L., Fischer, K. & Zachariasen, F. Spirals on the sea. *Proc. Roy. Soc. London* A456: 1217–1280, 2000.

[34] Özugurlu, E., Reinaud, J. N. & Dritschel, D. G. Interactions between two quasi-geostrophic vortices of unequal potential vorticity. *Under consideration for J. Fluid Mech.*, 2006.

[35] Polvani, L. M., McWilliams, J. C., Spall, M. A. & Ford, R. The coherent structures of shallow-water turbulence: Deformation-radius effects, cyclone/anticyclone asymmetry and gravity-wave generation. *Chaos* 4(2): 177–186, 1994.

[36] Reinaud, J. N. & Dritschel, D. G. The merger of vertically offset quasi-geostrophic vortices. *J. Fluid Mech.*, 469: 287–315, 2002.

[37] Reinaud, J. N. & Dritschel, D. G. The critical merger distance between two co-rotating quasi-geostrophic vortices. *J. Fluid Mech.*, 522: 357–381, 2005.

[38] Reinaud, J. N. & Dritschel, D. G. Destructive interactions between two counter-rotating quasi-geostrophic vortices. *In preparation – to be submitted to J. Fluid Mech.*, 2007.

[39] Reinaud, J. N., Dritschel, D. G. & Koudella, C. The shape of vortices in quasi-geostrophic turbulence. *J. Fluid Mech.*, 474: 175–192, 2003.

[40] Rudnick, D. On the skewness of vorticity in the upper ocean. *Geophys. Res. Lett.*, 28: 2045–2048, 2001.

[41] Stegner, A. & Dritschel, D. G. A numerical investigation of the stability of isolated vortices beyond the quasi-geostrophic regime. *J. Phys. Ocean.*, 30(10): 2562–2573, 2000.

[42] Theiss, J. Equatorial energy cascade, critical latitude, and the predominance of cyclonic vortices in geostrophic turbulence. *J. Phys. Ocean.*, 34: 1663–1678, 2004.

[43] Tran, C. V., Dritschel, D. G. Vanishing enstrophy dissipation in two-dimensional Navier-Stokes turbulence in the inviscid limit. *J. Fluid Mech.*, 559: 107–116, 2006.

[44] Vallis, G. K. Atmospheric and Oceanic Fluid Dynamics: Fundamentals and Large Scale Circulation *Cambridge Press*, 2006.

[45] Viúdez, Á & Dritschel, D. G., Optimal potential vorticity balance of geophysical flows *J. Fluid Mech.*, 521: 343–352, 2004.

[46] Viúdez, Á & Dritschel, D. G., Spontaneous generation of inertia-gravity wave packets by balanced geophysical flows. *J. Fluid Mech.*, 553: 107–117, 2006.

[47] Waugh, D. W. The efficiency of symmetric vortex merger. *Phys. Fluids A*, 4(8): 1745–1758, 1992.

[48] White, A. A. A view of the equations of meteorological dynamics and various approximations. *Large-scale atmosphere-ocean dynamics I*, eds: Norbury, J & Roulstone, I. *Cambridge Press*, 1–100, 2002.